UNIVERSITY OF CALIFORNIA
Los Angeles

The Synthesis and Application of Chemical Vapor Deposited Graphene.

A dissertation submitted in partial satisfaction of the

Requirements for the degree of Doctor of Philosophy

in Chemistry

by

Jaime Antonio Torres

2014

ABSTRACT OF THE DISSERTATION

The Synthesis and Application of Chemical Vapor Deposited Graphene

by

Jaime Antonio Torres

Doctor of Philosophy in Chemistry

University of California, Los Angeles, 2014

Professor Richard B. Kaner, Chair

Graphene is one of the most amazing materials every discovered. It is the first stable two-dimensional crystal ever studied and has broadly impacted a myriad of fields ranging from physical science to engineering. Science has made such great advancements due to graphene that its discovery earned Nobel recognition in 2010. Initially isolated from bulk graphite using cellophane tape, its use in macroscale applications requires methods to produce it in high quality and on a very large scale. This synthetic problem is the basis for this thesis whereby the scalable synthesis and application of graphene is demonstrated utilizing chemical vapor deposition (CVD).

Mono-carbon containing methane gas is the most utilized carbon precursor for the CVD growth of graphene. To study the effects of other hydrocarbon precursor gases, graphene was grown by chemical vapor deposition from methane, ethane, and propane on copper foils. The larger molecules were found to more readily produce bilayer and multilayer graphene, due to a higher carbon concentration and different decomposition processes. Single- and bilayer graphene was grown with good selectivity in a simple, single-precursor process by varying the pressure of

ethane from 250 to 1000 mTorr as characterized by Raman spectroscopy. The bilayer graphene is AB-stacked as shown by selected area electron diffraction analysis.

Vertically oriented structures of conductors and semiconductors, especially single crystals, are of great technological importance due to their directional and rapid charge carrier transport yet there does not exist a facile way to produce them. Here, we report a facile, solution-based "bottom-up" route for producing highly oriented, single crystalline, vertical arrays of conjugated molecules that exhibit uniform morphological and crystallographic orientations by employing a layer of graphene as a guiding substrate. Using an oligoaniline as model, we demonstrate that this method is highly versatile, allows for precision growth and deposition of crystals by first patterning the growth graphene substrates, and allows for the anisotropic transport of charged carriers to efficiently reach a conductivity of 12.3 S/cm along the vertical axis, the highest reported to date for an aniline oligomer. Large-area devices where current from individual crystals can be collectively harnessed are demonstrated, illustrating its promise for both micro- and macro-scopic device applications.

The transfer of large sheets of graphene is desired for a variety of applications including electronics and membrane technology. Currently, CVD grown graphene is isolated from a growth catalyst by use of polymer-assisted transfer. The underlying growth catalyst is etched away while the polymer acts as a support for transfer to arbitrary substrates before it is removed chemically and by high temperature annealing. While transferring graphene onto rigid substrates that can survive post-processing high temperature anneals is possible, the same is not true for plastic and flexible substrates. The use of the polymer may lead to unwanted contamination and

damaged graphene films. We demonstrate a way to transfer very large sheets of graphene tailored for thickness onto flexible and porous membranes supports for use in size selective filtration. We utilize optimized concentrations of ammonium persulfate to etch graphene grown on Cu-Ni alloys to produce polymer-free graphene film that can be transferred onto arbitrary substrates.

The dissertation of Jaime Antonio Torres is approved.

Xiangfeng Duan

Eric M. Hoek

Richard B. Kaner, Chair

University of California, Los Angeles

2014

This work would not have been possible without the love and support of numerous friends, family, and mentors I've had the pleasure to know. I dedicate it to you who have nurtured this seed of knowledge.

Table of Contents

List of figures

Acknowledgements

This is the moment I have dreaded for the entirety of my dissertation writing because there are too many people to thank personally by first name and I certainly don't want to miss a single one of them. I find the old adage "it takes a village to raise a child" very on point and would like to add that it "takes a village of professors to raise a PhD." I am forever indebted to the communities that have raised me from being a stubborn, introverted, know-it-all punk kid to a stubborn, extroverted, know-it-all chemistry PhD.

First and foremost I'd like to thank my mother, Teresa Torres, who did a masterful job raising 3 kids on her own and through the years, though we've butted heads, I know and appreciate her deep love for her baby son. I'd like to thank my very first research mentor, Professor Vince Lavallo who saw some spark in me towards the sciences and was kind enough to show me the ropes and introduce me to research at UCR. I'd also like to thank Professor Chris Reed and his group at UCR for taking me into his lab and exposing me to the wonders of the scientific method. I'd like to say thank you to UC LEADS who fanned the flames of interest and made it possible for me to connect with Professor John Arnold at UC Berkeley who taught me valuable lessons on synthesis and good Thai food. I'd like to give gratitude to Professors Frank Gomez and Wayne Tikkanen at CSULA for allowing me to grab my bearings in life and pursue a PhD. I'm indebted to Professors Luis Campos at Columbia and Craig Hawker at UCSB for taking my research and people skills to another level. I am especially grateful to Drs. Fred Harris, David Van Heerdan, and Ellen Heian from BSST/ZT Plus who taught me how to succeed beyond academia and for all the laughs. Everyone in the Kaner group, I am grateful for knowing you and allowing every one of you to expand the size of my current family. Much thanks to Ms. Nanetta Pon, Ms. Rebecca Li, and Mr. Winn Ho. All of you reawakened in me a sense of exploration I

had long feared forgotten. A very special thank you to Ms. Yesenia Garcia who is my rock throughout every up and down I had at UCLA. Her love and support is the very nourishment for my heart and soul. Much love to you.

I cannot forget the wonderful mentors and peers at the Intelligent Polymer Research Institute in the University of Wollongong, NSW, Australia. I am grateful for the hospitality and assistance of Dr. Rouhollah Ali Jalili, Dr. Adrian Gestos and Prof. Gordon Wallace who provided encouragement and a go get it attitude. Thank you to Nicolas Martino, a true friend and like-minded soul if I ever met one.

Last but not least, I'd like to thank my graduate mentor Professor Ric Kaner for his support and guidance. Looking back at the last four years of my life, there is no other advisor I can imagine working for other than you. You provided the atmosphere to explore my interests and my abilities to the fullest and I am a much better person today because of it.

Vita

2006	B.S., Chemistry, UC Riverside, California
2005- 2006	University of California Leadership Excellence through Advanced Degrees (UC LEADS) Scholar
2008	M.S., Chemistry, CSULA, California
2008	Research Intern in Science and Engineering (RISE) UC Santa Barbara's Material's Research Laboratory
2009	Research Scientist, BSST/ ZT Plus, Asuza, California
2010	Intern, Aerospace Research Labs
2010	Clean Green for Industry National Science Foundation Scholar
2013	Visiting Scholar, Intelligent Polymer Research Institute, University of Wollongong, Wollongong, NSW, Australia
2014	Intern Office of Intellectual Property UCLA
2010- present	Senior Research Associate, Department of Chemistry and Biochemistry, UCLA, California

Publications

Torres, J.A., Kaner R.B, "Graphene Synthesis: Graphene Closer to Fruition" *Nature Materials* **13**, 328–329 (2014)

Wang, Y., Torres, J.A. et al., “Graphene-assisted solution growth of vertically-oriented organic semiconducting single crystals”. (2014)

Wassei, Jonathan K., Torres, J.A., et al. "Chemical vapor deposition of graphene on copper from methane, ethane and propane: Evidence for bilayer selectivity." *Small* **8**.9 (2012): 1415-1422.

Gaspar, A., Baghdachi, S., Goldberg, M., Stevens, S., Torres, J.A., Salgado, M., & Gomez, F. A. (2008). Fritless Chromatographic Microfluidic-Based Columns for Chemical Separations. *American laboratory*, **40** (18), 13-16.

Chapter 1: Electronic, Thermal, Optical, and Mechanical Properties of Graphene

Graphene has attracted a great deal of intrigue since its first demonstrated isolation in 2004[1]. It is a two-dimensional crystal of carbon bonded together in a repeating pattern of hexagons. Graphene can be considered a single sheet of graphite and is the building block for a variety of other carbon materials of differing dimensionalities (Figure 1.1).

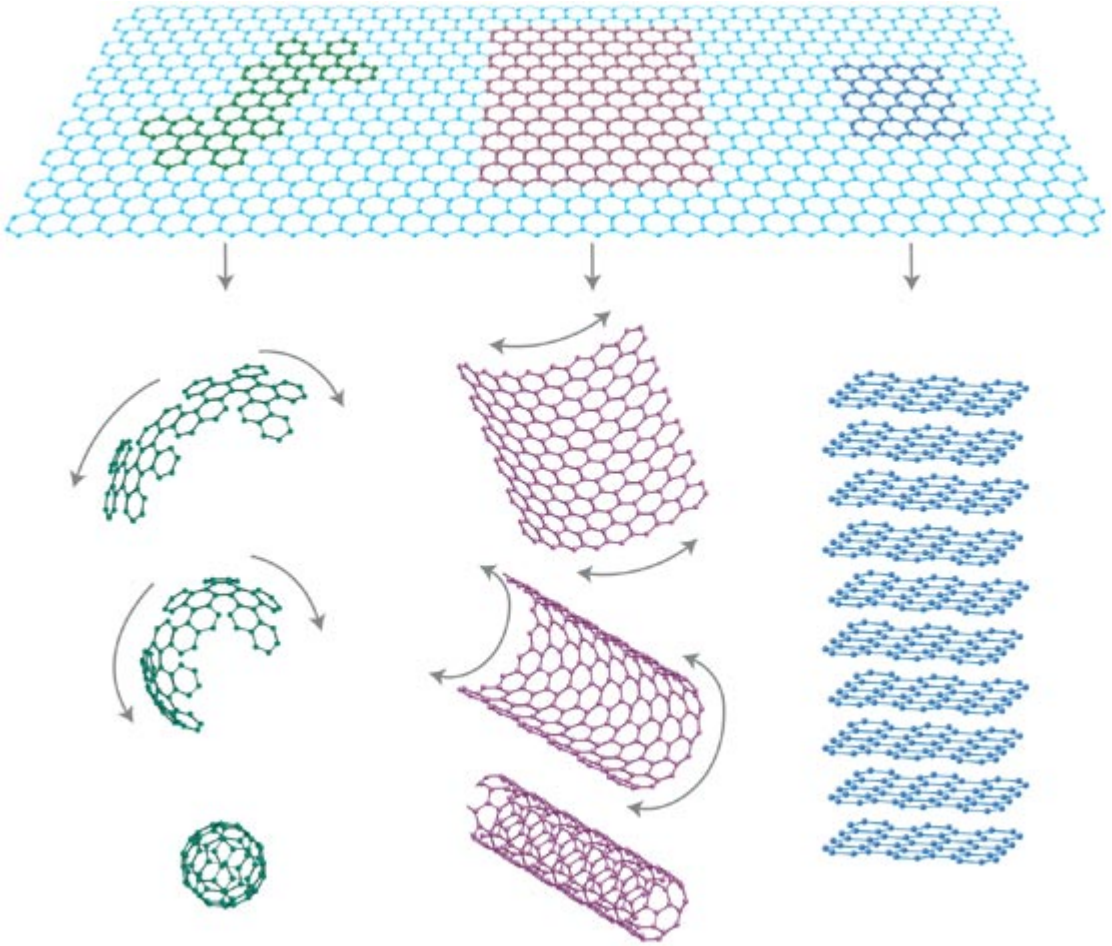

Figure 1.1 | Graphene as a 2D building material for carbon materials of all other dimensionalities. Graphene can be wrapped up into 0D buckyballs, rolled into 1D nanotubes, or stacked into 3D graphite. (reprinted with permission[9] © American Association for the Advancement of Science (AAAS))

Recognized as an integral part of 3D materials, graphene was nonetheless presumed not to exist in the free state[2]. Most believed this 2D version of carbon to be unstable with respect to the formation of curved structures such as soot, fullerenes and nanotubes. When freestanding graphene was unexpectedly exfoliated and the follow-up experiments confirmed that its charge carriers were indeed massless Dirac fermions by Giem and Novoselov[7] two things occurred: 1) the world of 2D crystals became widely accessible and 2) new flexible nanoelectronic devices moved closure to fruition.

Graphene's unusual electronic properties:

Let's begin at the beginning: Each carbon atom in graphene's hexagonal lattice has four valence electrons; the first three are used to form covalent sp^2 bonds, while the fourth resides in a p_z orbital that forms π bonds distributed equally along 3 directions thus leading to a bond order of 1 and 1/3. Graphene contains numerous covalent, delocalized π-bonds suitable for the rapid movement of injected electrons leading to high electronic conductivity. Extraordinary room temperature carrier mobility of >20,000 cm^2/Vsec has been demonstrated with graphene devices[10]. In addition, graphene displays an ability to absorb photons uniformly across a wide spectrum ranging from infrared to ultraviolet light. Although a single layer thick, graphene absorbs 2.3% of light[21] and has an exceptionally high surface-to-volume ratio as would be expected for a two-dimensional material. Graphene has no net dipole and displays hydrophobicity as a consequence of its non-polar bonding. The tight, chemical bonding between carbon atoms also makes graphene one of the strongest materials known[29]. Columbia University mechanical engineering professor James Hone once said it is "so strong it would take an elephant, balanced on a pencil, to break through a sheet of graphene the thickness of Saran

Wrap." Indeed graphene is recognized as one of the strongest materials known, capable of withstanding a great deal of stretching and fracturing.

Electronic carriers move ballistically in graphene:

Electrons move through graphene incredibly fast and begin to exhibit behaviors as if they were massless[3], mimicking the physics that governs particles at super small scales. In condensed matter physics, the Schrödinger equation suffices to describe the electronic properties of materials. When dealing with graphene — its charge carriers mimic relativistic particles and are more easily and naturally described starting with the Dirac equation rather than the Schrödinger equation. The electrons moving around graphene's carbon atoms interact with the periodic potential of the honeycomb lattice to give rise to new quasiparticles that at low energies (E) are accurately described by the (2+1)-dimensional Dirac equation with an effective speed of light $v_F \approx 106\ m^{-1}s^{-1}$. These quasiparticles, called massless Dirac fermions[8], can be seen as electrons that have lost their rest mass (m_0) or as neutrinos that acquired the electron charge e. The relativistic like description of electron waves on honeycomb lattices provides a new way to probe quantum electrodynamics (QED)[9] phenomena by measuring graphene's electronic properties.

Interestingly, graphene demonstrates an ambipolar electric field effect (Figure 1.2) such that charge carriers can be tuned continuously between electrons and holes in concentrations (n) as high as $10^{13}\ cm^{-2}$ and their mobilities (μ) can exceed 15,000 $cm^2V^{-1}s^{-1}$ even under ambient conditions.

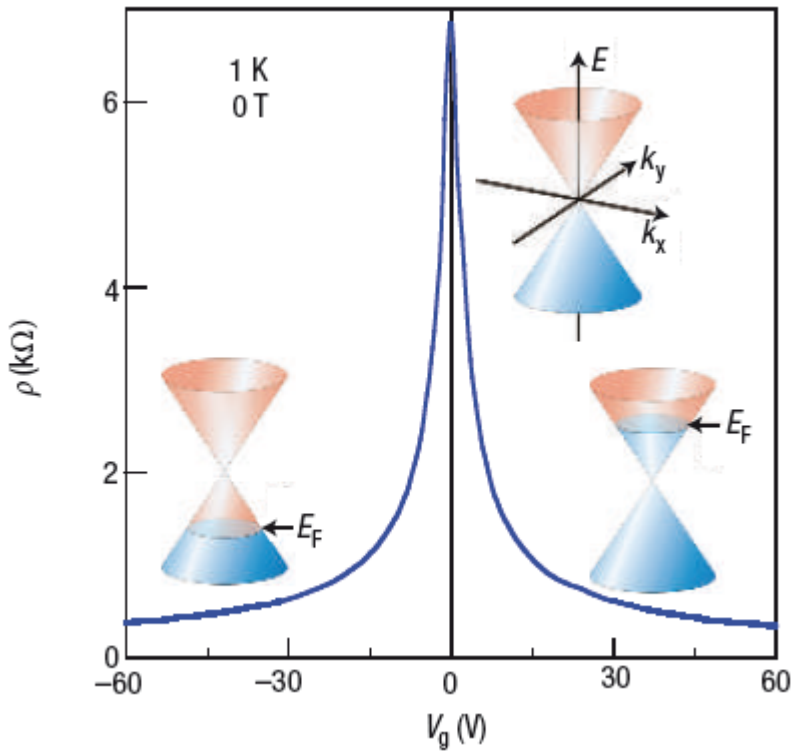

Figure 1.2 | Ambipolar electric field effect in single-layer graphene. The inset shows graphene's conical low-energy spectrum E(k), indicating changes in the position of the Fermi energy (E_f) with changing gate voltage (V_g). Positive (or negative) V_g induce electrons (or holes) in concentrations $n = K_{Vg}$, where the coefficient $K = 7.2 \times 10^{10} cm^{-2}V^{-1}$ for field-effect devices with a 300 nm SiO_2 layer used as a dielectric (reprinted with permission[9] © American Association for the Advancement of Science (AAAS)).

Graphene is a zero-gap semiconductor, in which low-E quasiparticles within each valley can formally be described by the Dirac-like Hamiltonian:

$$\hat{H} = \hbar v_F \begin{pmatrix} 0 & k_x - ik_y \\ k_x + ik_y & 0 \end{pmatrix} = \hbar v_F \boldsymbol{\sigma} \cdot \mathbf{k} \qquad [1.1]$$

where **k** is the quasiparticle momentum, **σ** the 2D Pauli matrix and the k-independent Fermi velocity v_F plays the role of the speed of light. Graphene's honeycomb lattice is made up of two equivalent carbon sublattices A and B (Figure 1.3a).

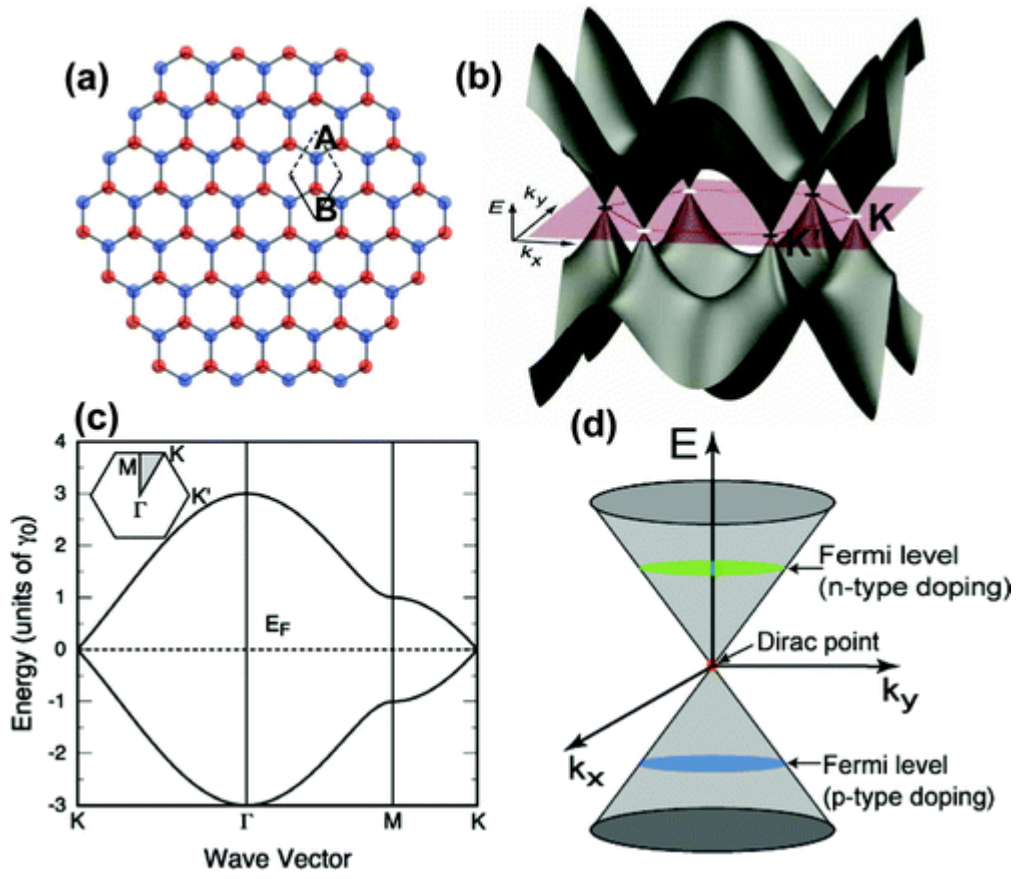

Figure 1.3 | **a.** The unit cell and **b.** The 3D bandstructure of graphene. **c.** Dispersion of the states of graphene. **d.** Approximation of the low energy bandstructure as two cones touching at the Dirac point. The position of the Fermi level determines the nature of the doping and the transport carrier. (reprinted with permission[11] © American Chemical Society).

The cosine-like energy bands associated with the sublattices intersect at zero E near the edges of the Brillouin zone (Figure 1.3b), giving rise to conical sections of the energy spectrum for $|E| < 1$ eV (Figure. 1.3d). Note that there are two π electrons per unit cell and these electrons fully occupy the lower π band. A detailed calculation of the density of states will reveal that the density of states at the Fermi energy is zero, therefore making graphene a zero-gap semiconductor. The existence of a zero gap at the K points comes from the symmetry requirement that the two carbon atoms A and B in the hexagonal lattice are equivalent to each other.

Electrons moving through graphene travel with little scattering and reported low-temperature mobility approaching 200,000 $cm^2V^{-1}s^{-1}$ for carrier densities below 5 times 10^9 cm^{-2} demonstrate the ballistic transport of carriers through graphene[10]. Such values cannot be attained in semiconductors and are attributed to the unique properties of graphene.

Thermal Properties of Graphene:

Graphene's strong covalent bonds are responsible for the quick dissipation of lattice vibrations known as phonons, which leads to extremely high thermal conductivities (κ) >3,000 WmK^{-1} at room temperature[16] (Figure 1.4c).

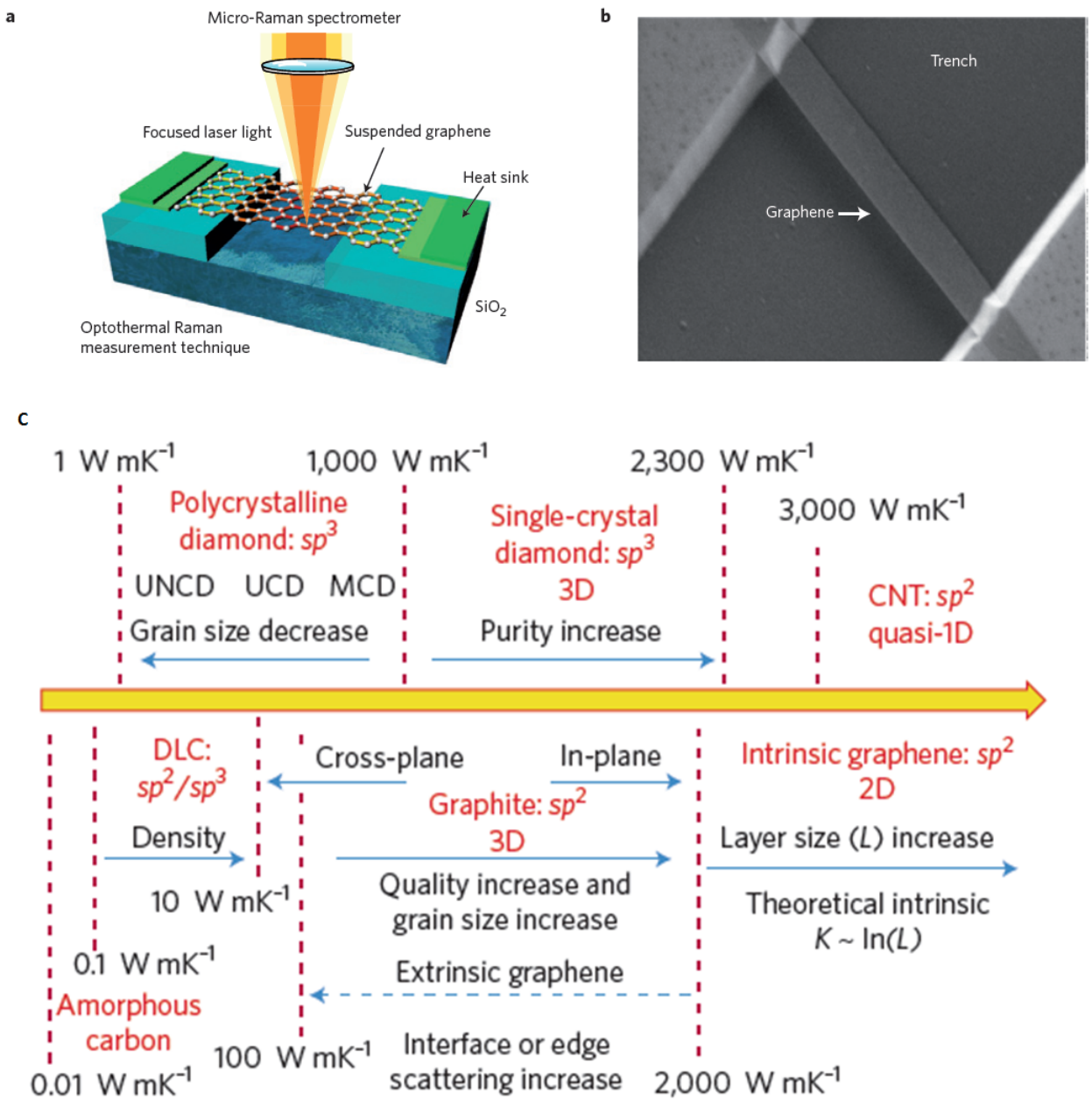

Figure 1.4 | The thermal conductivity of graphene and various carbon materials: a. Experimental study of heat conduction in graphene was made possible by an optothermal Raman technique. The heating power ΔP was provided by a laser light focused on a suspended graphene layer connected to heat sinks at its ends. **b.** Graphene of rectangular shape suspended across a 3 μm-wide trench in a Si wafer **c.** Comparison of the thermal conductivities of various carbon materials. The figure is based on average values reported in the literature. The axis is not to scale. (reprinted with permission[16] © Nature Publishing Group).

In solid materials, heat is carried by acoustic phonons and thermal conductivity is introduced through Fourier's law, $q = -K\Delta T$, where q is the heat flux, K is the thermal conductivity and ΔT is the temperature gradient. In this expression, K is treated as a constant, which is valid for small temperature (T) variations. Over a wide temperature range, K is a function of T. The value K is actually treated as $K = K_p + K_e$, where K_p and K_e are the phonon and electron contributions, respectively. In nanostructures, K is reduced by scattering from boundaries and therefore can be utilized to manipulate phonon dispersions to alter the final thermal conductivity.

Thermal transport in graphene can be dominated by the intrinsic properties of the strong sp^2 lattice, rather than by phonon scattering on boundaries or by disorder, giving rise to extremely high K values. This is certainly true in mechanically exfoliated graphene,[17] but CVD grown graphene films on metal foils tend to be polycrystalline in nature.

Does the presence of numerous grain boundaries affect the thermal conductivity significantly? Laser heating experiments[19] conducted on suspended CVD monolayer graphene were performed by monitoring the Raman G peak, room-temperature thermal conductivity and interface conductance of $(370 + 650/-320)$ $Wm^{-1}K^{-1}$ and $(28 + 16/-9.2)$ $MWm^{-2}K^{-1}$ were reported for the supported graphene. The thermal conductivity of the suspended graphene exceeds $(2500 + 1100/-1050)$ $Wm^{-2}K^{-1}$ near 350 K and becomes $(1400 + 500/-480)$ $Wm^{-2}K^{-1}$ at about 500 K. These values for the supported area of the CVD graphene are comparable to the recently reported values for mechanically exfoliated graphene on SiO_2. The thermal conductivity of the suspended region of the CVD graphene is higher than the reported values for graphite at near room temperature and 500 K, respectively. Thus, the presence of polycrystalline grain boundaries does not sufficiently alter the thermal properties of the graphene and the quasi-ballistic transport of

low frequency phonons with mean-free paths longer than the laser beam has been demonstrated. The ability to dissipate heat efficiently, while conducting electrons ballistically, may benefit the areas of optoelectronics, thermal management, thermoelectrics and solar energy harvesting from the application of graphene.

Optical Properties:

Each single layer of graphene absorbs 2.3% of the visible light that interacts with it. A single layer is thus transparent without causing glare. The optical image contrast can be used to identify graphene on top of a Si/SiO_2 substrate (Figure 1.5). The transmittance of single layer graphene (SLG) can be derived by applying Fresnel equations in the thin-film limit for a material with a fixed universal optical conductance[20]:

$$T = (1 + 0.5\pi\alpha)^{-2} \approx 1 - \pi\alpha \approx 97.7\% \qquad [1.2]$$

Where $\alpha = e^2/(4\pi\varepsilon_0\hbar c) = G_0/(\pi\varepsilon_0 c)$ and the fine structure constant $G_0 = e^2/(4\hbar) \approx 6.08 \times 10^{-5}\ \Omega^{-1}$,

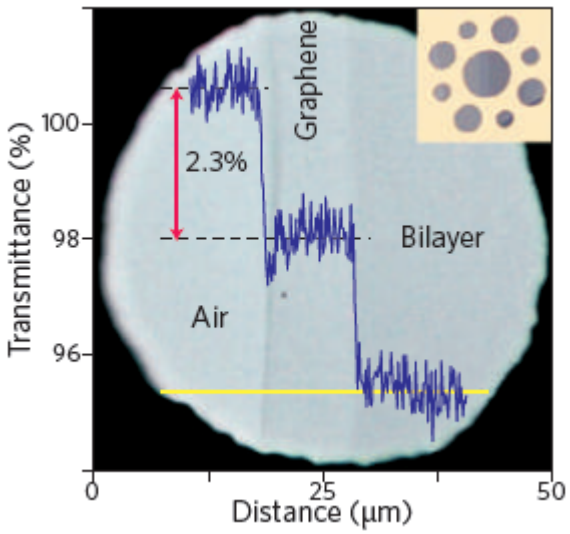

Figure 1.5 | Optical image of single and bilayer graphene transferred onto Si/SiO_2. The contrast scales with the increasing number of layers as a result of interference. (reprinted with permission[42] © American Chemical Society).

Perhaps the most ready application for graphene will be as a flexible transparent conductor. Briefly, optoelectronic devices such as displays, touch screens, light-emitting diodes and solar cells require materials with low sheet resistance, R_s, and high transparency. In a thin film,

$R_s = \rho/t$, where t is the film thickness and $\rho = 1/\sigma$ is the resistivity, σ is direct current conductivity. For a rectangle of length L and width W, the resistance R is:

$$R = \rho/t \times L/W = R_s \times L/W \qquad [1.3]$$

The term L/W can be seen as the number of squares of side W that can be superimposed on the resistor without overlapping. Thus, even if R_s has units of ohms (as R does), it is historically quoted in 'ohms per square' (Ω/□).

Figure 1.6 compares graphene to several other types of transparent conductors. The state of the art transparent conducting materials are semiconducting doped indium oxide (ITO, In_2O_3), zinc oxide (ZnO) or tin oxide (SnO_2)[24], as well as ternary compounds based on their combinations[2]. ITO is commercially available with T ≈ 80% and R_s as low as 10 Ω/□ on glass, and ~60−300 Ω/□ on polyethylene terephthalate. Note that T is typically quoted at 550 nm, as this is where the spectral response of the human eye is highest.

Silver nanowires (AgNWs), single and multiwall carbon nanotubes (SW-CNTs, MW-CNTs), and metal grids have also been explored as potential transparent conductors. Functional transparent conducting films based on these materials would likely require thick samples which would decrease the resulting transmittance (Figure 1.5a). An ideal intrinsic SLG is calculated to have $R_s \approx 6$ kΩ/□ with T ≈ 97.7%. While the transmittance is much higher than ITO, the sheet resistance is far worse (Figure 1.6c). However, stacking graphene into few layers serves to lower the sheet resistance while maintaining relatively good transmittance[22]. A four-layer sample of

graphene (Figure 1.5b) would have an Rs < 100 Ω/□ and a T > 90%. In addition to the good transparency, graphene films tend to be chemically and mechanically stable, and easier to process using standard lithography films compared to ITO. Chemical vapor deposition synthesis of graphene may be a viable way to achieve tailored thicknesses[3-5] of graphene with acceptable transparencies suitable for optoelectronic applications. Because the absorption spectrum of single layer graphene is quite flat from 300 – 2500 nm,[28] it potentially can be used for IR shielding for stealth technology. Additionally, graphene can be implemented into photodetection, because of its ability to absorb light and convert it into electrical current.[27,28,35]

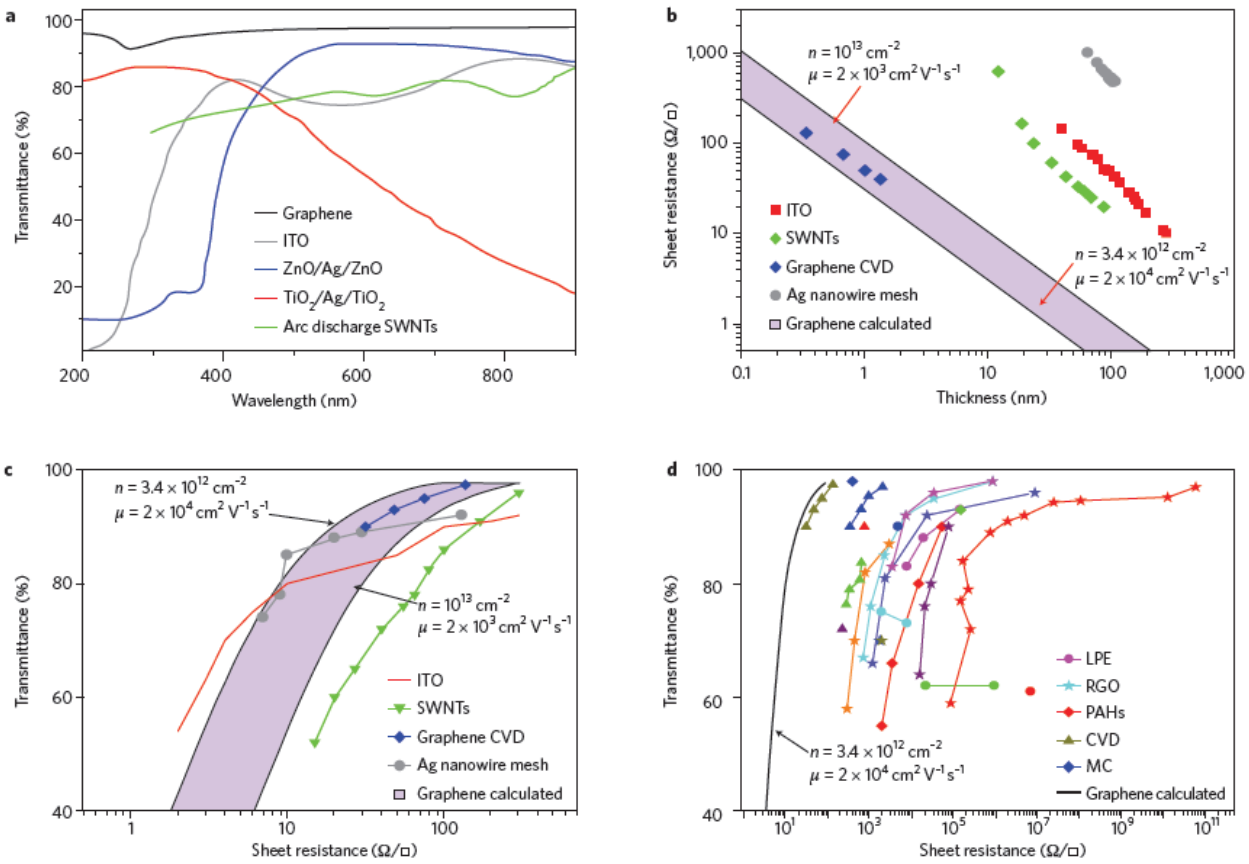

Figure 1.6 | Graphene as a transparent conducting film (GTCF) a. Transmittance for different transparent conductors: GTCFs, single-walled carbon nanotubes (SWNTs), ITO, ZnO/Ag/ZnO TiO_2/Ag/TiO_2. **b.** Thickness dependence of the sheet resistance. The blue rhombuses show roll-to-roll GTCFs based on CVD-grown graphene; red squares, ITO; grey dots, metal nanowires; green rhombuses, SWNTs. **c.** Transmittance versus sheet resistance for different transparent conductors: blue rhombuses, roll-to-roll GTCFs based on CVD-grown graphene; red line, ITO; grey dots, metal nanowires; green triangles, SWNTs. **d.** Transmittance versus sheet resistance for GTCFs grouped according to production strategies: triangles, CVD; blue rhombuses, micromechanical cleavage (MC); red rhombuses, organic synthesis from polyaromatic hydrocarbons (PAHs); dots, liquid-phase exfoliation (LPE) of pristine graphene; and stars, reduced graphene oxide (RGO). A theoretical line is also plotted for comparison. (reprinted with permission[21] © Nature Publishing Group).

Mechanical Properties:

Graphene is thought to be the strongest material known because its intrinsic strength is predicted to exceed that of any other material[30]. Hone et al. took mechanically exfoliated graphene and suspended it over wells etched into Si/SiO_2[29]. The elastic properties and intrinsic breaking

strength of freestanding monolayer graphene membranes were measured by nanoindentation in an atomic force microscope. A schematic of the test is shown in Figure 1.8.

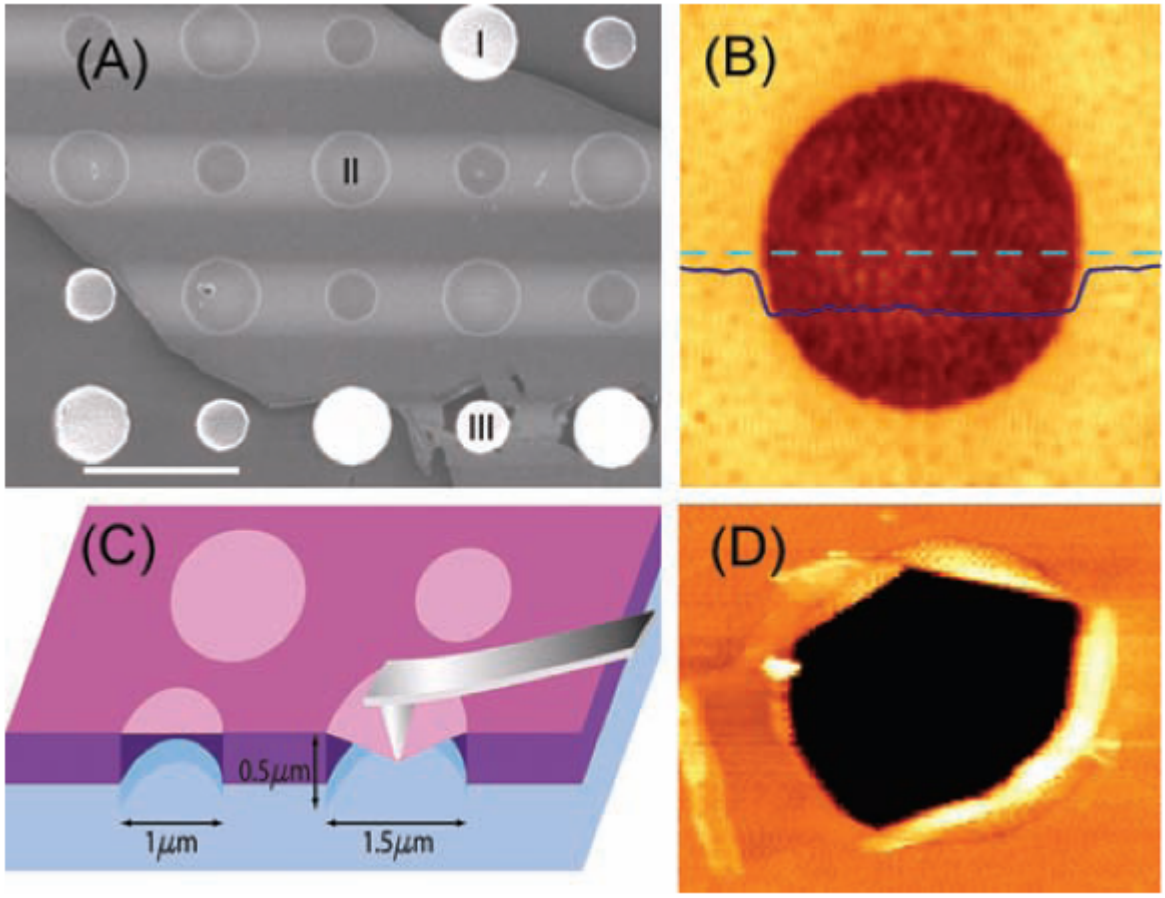

Figure 1.7 | Experimental set-up for the mechanical testing of exfoliated monolayer graphene: a. SEM of suspended monolayer graphene spanning an array of circular holes 1 μm and 1.5 μm in diameter. **b.** Noncontact mode AFM image of one membrane, 1.5 μm in diameter. The solid blue line is a height profile along the dashed line. The step height at the edge of the membrane is about 2.5 nm. **c.** The nanoindentation on suspended graphene membrane **d.** AFM image of a fractured membrane. (reprinted with permission[29] © American Association for the Advancement of Science (AAAS)).

The choice of AFM nanoindentation over pre-etched wells allowed for the suspended graphene sheets to clamp around the entire circumference of the hole rather than on just two points in the case of carbon nanotubes. The elastic stiffnesses measured were 340 newtons per meter ($N \cdot m^{-1}$) and -690 $N \cdot m^{-1}$, respectively. The breaking strength is 42 $N \cdot m^{-1}$ and represents the intrinsic

strength of a defect-free sheet. These quantities correspond to a Young's modulus of E = 1.0 terapascals (Figure 1.9A), third-order elastic stiffness of D = –2.0 terapascals, and intrinsic strength of σ_{int} = 130 gigapascals for bulk graphite. These experiments establish graphene as the strongest material ever measured, and show that atomically perfect nanoscale materials can be mechanically tested to deformations well beyond the linear regime.

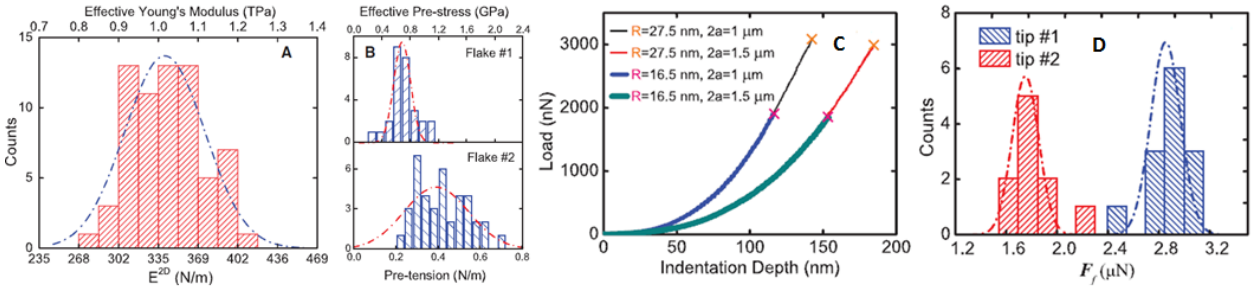

Figure 1.8 | The elastic response and fracture testing behaviour of exfoliated monolayer graphene. **a.** Histogram of elastic stiffness. **b.** Histogram of film pretensions. **c**. Four typical tests, with different tip radii and film diameters; fracture loads are indicated by × marks. **d.** Histogram and Gaussian distribution of breaking force for both tips. (reprinted with permission[30] © American Association for the Advancement of Science (AAAS)).

In contrast to mechanically exfoliated graphite which tends to produce single crystals of graphene, large-area graphene films produced by CVD are polycrystalline and thus contain grain boundaries that can potentially weaken the material. Nanoindentation[32] studies reveal that for CVD-graphene films with different grain sizes, the elastic stiffness of CVD-graphene is identical to that of pristine graphene if post-processing steps avoid damage or rippling (Figure 1.9). Its strength is only slightly reduced despite the existence of grain boundaries. The measured fracture loads for large grain (LG) and (SG) membranes (identified by TEM in the study) are shown in Figure 1.8a and b. The measured values are similar to the exfoliated graphene studies despite the presence of grain boundaries. Elastic moduli of 324 ± 13, 339 ± 17, and 328 ± 17 N/m (which correspond to a 3D Young's modulus of ~1 TPa) were obtained for pristine, LG, and SG graphene, respectively. The presence of wrinkles and small patches of multilayer graphene

account for the wider distributions observed. Fracture loads of 3410 ± 260, 3370 ± 340, and 2590 ± 380 nN were measured for the pristine, LG, and SG films, respectively. The difference in the SG films indicates that the strength is influenced by the randomly occurring defects and grain boundaries in the membranes, although this value is much higher than previously measured. This study unequivocally establishes CVD-graphene as a large-area, high-strength material for flexible electronics and strengthening components.

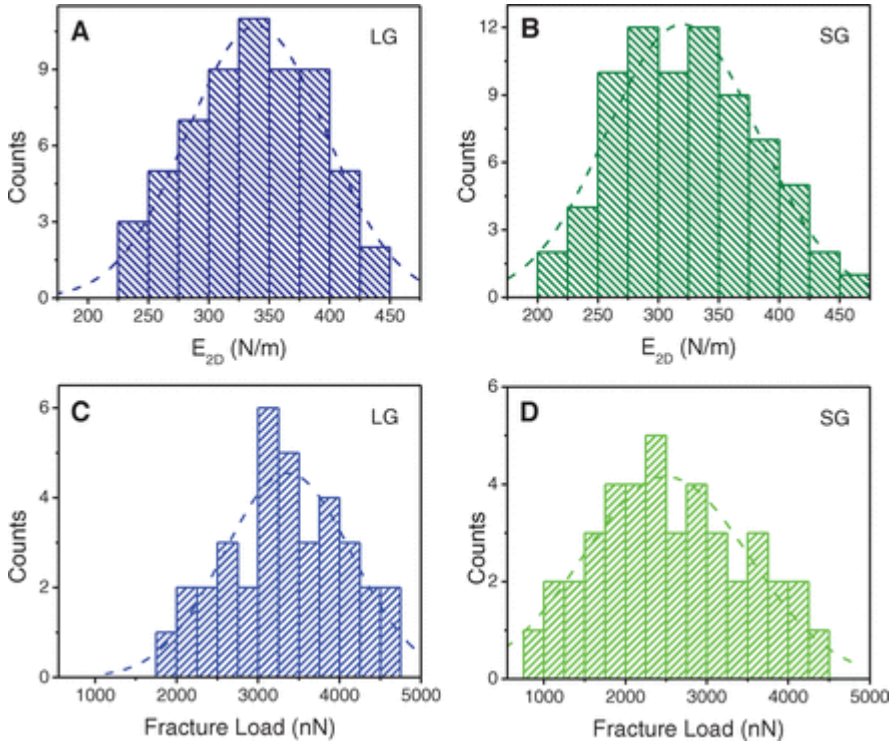

Figure 1.9 | The elastic response and fracture behaviour of CVD grown monolayer graphene: a. The histograms of the elastic stiffness of large grain (LG) graphene films. **b.** The histograms of small grain (sg) graphene films. **c.** Histograms of fracture load for LG films **d.** Histograms of fracture load for SG films. (reprinted with permission[31] © American Association for the Advancement of Science (AAAS)).

Conclusions and Outlook for Graphene:

The intrinsic electronic, thermal, optical, and mechanical properties of graphene are consequence of its underlying sp^2 bonded honeycomb lattice. Graphene allows for the ballistic transport of

carriers through its conjugated carbon lattice, is the best thermal conductor known, exhibits high transmission of visible light, and is the strongest material measured by far. A great deal of progress[36-41] has been accomplished since graphene's first isolation in 2004. The physical and optoelectronic properties of this material have been extensively studied as evident in this chapter. The next frontier of research will focus on the large scale synthesis and incorporation of this wondrous material into the macroscale. Additionally, graphene has paved the way for the study of other 2D materials, although they do not exhibit the same chemical stability as graphene.

This thesis accounts for several significant advances to the fields of graphene namely in synthesis/isolation, characterization and device applications. The chapters herein focus heavily on Bottom-up approaches but do highlight some Top-down routes to graphene.

Synthetic routes are only a single focus of this dissertation, certainly application of graphene is a top priority and there will also be an emphasis on how these different approaches have afforded unique opportunities to explore graphene's properties. We explore the use of graphene as a both a transparent electrode for use in conducting AFM measurements and for vertical alignment of conjugated polymers for sensors, electronics, and organic photovoltaic cells. We also explore the use of graphene as an atomically thin membrane for use in size selective filtration.

References:

1 Novoselov, Kostya S., et al. "Electric field effect in atomically thin carbon films." science 306.5696 (2004): 666-669 doi: 10.1126/science.1102896 (2004).

2 Novoselov, K. S., et al. "Two-dimensional atomic crystals." Proceedings of the National Academy of Sciences of the United States of America 102.30 (2005): 10451-10453. doi: 10.1073/pnas.0502848102 (2005)

3 Li, Xuesong, et al. "Large-area synthesis of high-quality and uniform graphene films on copper foils." *Science* **324**.5932, 1312-1314, doi: 10.1126/science.1171245 (2009).

4 Hass, J., W. A. De Heer, and E. H. Conrad. "The growth and morphology of epitaxial multilayer graphene." *Journal of Physics: Condensed Matter* **20**.32, 323202, doi: 10.1088/0953-8984/20/32/323202 (2008)

5 Li, Dan, et al. "Processable aqueous dispersions of graphene nanosheets." *Nature nanotechnology* **3**.2, 101-105, doi: 10.1038/nnano.2007.451 (2008)

6 Allen, Matthew J., Vincent C. Tung, and Richard B. Kaner. "Honeycomb carbon: a review of graphene." *Chemical reviews* **110**.1, 132-145, doi: 10.1021/cr900070d (2009)

7 Novoselov, K. S. A., et al. "Two-dimensional gas of massless Dirac fermions in graphene." *Nature* **438**.7065, 197-200, doi: 10.1038/nature04233 (2005).

8 Geim, Andre K., and Konstantin S. Novoselov. "The rise of graphene." *Nature materials* **6**.3, 183-191, doi: 10.1038/nmat1849 (2007)

9 Novoselov, Konstantin S., et al. "Room-temperature quantum Hall effect in graphene." *Science* **315**.5817, 1379-1379 doi: 10.1126/science.1137201 (2007).

10 Neto, AH Castro, et al. "The electronic properties of graphene." *Reviews of modern physics* **81**.1, 109, doi: 10.1103/RevModPhys.81.109 (2009)

11 Avouris, Phaedon. "Graphene: electronic and photonic properties and devices." *Nano letters* **10**.11, 4285-4294, doi: 10.1021/nl102824h (2014)

12 Zhang, Yuanbo, et al. "Experimental observation of the quantum Hall effect and Berry's phase in graphene." *Nature* **438**.7065, 201-204, doi: 10.1038/nature04235 (2005)

13 Zhang, Yuanbo, et al. "Direct observation of a widely tunable bandgap in bilayer graphene." *Nature* **459**.7248, 820-823, doi: 10.1038/nature08105 (2009)

14 Bao, W., et al. "Stacking-dependent band gap and quantum transport in trilayer graphene." *Nature Physics* **7**.12, 948-952, doi: (2011)

15 Balog, Richard, et al. "Bandgap opening in graphene induced by patterned hydrogen adsorption." *Nature materials* **9**.4, 315-319, doi: 10.1038/nmat2710 (2010)

16 Balandin, Alexander A. "Thermal properties of graphene and nanostructured carbon materials." *Nature materials* **10**.8, 569-581, doi: 10.1038/nmat3064 (2011)

17 Lee, Jae-Ung, et al. "Thermal conductivity of suspended pristine graphene measured by Raman spectroscopy." *Physical Review B* **83**.8, 081419, doi:10.1103/PhysRevB.83.081419 (2011)

18 Mak, Kin Fai, Jie Shan, and Tony F. Heinz. "Seeing many-body effects in single-and few-layer graphene: observation of two-dimensional saddle-point excitons." *Phys. Rev. Lett*. **106**, 046401, doi: 10.1103/PhysRevLett.106.046401 (2011)

19 Cai, Weiwei, et al. "Thermal transport in suspended and supported monolayer graphene grown by chemical vapor deposition." *Nano letters* **10**.5, 1645-1651.doi: 10.1021/nl9041966 (2010)

20 Kuzmenko, A. B., et al. "Universal optical conductance of graphite." *Physical review letters* **100**.11, 117401, doi: 10.1103/PhysRevLett.100.117401 (2008)

21 Bonaccorso, Francesco, et al. "Graphene photonics and optoelectronics." *Nature Photonics* **4**.9, 611-622, doi: 10.1038/nphoton.2010.186 (2010).

22 De, Sukanta, and Jonathan N. Coleman. "Are there fundamental limitations on the sheet resistance and transmittance of thin graphene films?." *Acs Nano* **4**.5, 2713-2720, doi: 10.1021/nn100343f (2010)

23 Casiraghi, C., et al. "Raman fingerprint of charged impurities in graphene." *Applied Physics Letters* **91**.23, 233108, doi: 10.1063/1.2818692 (2007)

24 Sahu, D. R., Shin-Yuan Lin, and Jow-Lay Huang. "ZnO/Ag/ZnO multilayer films for the application of a very low resistance transparent electrode." *Applied Surface Science* **252**.20, 7509-7514, doi: 10.1016/j.apsusc.2005.09.021 (2006)

25 Becerril, Hector A., et al. "Evaluation of solution-processed reduced graphene oxide films as transparent conductors." *ACS nano* **2**.3, 463-470, doi:10.1021/nn700375n (2008)

26 Wang, Xuan, Linjie Zhi, and Klaus Müllen. "Transparent, conductive graphene electrodes for dye-sensitized solar cells." Nano letters 8.1, 323-327, doi: 10.1021/nl072838r (2008).

27 Wan, Xiangjian, Yi Huang, and Yongsheng Chen. "Focusing on energy and optoelectronic applications: a journey for graphene and graphene oxide at large scale." *Accounts of chemical research* **45**.4, 598-607, doi: 10.1021/ar200229q (2012)

28 Bao, Qiaoliang, and Kian Ping Loh. "Graphene photonics, plasmonics, and broadband optoelectronic devices." *ACS nano* **6**.5, 3677-3694, doi: 10.1021/nn300989g (2012)

29 Lee, Changgu, et al. "Measurement of the elastic properties and intrinsic strength of monolayer graphene." *Science* **321**.5887, 385-388, doi: 10.1126/science.1157996 (2008).

30 Zhao, Qingzhong, Marco Buongiorno Nardelli, and J. Bernholc. "Ultimate strength of carbon nanotubes: a theoretical study." *Physical Review B* **65**.14, 144105, doi: 10.1103/PhysRevB.65.144105 (2002)

31 Lee, Gwan-Hyoung, et al. "High-strength chemical-vapor–deposited graphene and grain boundaries." *Science* **340**.6136, 1073-1076, doi: (2013)

32 Huang, Pinshane Y., et al. "Grains and grain boundaries in single-layer graphene atomic patchwork quilts." *Nature* **469**.7330, 389-392, doi: 10.1038/nature09718 (2011)

33 Ruiz-Vargas, Carlos S., et al. "Softened elastic response and unzipping in chemical vapor deposition graphene membranes." *Nano letters* **11**.6, 2259-2263, doi: 10.1021/nl200429 (2011)

34 Kim, Kinam, et al. "A role for graphene in silicon-based semiconductor devices." *Nature* **479**.7373, 338-344, doi: 10.1038/nature10680 (2011)

35 Mueller, Thomas, Fengnian Xia, and Phaedon Avouris. "Graphene photodetectors for high-speed optical communications." *Nature Photonics* **4**.5, 297-301, doi: 10.1038/nphoton.2010.40 (2010)

36 El-Kady, Maher F., et al. "Laser scribing of high-performance and flexible graphene-based electrochemical capacitors." *Science* **335**.6074, 1326-1330, doi: 10.1126/science.1216744 (2012)

37 Stoller, Meryl D., et al. "Graphene-based ultracapacitors." *Nano letters* **8**.10, 3498-3502, doi: 10.1021/nl802558y (2008)

38 Sanchez, Vanesa C., et al. "Biological interactions of graphene-family nanomaterials: an interdisciplinary review." *Chemical research in toxicology* **25**.1, 15-34, doi: 10.1021/tx200339h (2011)

39 Tang, Haixiong, et al. "Highly efficient synthesis of graphene nanocomposites." *Nano letters* **12**.1, 84-90, doi: 10.1021/nl203023k (2011)

40 Bae, Sukang, et al. "Roll-to-roll production of 30-inch graphene films for transparent electrodes." *Nature nanotechnology* **5**.8, 574-578, doi: 10.1038/nnano.2010.132 (2010)

41 Hu, Wenbing, et al. "Graphene-based antibacterial paper." *Acs Nano* **4**.7, 4317-4323, doi: 10.1021/nn101097v (2010)

42 Yan, Hugen, et al. "Infrared spectroscopy of wafer-scale graphene." *ACS Nano* **5**.12 9854-9860, doi: 10.1021/nn203506n (2011)

Chapter 2: Synthesis of Single and Few Layer Graphene via Chemical Vapor Deposition (CVD):

Chemical vapor deposition (CVD) has emerged as a powerful tool to grow high quality films of graphene of various thicknesses and on a variety of substrates[1–4]. Unlike mechanical exfoliation, large area coverage up to 30 in. along the diagonal can be achieved via CVD[5]. It is now possible to grow graphene with carrier mobility values in excess of 7100 $cm^2V^{-1}s^{-1}$ at room temperature,[6] which is close to the results on SiO_2/Si with graphene exfoliated from HOPG or Kish graphite. The high carrier mobility and size scalability make CVD graphene a promising material for applications such as integrated high frequency electronics. A schematic of a typical CVD reactor used for graphene growth is illustrated in Figure 2.1. The thin film process of CVD is a "Bottom-up" molecular synthesis technique driven by thermodynamics and kinetics of the precursor chemistry, the dynamics of heat and mass transport and the physics of surface adsorption and crystal growth. This process is well suited for synthesizing coatings that are of high purity and of a controlled thickness (typically a few microns in thickness). It is this general tailorability that makes CVD a promising tool for high quality graphene synthesis.

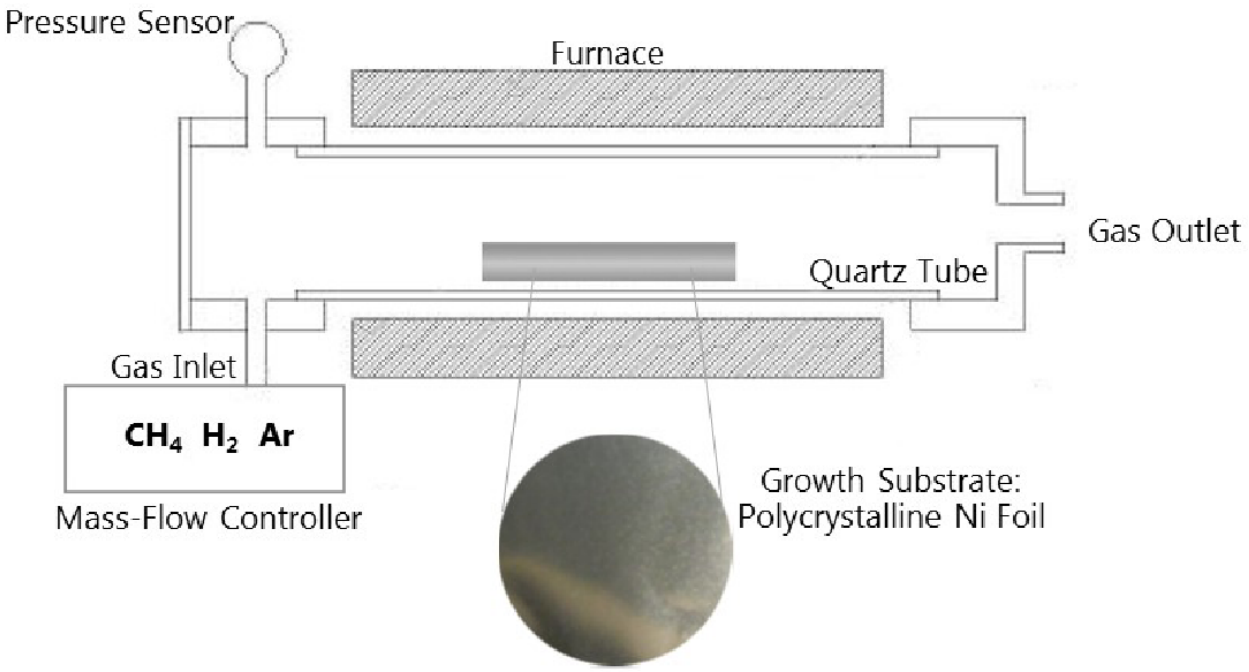

Figure 2.1 | Schematic of a Chemical Vapor Deposition reactor that can be used to grow graphene. A catalytic surface (i.e. copper, nickel, etc.) is placed into the growth chamber and a controlled amount of precursor gases are fed from inlet to outlet. Parameters such as temperature, feed rate, pressure, cooling rate, etc. become important for high quality growth of films.

Several factors are important in controlling the number of layers of CVD-grown graphene[8-11]. Chief among them is the concentration of the precursor carbon source. Utilizing our home built CVD reactor, we investigated the effect of carbon concentration from alkane gases on graphene growth. We compared ethane and propane to methane, which have two and three times the amount of carbon, respectively. We systematically varied the pressure of the hydrocarbon precursors to examine the effect of carbon concentration. We utilized low pressure CVD conditions (LPCVD) for the growths and varied it (250–1000 mTorr), while other conditions

such as flow rate, temperature, and time were fixed. Figure 2.2 shows optical micrographs (OM) of transferred graphene films that were grown with methane, ethane, and propane. They were transferred onto silicon substrates with a 300 nm oxide layer to provide contrast for imaging.

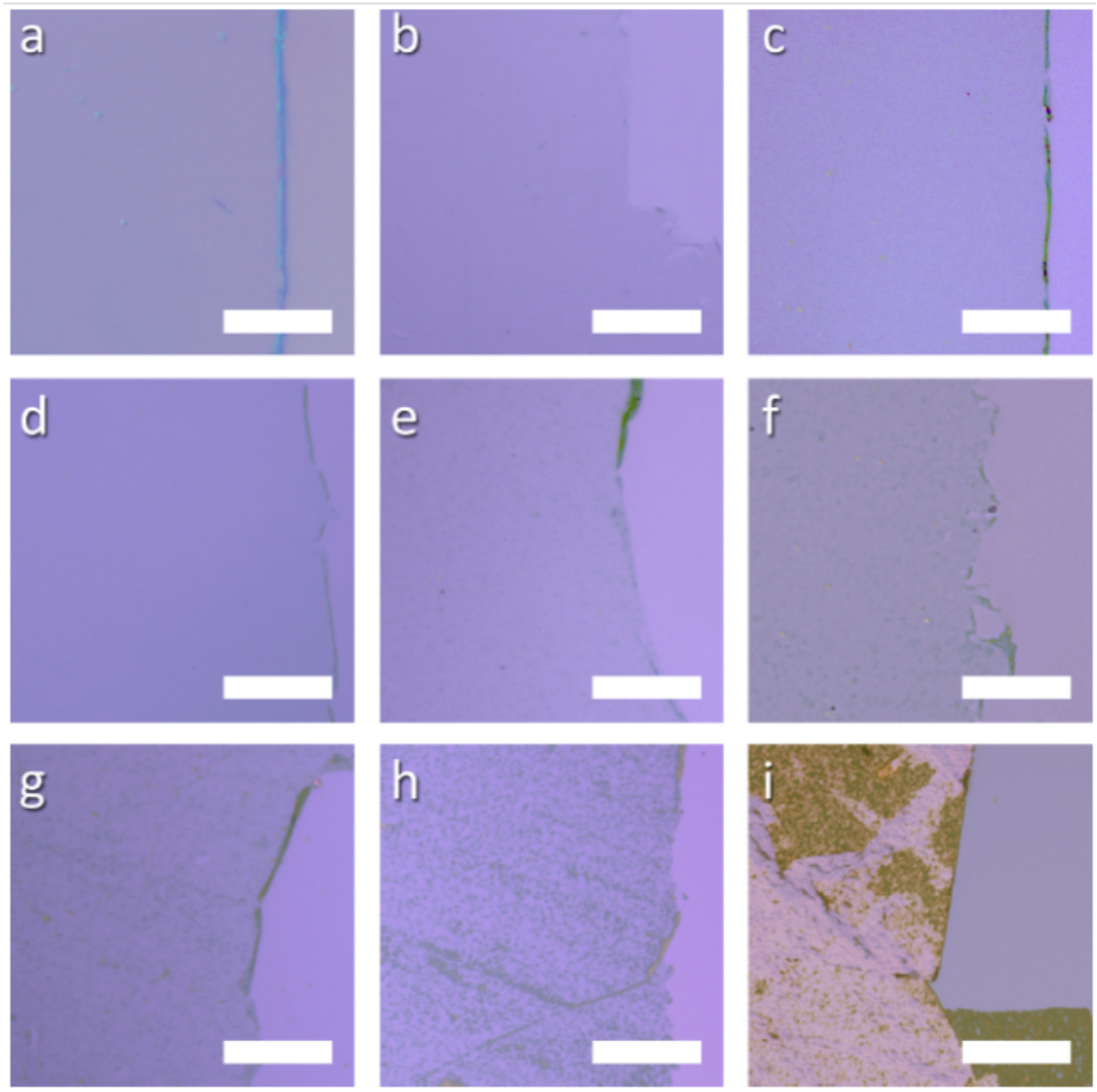

Figure 2.2 | Optical micrographs of LPCVD grown graphene films transferred onto Si/SiO_2. Graphene grown with methane **a–c**, ethane **d–f**, and propane **g–i** at 250, 500, and 1000 mTorr growth pressures, respectively. Scale bar represents 20 μm. (reprinted with permission30 ©2012 WILEY-VCH Verlag GmbH & Co. KGaA, Weinheim)

As the carbon concentration increases, the transferred films become increasingly darker because additional layers interfere with the reflected light[12]. As the hydrocarbon precursor gas increases in carbon content, the resulting films become increasingly thicker with variability in quality. Figure 2.3 demonstrates that transmittance at 550 nm for graphene decreases with the carbon content of the precursor gas as expected. Each layer of graphene absorbs about 2.3% of the incident light and this relation can be used to determine the number of layers of graphene grown (each layer of graphene is 0.334 nm thick).

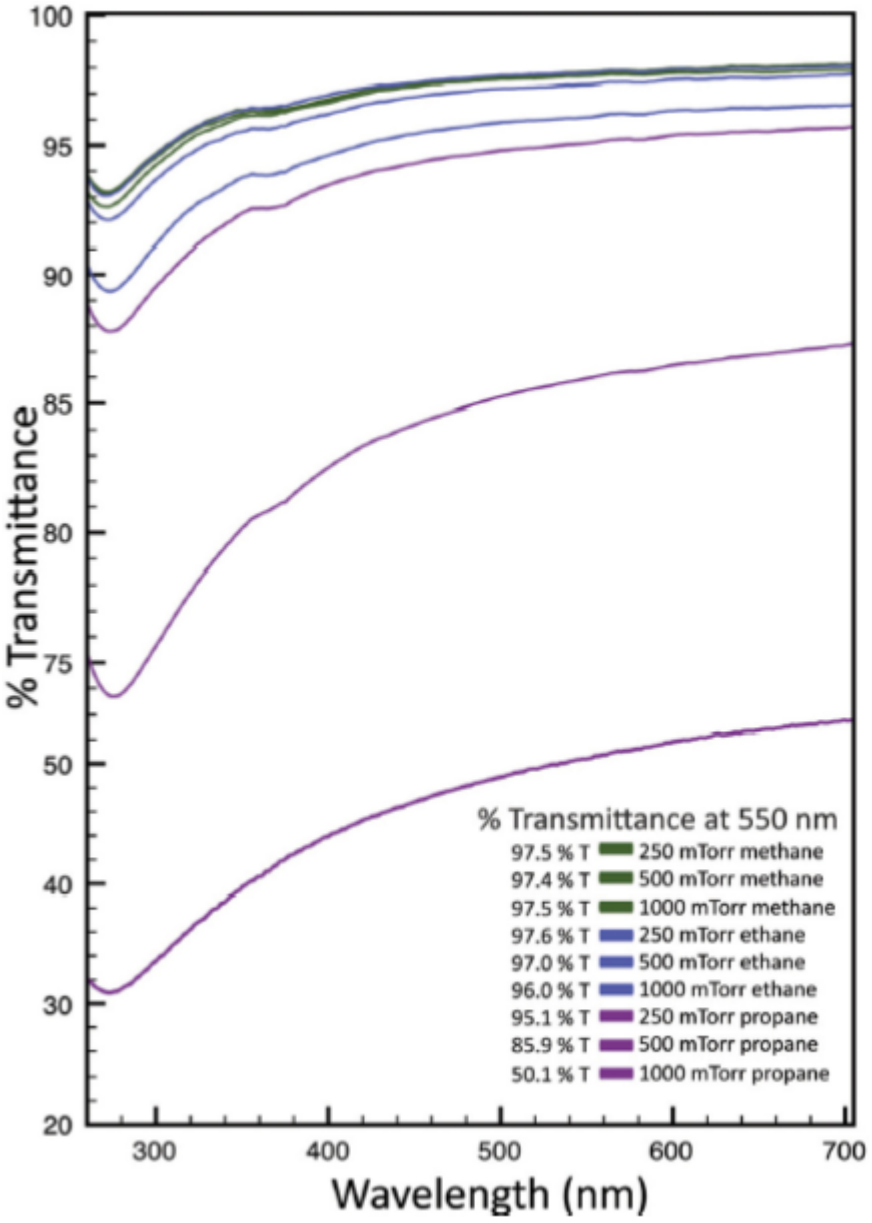

Figure 2.3 | UV-Vis transmittance of graphene films as a function of precursor gas. As the graphene increases in film thickness, the transmittance decreases. (reprinted with permission30 ©2012 WILEY-VCH Verlag GmbH & Co. KGaA, Weinheim)

Increasing carbon content leads to bilayer selectivity:

The graphene grown from ethane gas shows a significant change when the pressure is increased; bilayer graphene becomes the dominant form. We increase the pressure of the total system by

increasing the amount of precursor gas which increases the amount of carbon available for graphene formation. High-resolution SEM images of ethane-synthesized graphene (Figure 2.4) reveal darker, more conductive bilayer regions covering the first layer. The SEM images of ethane-grown graphene were used, in conjunction with ImageJ freeware, to calculate the type and percent coverage of graphene based on relative color intensities. The analysis infers that up to 75% bilayer graphene can be grown with ethane at 1000 mTorr pressure, and is graphed in Figure 2.4f. Under these growth conditions, methane yields predominantly single-layer graphene; therefore, SEM analysis was not performed. It should be noted that even using methane some multilayer graphene is produced due to the nature of the growth of graphene on copper surfaces.[13]

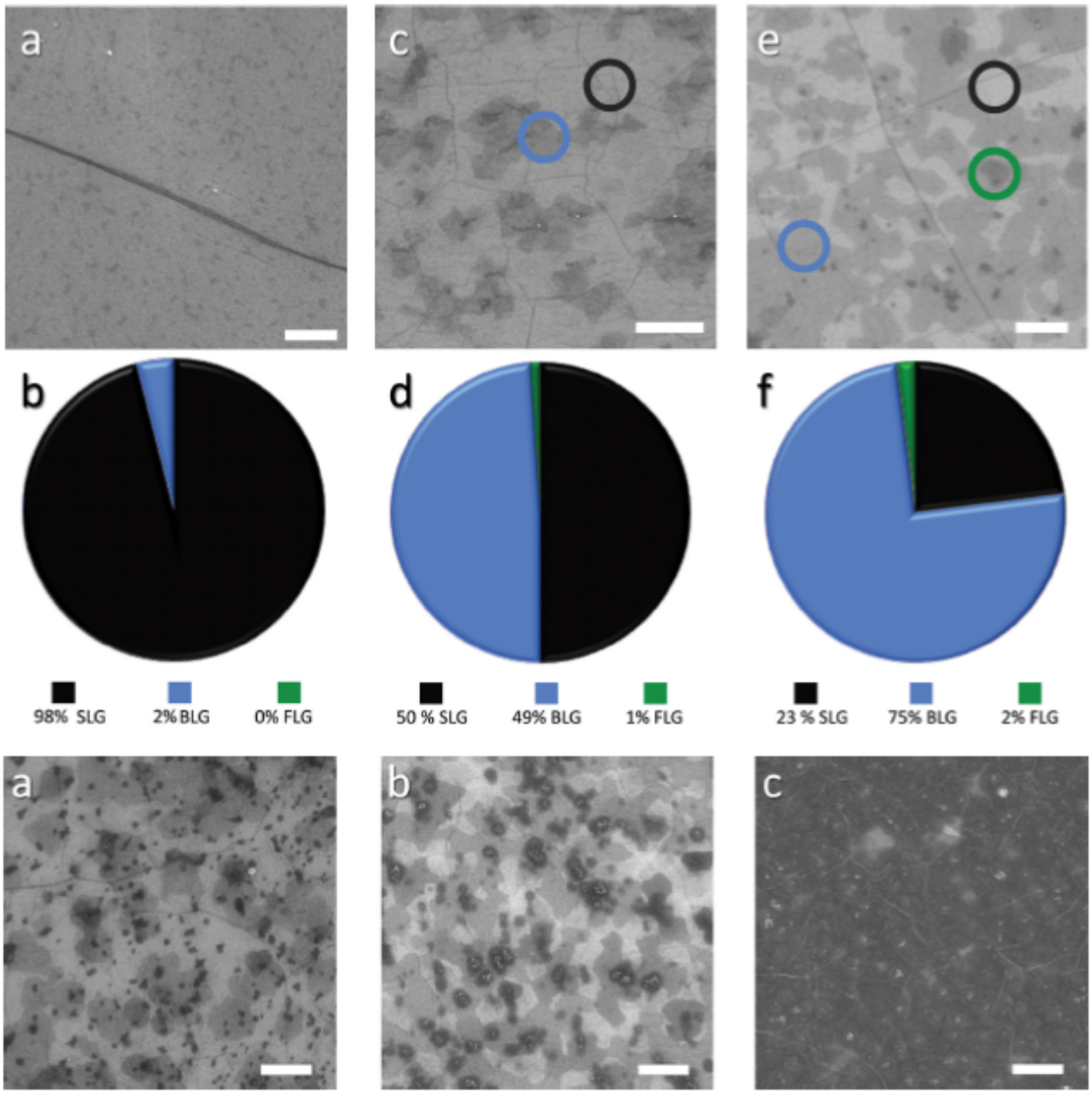

Figure 2.4 | Scanning electron micrographs of graphene grown with ethane at increasing pressures: a. 250, **c.** 500 and **e.** 1000 (mTorr) show the appearance and growth of a second layer. Coverage statistics (**b, d, f**) were tabulated and graphed to illustrate the growth trends of graphene layers at different pressures. At 250 mTorr **a.** a single layer (black circle) is controllably grown, but at 500 mTorr **c.** ~49% bilayer coverage (blue circle) is observed with 1% few-layer graphene (green circle), and at 1000 mTorr**, e.** ~75% bilayer coverage is observed with small regions containing ~2% few-layer graphene. Scale bars represent 1 μm. (reprinted with permission30 ©2012 WILEY-VCH Verlag GmbH & Co. KGaA, Weinheim)

Propane when used as a precursor produces multilayer graphene with turbostratic ordering. Raman spectroscopy was used to assist in quantitatively determining the number of layers of graphene and to gauge the crystallinity by noting changes in the spectral fingerprint (Figure 2.5).[14]

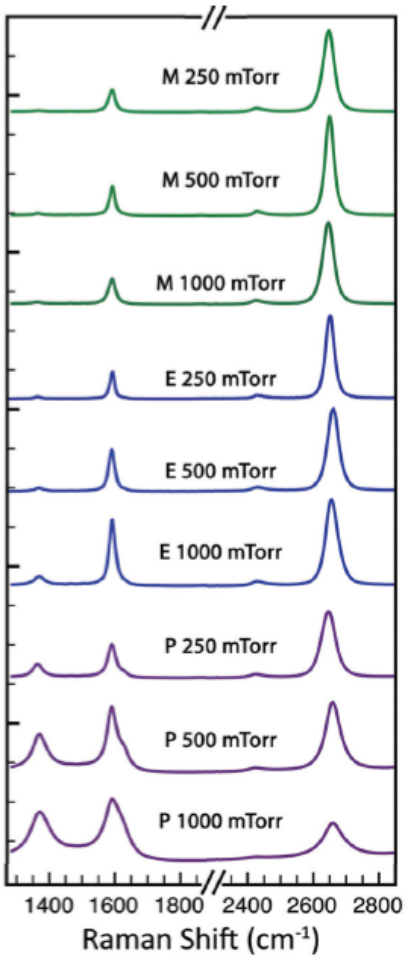

Figure 2.5 | Raman spectra of graphene films grown at varying pressures and hydrocarbon precursors: a. Overall trend in graphene crystallinity as a function of pressure. Spectra were measured with a low-power laser, at wavelength of 514 nm. M: methane, E: ethane, and P: propane. (reprinted with permission30 ©2012 WILEY-VCH Verlag GmbH & Co. KGaA, Weinheim)

Graphene growths with methane (at all pressures) show the characteristic Raman signals for single-layer graphene and have the expected 2D:G peak intensities of roughly 3.0-4.0. Ethane derived graphene shows single and bilayer Raman signatures that vary as the pressure (carbon concentration) is increased. The Raman spectra resulting from propane show the presence of a disorder peak, D (~345 cm^{-1}), and a D′ (~1615 cm^{-1}) peak, budding from the G peak. Furthermore, the intensity of the D peak linearly increases with the growth pressure of propane. The increasing disorder is suggestive of turbostratic graphene, [12] (rotationally disordered multilayer graphene) and also graphene with sp^3 defects.[15] If the mechanism by which graphene forms on copper surfaces is influenced by the availability of copper d-orbitals to stabilize carbon radicals formed during the high temperature decomposition of hydrocarbons, then as the copper surface becomes saturated this catalytic ability is decreased. The combustion and formation of carbon radicals continues at high temperature, but rather than become catalytically converted to sp^2 bonded graphene, it becomes amorphous or turbostratic. We attribute the lower crystallinity of the films to oversaturation from carbon species and from different cracking pathways of the precursors. A closer investigation of ethane growths, Figure 2.6a-c, shows that ethane-grown graphene exhibits a significant change in the 2D band as the pressure is increased from 250 to 1000 mTorr indicative of layering. The normalized Raman allows for studying the nature of the 2D band. At pressures of 500 and 1000 mTorr, the 2D peaks change in shape, width, position, and intensity, indicative of additional layers. The full width at half maximum (FWHM) of the 2D peaks become shifted, broader, and asymmetric. Furthermore, they can be Lorentzian fitted with four bands as a direct consequence of interactions between the multilayer graphene[16-18.]

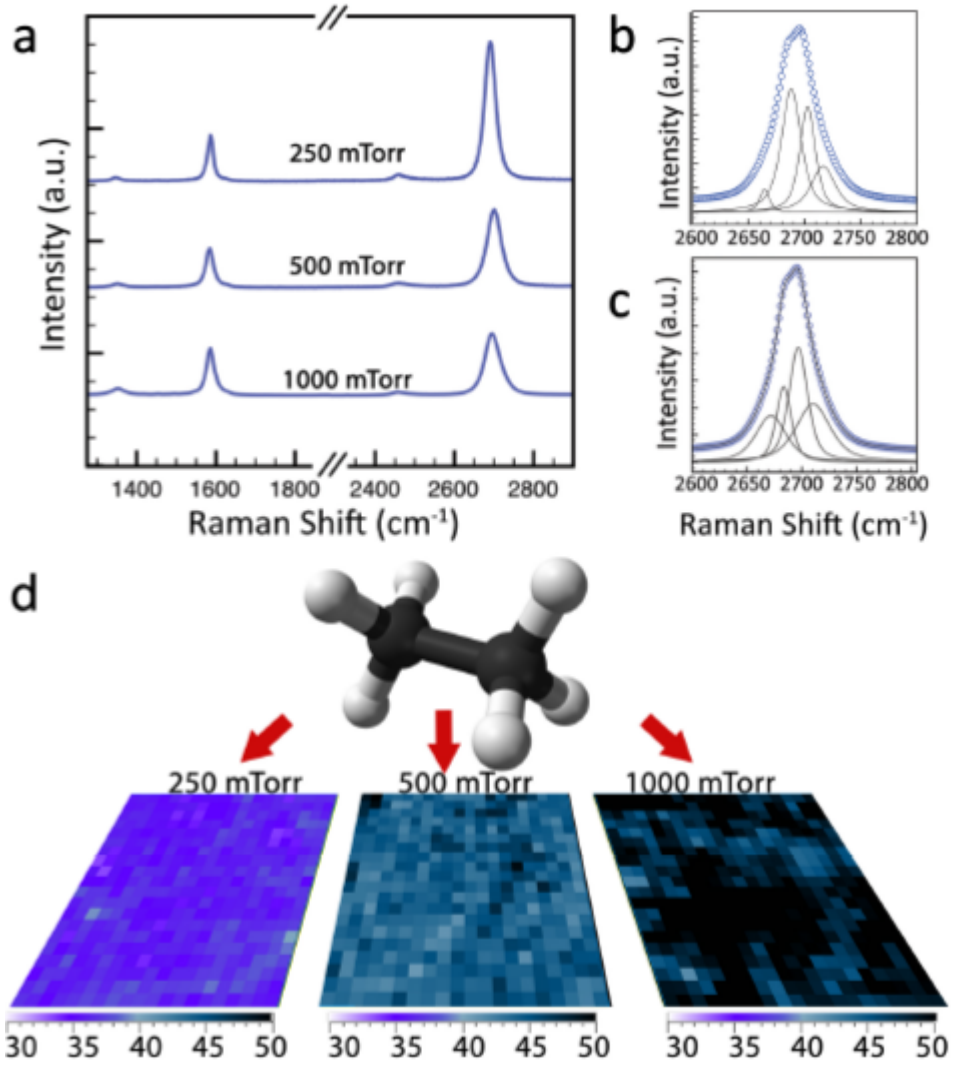

Figure 2.6 | Raman spectroscopy as a function of pressure: a. Raman spectra and maps of graphene films grown at different pressures using ethane. Raman spectra placed in sequence show changes in the G and 2D ratios as a function of pressure. Lorentzian fits of the FWHM from the 2D peaks for graphene grown with ethane at **b**. 500 and **c**. 1000 mTorr show that the 2D band is split into 4 components: 2D1B, 2D1A, 2D2A, 2D2B, indicative of bilayer interaction. **d**. Raman mapping over a 20 μm × 20 μm scan area for the FWHM of the 2D peak shows single- to bilayer graphene areas at different pressure growths with ethane gas. The values of the color gradient bars below are in wavenumbers (cm^{-1}). (reprinted with permission30 ©2012 WILEY-VCH Verlag GmbH & Co. KGaA, Weinheim)

The 2D peaks of graphene grown with ethane at pressures of 250–1000 mTorr were further analyzed through Raman contour mapping of a 400 μm^2 region (Figure 2.6d). The map plots the intensity of the 2D peak (cm^{-1}) for various pressures. The FWHM values of the ethane-grown graphene increase as a function of pressure from ~33 cm^{-1} at 250 mTorr, to ~50 cm^{-1} at 1000 mTorr and are in good agreement with values obtained by other groups.[8, 10]

We next utilized selected area electron diffraction (SAED) via TEM to further understand the crystallographic information of the grown films as well as the type of stacking found in the multilayer samples. Single- and bilayer graphene can be quantitatively identified by peak intensities; the former has a two-atom basis set and the latter a four-atom basis set. The structure factor calculated using these basis values allows us to determine whether the peak intensities are from single layer or bilayer graphene. Additional distinction between single- and bilayer graphene can be obtained by measuring the diffraction peak amplitude as a function of reciprocal space distance. After correcting for the Rutherford cross section and the Debye–Waller effects, the structure factor of the basis for single-layer graphene has a 4:1 value (between the first and second order diffraction peaks) and a 16:1 value for AB bilayer graphene. Single and bilayer samples can be distinguished based on the relative intensity of the inner and outer peaks from the diffraction intensity line profiles collected from SAED. Diffraction patterns shown in Figure 2.7 a–e correspond to graphene grown at 1000 mTorr with methane, 250–1000 mTorr with ethane, and 250 mTorr with propane.

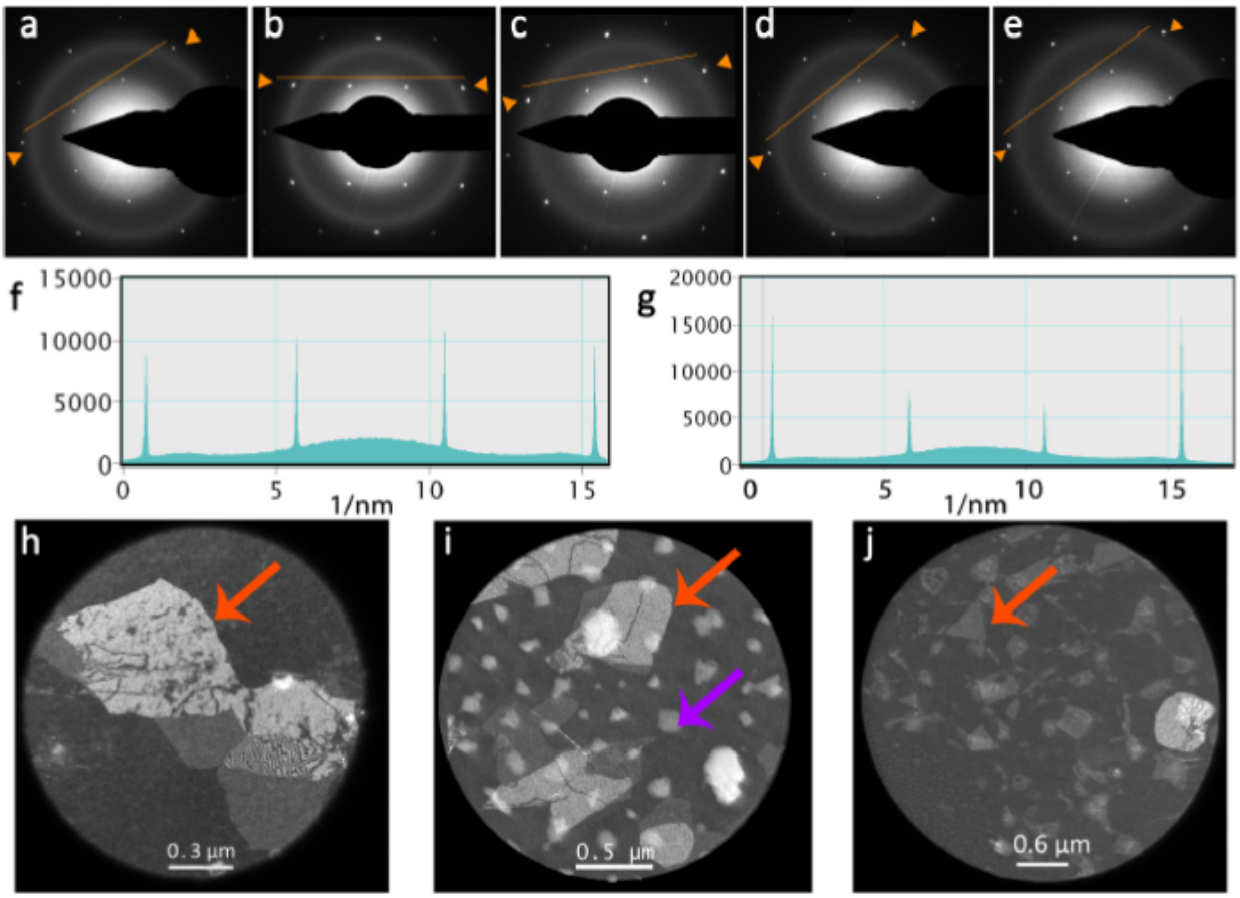

Figure 2.7 | TEM selected area electron diffraction (SAED) patterns of single- and bilayer graphene, diffraction intensity line profiles and low-resolution TEM (LRTEM) images. Normal incident diffraction pattern of **a**. single-layer graphene from methane grown at 1000 mTorr, **b.** single-layer graphene from ethane grown at 250 mTorr, **c., d.** bilayer graphene from ethane at 500 **c** and 1000 **d** mTorr, and **e.** bilayer layer graphene from propane grown at 250 mTorr. Representative line profiles for **f**. single-layer and **g.** bilayer graphene show the differences in diffraction intensities. LRTEM images of graphene grown with ethane at **h.** 500 and **i.** 1000 mTorr and with propane at **j.** 250 mTorr, from many angles, show the actual size of each crystalline domain (red arrows) to be around 500 nm across, although SEM shows the actual coverage is much larger. The purple arrow indicates silicon residue from the etch process. (reprinted with permission30 ©2012 WILEY-VCH Verlag GmbH & Co. KGaA, Weinheim)

SAED analysis shows that films grown with higher pressures of ethane are AB-stacked. The changes in relative peak intensities can be seen in the characteristic line profiles shown in Figure 2.7f (single-layer graphene) and 2.7g (bilayer graphene). The peak intensities (outermost to

innermost) of ~1:1 correspond to single-layer graphene, while ~2:1 represents bilayer graphene. Methane in all cases produced predominately single layer. Graphene grown with ethane at 250 mTorr produces single-layer graphene while at higher pressures exhibits a ratio of 2:1, suggesting AB-stacking in the areas of bilayer coverage. Propane films grown at 250 mTorr produce diffraction patterns indicative of bilayer graphene. Higher pressure propane films were not measured. Images collected at various diffraction angles show the bilayer graphene grown with ethane at 500 and 1000 mTorr (Figure 2.7h, i) and with propane at 250 mTorr (Figure 2.7j) are composed of crystalline facets around 500 nm across, although SEM images show that the actual coverage is much larger.

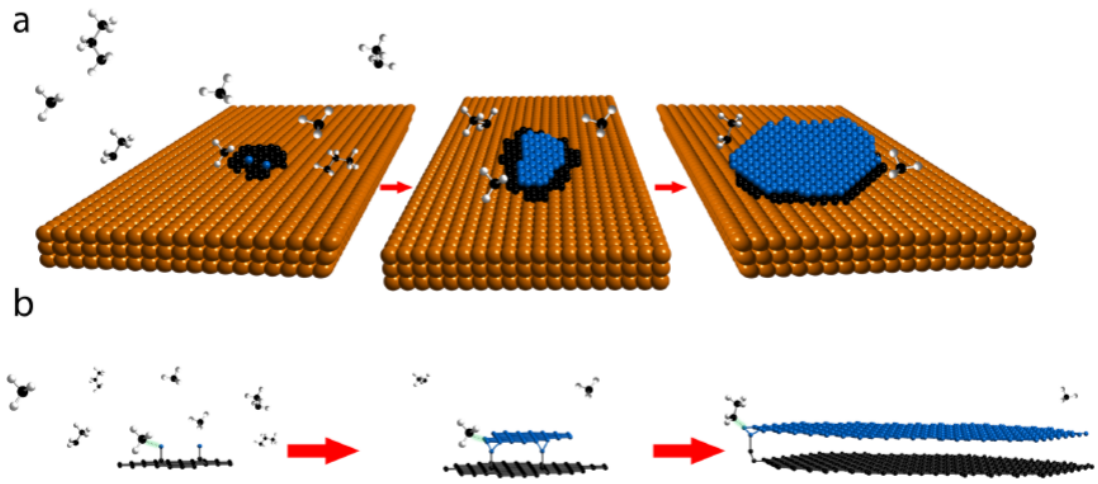

Figure 2.8 | A schematic of bilayer graphene growth with ethane and/or propane feedstock gas: a. Top view is shown with a space-filling model and **b.** Side view is shown with a ball-and-stick model. Copper atoms are shown as orange spheres, carbon in black (first layer) and in blue (second layer), and hydrogen in gray. When the copper catalyst is oversaturated with ethane molecules, secondary growth is observed. Since ethane has a lower decomposition pathway, higher concentrations of carbon radical will participate in secondary growth near the edge, where dangling bonds and defects are more prevalent. (reprinted with permission30 ©2012 WILEY-VCH Verlag GmbH & Co. KGaA, Weinheim)

We proposed that the observation of additional graphene layers with ethane and propane likely results from alkyl radicals or alkenes that react with edges and defects in the previous layer, which favor reaction with incoming reactive carbon species.[10,19] Upon switching from methane to higher alkane precursors, C–H and C–C bond energies become increasingly weaker. The C–H bond energies for methane are 105 kcal per mole versus 100 kcal per mole for ethane or propane (on the primary carbon) and the C–C bond energies for ethane and propane are only 90 and 88 kcal per mole, respectively (Figure 2.8).[20] It has been observed that a methyl radical source can be used to grow graphene on HOPG (highly ordered pyrolytic graphite),[19] and is a possible mechanism for growth of additional graphene layers on top of graphene formed on copper. As the first layer of graphene forms on the surface of copper, dangling bonds exist that may serve as nucleation points for further growth of graphene, laterally at first and then vertically. If the amount of carbon within the reactor is increased, more carbon is brought to the surface and accelerated surface reactions produce secondary graphene such that only a combination of single-/multilayer graphene is observed. A plot of the FWHM values for the Raman 2D peak versus carbon content, Figure 2.9, illustrates that carbon concentration plays a vital role in the graphitization process and the resulting quality of the graphene. In this light, it may be possible to grow uniform single-layer graphene with larger-hydrocarbon gases, provided the feedstock gas is appropriately diluted with a reductive gas such as hydrogen, and the growth time is modified. It may be desirable to utilize alkene feed stocks because these would have even lower cracking temperatures suitable for lower temperature growths or more complete decomposition at higher temperatures.

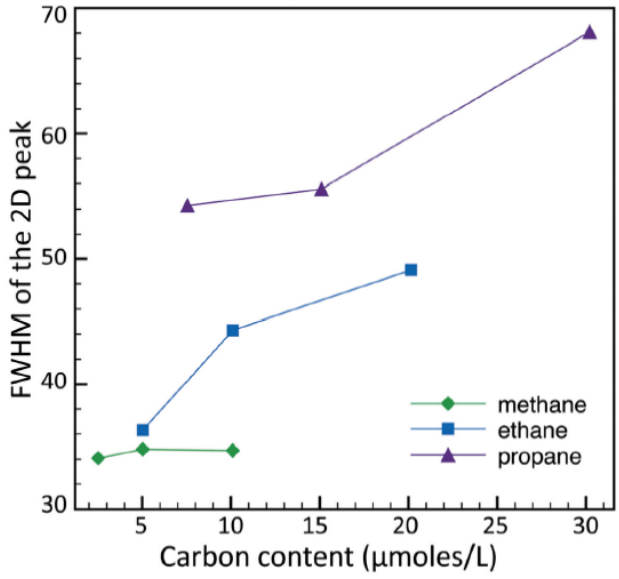

Figure 2.9 | Plot of the full width half maximum (FWHM) of the 2D peak as a function of carbon content. (reprinted with permission30 ©2012 WILEY-VCH Verlag GmbH & Co. KGaA, Weinheim)

Parameters that affect graphene growth

As we have seen, the concentration of the carbon precursor greatly affects the quality and number of layers of the graphene films grown on copper. Pressure too plays an interesting role in the formation of graphene films as does temperature, and nucleation density.

Low pressure and atmospheric pressures:

Early efforts focused on LPCVD (0.5–50 Torr) and many advances were made in making high quality films under low-pressure conditions. Typically flower-shaped domains having lobes and dendritic features usually result from LPCVD. One unique feature of the LPCVD growths is the sublimation of copper at high temperature. Typically, the cold end of the reactor tube will be covered in a thin layer of copper following growth. Atmospheric pressure CVD (APCVD) in contrast gives hexagonal shaped domains. Activation energies differ for low and atmospheric pressure CVD. At low pressure, evaporation of copper is significant and limits carbon nucleation

with a nucleation density barrier activation barrier, E_{nuc} ~4 eV. Copper evaporation is suppressed by atmospheric pressure CVD and the measured E_{nuc} ~9 eV is attributed to desorption energies of active carbon species/graphene critical nuclei[40]. The increase in activation energy indicates that at atmospheric pressures, the nucleation density of graphene decreases by 5 orders of magnitude.

Whether LPCVD or APCVD is utilized for growth, the effect of temperature plays roughly the same role for both. High temperature growths are key to extremely low nucleation density,[21-24] improved uniformity of layer number,[25] and fast growth rates, with activation energy of 2.7 eV.[25]

It is generally the case that the higher the temperature, the smaller the nucleation density, the larger the graphene domains and the more uniform the resulting films.

Optimizing Growth Parameters:

APCVD growth at relatively high temperature is particularly promising for continuously fed roll-to-roll processing. We decided to utilize APCVD and optimize our system to grow the highest quality graphene possible. Figure 2.10 shows the growth of hexagonal domains over a relatively short time frame. The growths were carried out under atmospheric pressure, a temperature of 1050 °C for both annealing and growth, and under a flow rate of 4 standard cubic cm/min (sccm) of methane, 20 sccm of H_2, and 200 scmm of Ar and for periods of time ranging from 0.3 - 64 minutes. At the 2 min mark, the presence of graphene becomes apparent. At the 4 min mark, a film begins to form although there are areas on the copper foil that remain uncovered. A continous film forms from 8 min on.

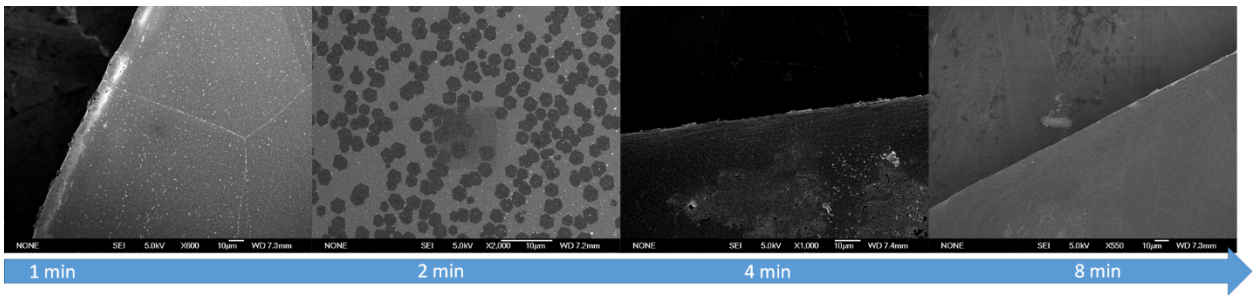

Figure 2.10 | Atmospheric growth of FLG as a function of time: Initially nothing grows below 1 min, but then nucleation begins at the 2 min mark. By 8 min growth has produced a continuous film.

Figure 2.11 reveals some secondary growth on the forming graphene hexagons. A recent study[13] on the growth of bilayer and multilayer graphene on copper foils that was monitored by isotopic labeling of the methane precursor and characterized by Raman suggests that adlayer growth proceeds by catalytic decomposition of methane (or CH_x, $x < 4$) trapped in a "nanochemical vapor deposition" chamber between the first layer and the substrate. During growth at high temperature, the adlayers formed simultaneously and beneath the top, continuous layer of graphene and the Cu substrate. Additionally, the adlayers share the same nucleation

center and all adlayers nucleating in one place have the same edge termination. Once the graphene layers grow laterally they will coalesce and prevent the further growth of multilayers. Certainly we can see that the multilayer spots in the hexagons tend not to grow after larger domains have merged together. Interestingly, the growth of graphene seems to occur in a particular direction, most likely due to the flow of the gases during growth as seen in Figure 2.11c. Figures 2.11d-f show the complete growth of graphene at the 64 min mark. The complete film follows the same directional pattern observed during the initial formation. We continued to increase the hydrogen flow rate in subsequent growths in order to further dilute the concentration of methane. We find that 4 sccms of CH_4, 100 sccms of H_2, and 200 sccms of Ar at atmospheric

pressure and temperatures >1000 °C are sufficient to provide high quality and complete films of graphene.

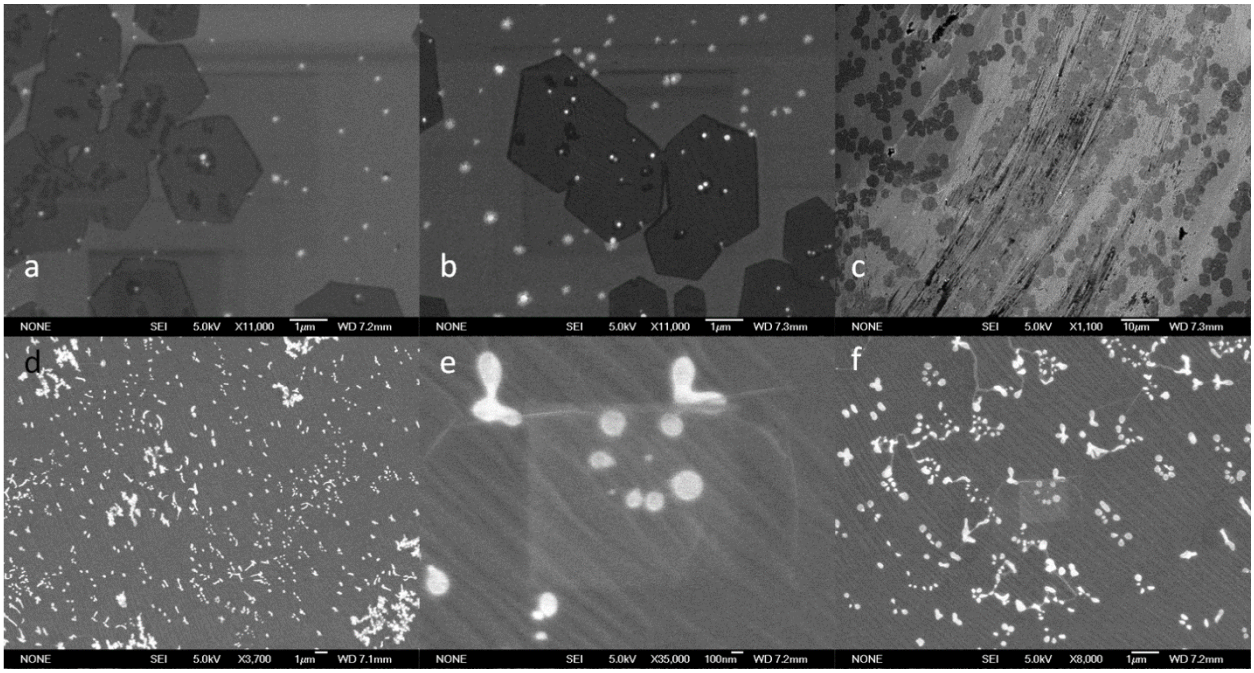

Figure 2.11 | Nucleation of graphene on copper at atmospheric pressure: a. Graphene grows in a hexagonal pattern due to the etching effect of hydrogen. Secondary points of nucleation can be seen on the larger graphene crystals. **b.** Grains continue to grow until they coalesce. **c.** The growth follows the flow of gases in the CVD reactor giving the film a directional quality. **d.** Graphene film after 64 min of growth. The bright colored material is thought to be quartz nanoparticles from the CVD reactor. **e.** The as grown film of graphene appears as a striated surface. **f.** The graphene seems to grow underneath the quartz nanoparticles.

Recently, it has been shown that controlling the formation of a surface oxide on copper[26] may lead to even better control of the graphene nucleation on copper. In the presence of the copper oxide, carbon radicals formed from high temperature decomposition are unable to nucleate on the catalytically unreactive surface. During growth, hydrogen gas is introduced which begins to etch away the copper oxide allowing for nucleation to take place. We decided to test the effects of annealing copper without hydrogen gas at high temperature. We took 25 μm copper foil as received and annealed it at atmospheric pressure under 200 sccms of Ar at 1070 °C for 5 min.

We then introduced 4 sccm of CH_4 and 100 sccm of H_2 into the reaction chamber for 5 min. The resulting growths show decreased nucleation density and enlarged graphene domains (Figure 2.12). The domains of the graphene now appear less hexagonal and more star and dendritic shaped indicating that the absence of hydrogen gas leads to less etching of the domains. The domains are also larger compared to the hydrogen pre-anneal growths, suggesting that in the absence of more nucleated domains, carbon radicals will nucleate and continue to grow laterally thereby getting larger and larger. We find that annealing of copper foils in Ar for a minimum of 10 minutes followed by high temperature growth of graphene gives us the best quality, most complete films to date.

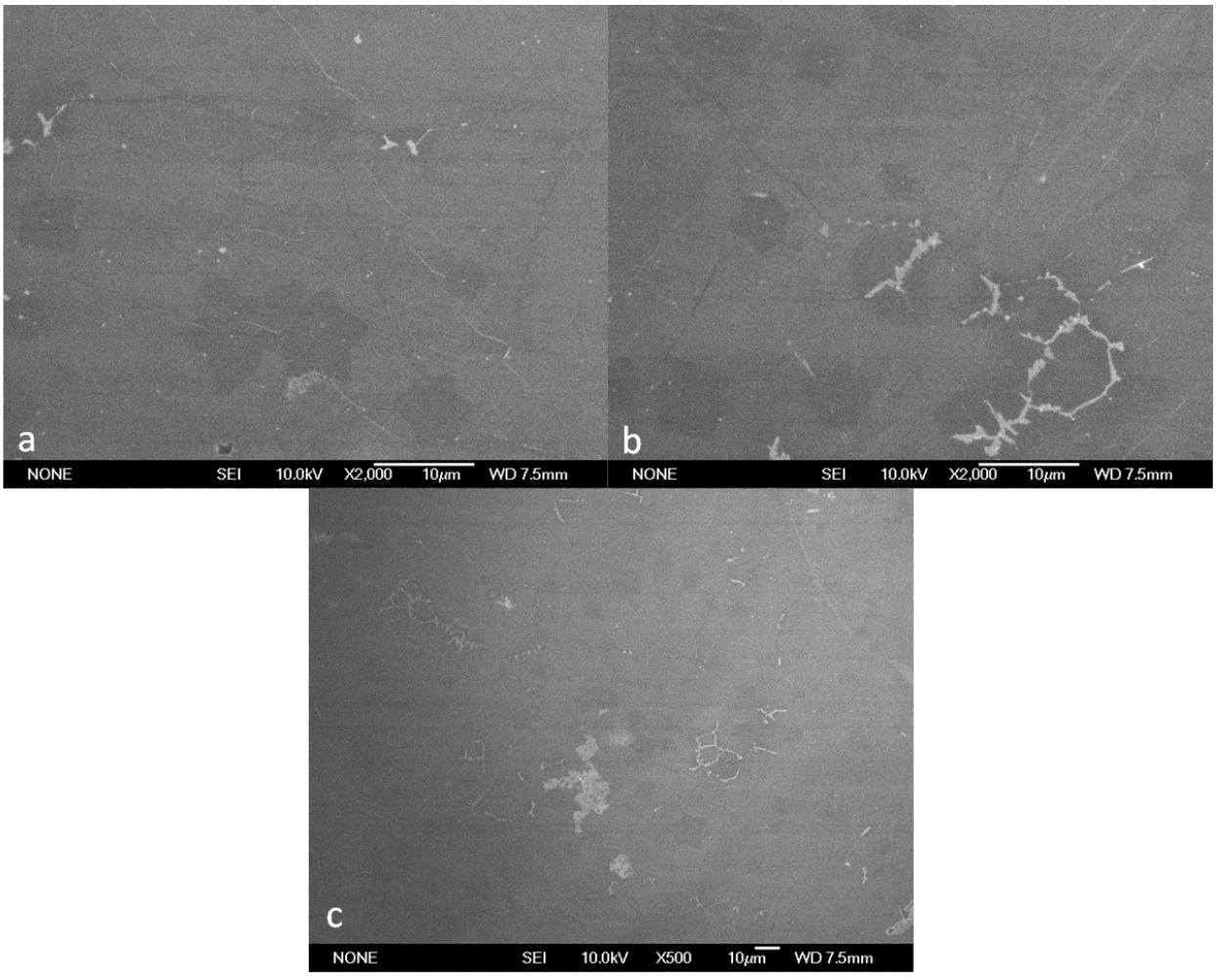

Figure 2.12 | The 5 minute growth of large, low density graphene grains on a copper substrate at atmospheric pressure: a. Avoiding the hydrogen anneal step in the synthesis of graphene leads to larger grain growth **b.** The copper surface is less densely populated by graphene grains even at 5 min growth time. **c.** The growth still follows a striated pattern due to the flow of the gases during growth.

Growth of graphene on nickel substrates:

Nickel is an interesting candidate for growth of graphene because 1) Ni yields the smallest lattice mismatch with the hexagonal carbons in graphene (1.2% mismatch for Ni(111); 2) low temperature growth of graphene may be obtained using Ni that is suitable for use with various engineered structures on substrates to make functional devices or composite structures; and 3) it allows for the tailored growth of multilayer graphene by altering the thickness of the Ni, cooling rate [27], or carbon feed during growth[32]. In order to make large, complete films of graphene suitable for use in water filtration membranes, we explored the growth of graphene on Ni. Figure 2.13 demonstrates the evolution of growth over time at high temperature (1073 °C).

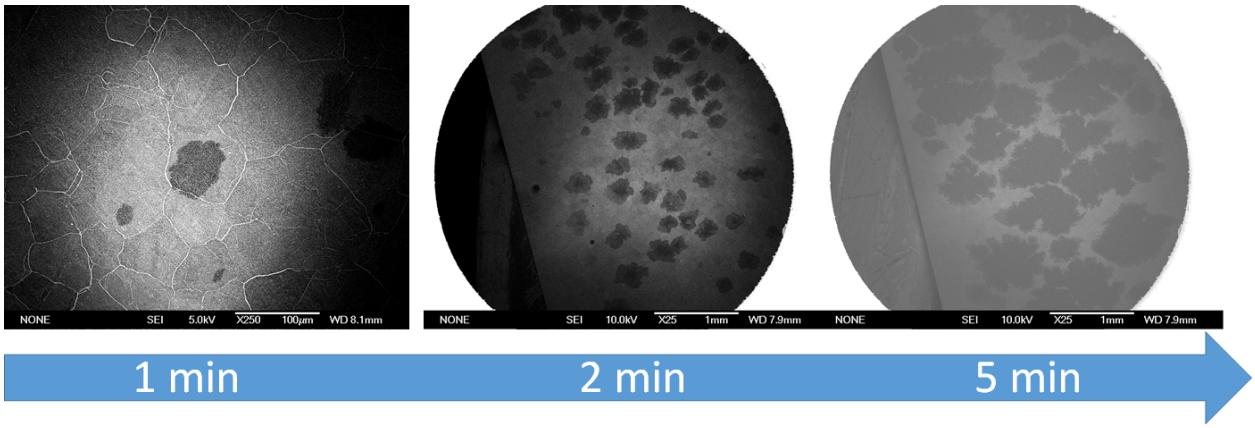

Figure 2.13 | Atmospheric growth of FLG as a function of time: At 1 min, nucleation begins and growth continues laterally well beyond 5 min. In order to obtain complete surface coverage at 2% methane concentration, a minimum of 20 minutes is required.

The growth conditions were kept the same as for copper (i.e. 25 μm thick foils, hydrogen-less anneal, low carbon flow rate, high hydrogen concentration during growth, atmospheric pressure). The growth of graphene on Ni is slightly more complicated than for copper. Two reactions are taking place both in the bulk and on the surface of the catalyst. Ni has better hydrogenation capabilities than copper and is therefore a more active catalyst. Methane flowing over the surface is dehydrogenated to form carbon radicals which can combine to form graphitic species on the surface. On the other hand, copper has very poor carbon solubility and therefore tends to form only single layers at reduced carbon concentrations because of surface limiting reactions. Unlike growth on copper, the maximum number of carbon atoms incorporated into the Ni is governed by the Ni-C phase[28-30] diagram and is temperature dependent. Most growths[27-33] are done far below the eutectic temperature of 1321 °C, usually around 1000 °C where the carbon solubility is nearly 0.2 wt%. Concurrently with the surface reaction, some of the carbon will diffuse into the bulk because of Ni's increased solubility for carbon. At low temperatures (<500 °C) this may lead to formation of a stable carbide, but at higher temperatures graphitic species are more stable. Growth of monolayer graphene has been observed at temperatures as low as 560 °C on Ni (111) surfaces[35]. Therefore, it is possible to tailor the amount of layers by reducing temperature. We explored growing graphene at various temperatures ranging from 600 °C to 1073 °C. Growing graphene below 760 °C only gave amorphous carbon films while growths above 1000 °C resulted in graphite. We obtained satisfactory growths at 780 °C as confirmed with UV-Vis, TEM, and Raman. The concentration of carbon is important to obtain full film coverage. We tried several experiments where we kept the flow rate of methane (4 sccm) and hydrogen (100 sccm) the same and varied the amount of Ar from 100 to 10000 sccm. We discovered that any

combination in which the total concentration of CH_4 decreases below 2% will not give continuous graphene growth.

Additionally, the cooling rate of Ni will affect the quality of films. Graphene segregation by cooling is a non-equilibrium process. Non-equilibrium segregation in general involves the transport of carbon vacancy-impurities that are trapped in grain boundaries and surfaces during cooling, and strongly depends on the cooling rate.[27] If the rate is too fast, then carbon diffusing from the bulk will be quenched and the graphene will not be able to uniformly precipitate out to the surface from grain boundaries. This results in patchy surface coverage and incomplete films. If too slow, then too much carbon is allowed to diffuse into the bulk rather than the surface, resulting in almost no film formation. Cooling somewhere in between and will give the desired film growth. For our system, we find that allowing the Ni to cool at 20 °C/min is sufficient to give complete films as seen in Figure 2.14a.

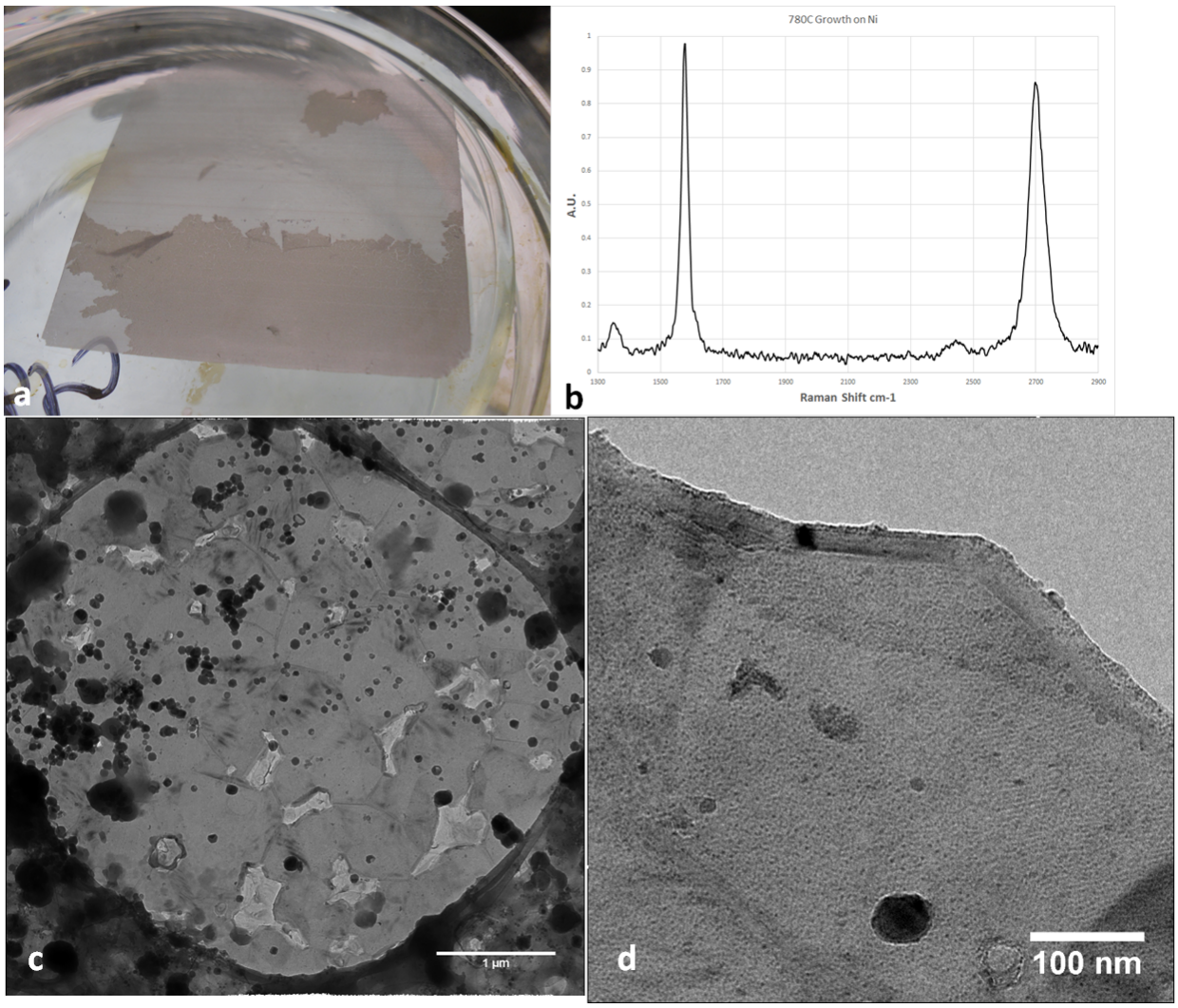

Figure 2.14 | Transfer of FLG from growth substrate: a. PMMA-less transfer. The resulting film was fished from the etchant and placed into a water bath. The brown layer underneath the top layer is the bottom layer of graphene that covered the Ni growth substrate in contact with the etchant. **b.** Raman of the transferred film. The characteristic G peaks appears at 1578 cm^{-1} and the 2D peak appears at 2702 cm^{-1}. **c.** Transferred film on a TEM grid. The appearance of multilayers is made apparent by the presence of micro tears. The black spots correspond to etchant residue. **d.** TEM image of FLG at an edge.

We wanted to know about the crystallinity of the as grown FLG films and whether or not they are ordered. For this we turned to SAED once again. Figure 2.15b shows a simulated pattern for the diffraction of AB stacked graphite. Next a series of SAED patterns were collected moving from left to right across this area (Figure 2.15c). The pattern changes and the (010) sets of

hexagonal spots (d = 0.214 nm) that's distinctive for AB stacked graphite is observed, especially in the later areas. However, the presence of diffusion around the spots indicates that they are mostly AB stacked, but the stacking order is not perfect (inset Figure 2.15c).

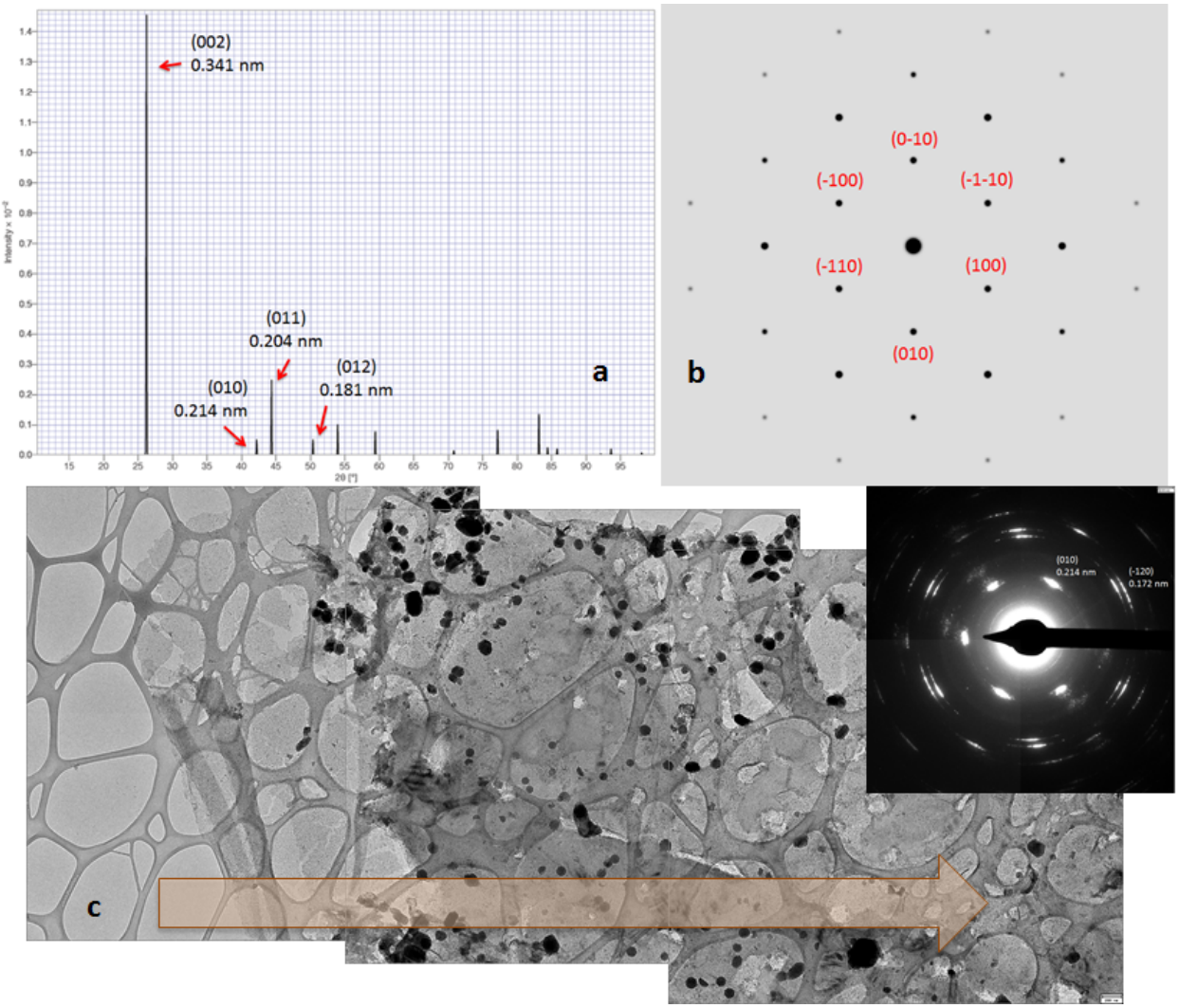

Figure 2.15 | Selected area electron diffraction (SAED) of as grown FLG: a. Simulated powder X-ray diffraction of AB-stacked graphite. **b.** Simulated SAED of AB-stacked graphite. **c.** The series of SAED patterns was collected moving from left to right across this area. Inset shows that the ordered stacking of FLG while crystalline, is not perfectly AB-stacked.

Alloying of catalytic metals offers another interesting opportunity to tailor the amount of graphene layers via CVD.[36-38] It is well known that copper and nickel alloy at temperatures

greater than 300 °C. The catalytic power of Ni combined with the self-limiting reactivity of Cu may lead to the formation of uniform FLG. We deposited a 400 nm thick layer of polycrystalline Ni onto a 25 μm thick copper foil. We wanted to ensure that the amount of Ni was as small as possible to prevent bulk diffusion and hinder multilayer growth. We used 4 sccm of CH_4, 100 sccm of H_2, and 200 sccm of Ar during the growth conditions. As previously done, we annealed the foil to 1073 °C under flowing Ar to increase grain growth. We next tested a variety of temperatures and growth times. We examined the growth at 780-1000 °C for 10-45 min on 2 inch by 2 inch foils. We discovered that we consistently obtained FLG of <10 layers at all temperatures investigated. However, for the 780 °C growths, incomplete films were obtained during transfer. We investigated the quality of the as prepared samples (Figure 2.16a-e). TEM reveals that the crystallinity of the samples is excellent.

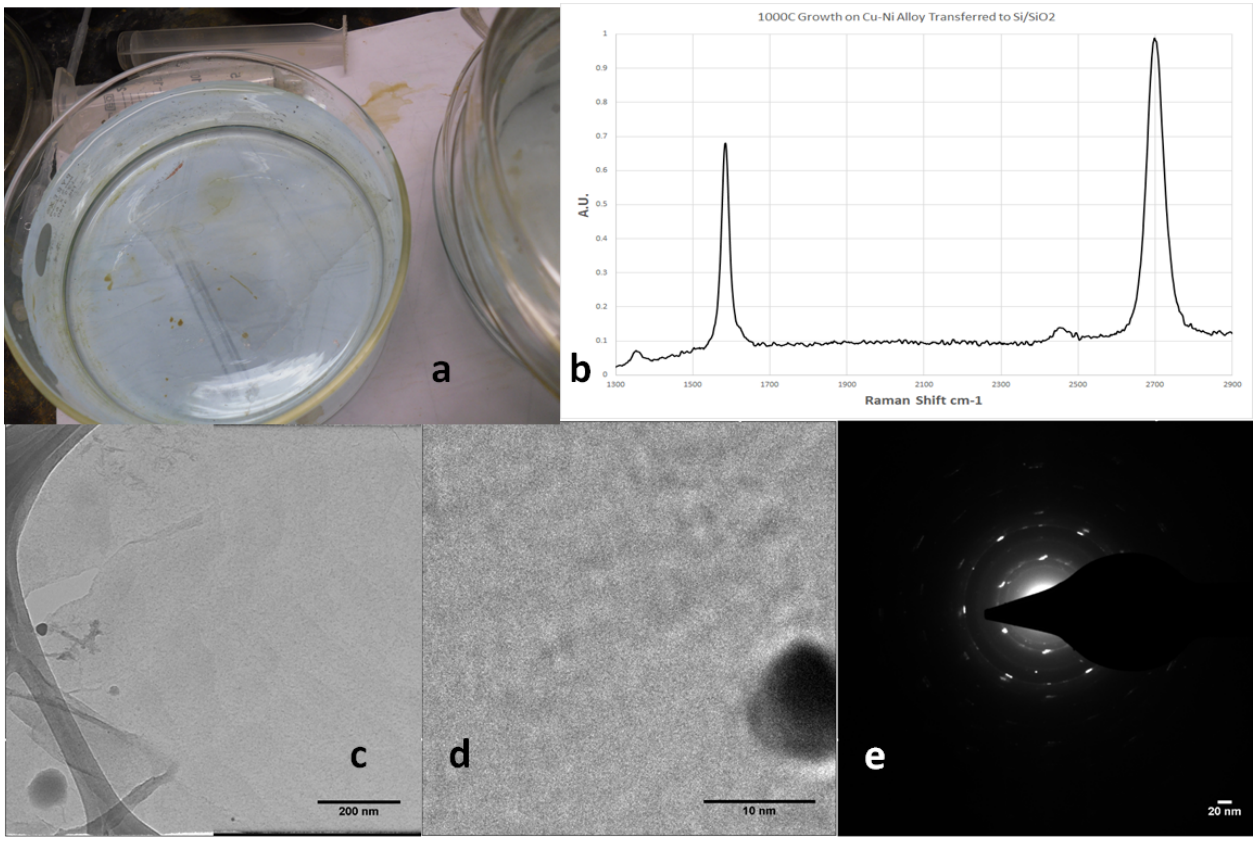

Figure 2.16 | Transfer of FLG from growth substrate: a. PMMA-less transfer in APS etchant. **b.** Raman of transferred film. The characteristic G peaks appears at 1585 cm^{-1} and the 2D peak appears at 2697 cm^{-1}. The ratio of I_{2D}/I_G is 1.45 indicating FLG. **c.** Transferred film on TEM grid. The black spots correspond to etchant residue. **d.** Magnified TEM image of FLG. **e.** SAED of FLG indicating crystallinity.

Comparison of the growths of FLG using either 25 μm Ni foils or Cu-Ni alloy was done with UV-Vis to elucidate the difference in layering (Figure 2.17). Keeping all other parameters consistent, the thickness of the Ni greatly influences the amount of layers formed. There are nearly 4 times as many layers with the thick foil compared to the alloyed film. The difference of course is the thickness of the sputtered Ni (400 nm vs. 25,000 nm) used for growth.

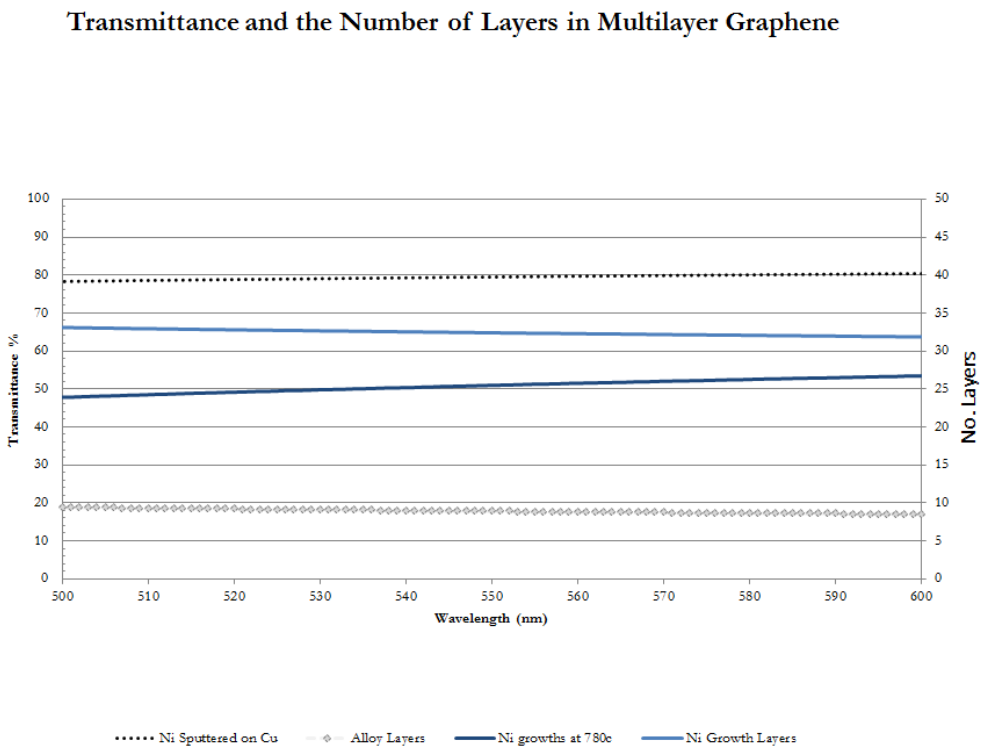

Figure 2.17 | Relationship between Transmittance and the number of layers in FLG: A plot of FLG grown on both 25 µm Ni foil and alloyed Cu-Ni. Transmittance is plotted to the left, while the number of layers is plotted on the right vertical axis. 550 nm wavelength is used to determine the transmittance of incident light in graphene. Each layer of graphene absorbs 2.3% of light thereby decreasing the transmittance of incident light. As expected, FLG grown on alloy (dotted gray diamonds) has more transmittance correlating to 9 layers of graphene.

Future directions:

We are utilizing the FLG for water filtration membranes. We are interested in the thick films because they may prove more mechanically robust for transfer and high pressure testing than single layer graphene. It would be interesting to explore the effect of decreasing the thickness of sputtered Ni systematically on the number of layers obtained from the alloy. Films of 50, 100, 200, 300 nm can be placed on top of commercially available copper foils. It would be equally interesting to do a growth time study to visualize the evolution of graphene domains on the alloy.

Due to the difference in catalytic ability, growth on the alloy may proceed radically differently than on Cu or Ni alone. Finally, varying the concentration of methane (down to ppm) during growth would enable us to grow large crystals of FLG. This may allow for millimeter sized growth of bilayer or few layer graphene that would be of interest for electronic devices.

References:

1 Li, Xuesong, et al. "Large-area synthesis of high-quality and uniform graphene films on copper foils." *Science* **324**.5932, 1312-1314, 10.1126/science.1171245 (2009)

2 Li, Xuesong, et al. "Graphene films with large domain size by a two-step chemical vapor deposition process." *Nano letters* **10**.11, 4328-4334, doi:10.1021/nl101629g (2010)

3 Reina, Alfonso, et al. "Large area, few-layer graphene films on arbitrary substrates by chemical vapor deposition." *Nano letters* **9**.1, 30-35, doi:10.1021/nl801827v (2008)

4 Bae, Sukang, et al. "Roll-to-roll production of 30-inch graphene films for transparent electrodes." *Nature nanotechnology* **5**.8, 574-578, doi:10.1038/nnano.2010.132 (2010)

5 Gao, Libo, et al. "Repeated growth and bubbling transfer of graphene with millimetre-size single-crystal grains using platinum." *Nature communications* **3**, 699, doi: 10.1038/ncomms1702 (2012)

8 Sun, Zhengzong, et al. "Growth of graphene from solid carbon sources." *Nature* **468**.7323, 549-552.9, doi: 10.1038/nature09579 (2010)

9 Lee, Seunghyun, Kyunghoon Lee, and Zhaohui Zhong. "Wafer scale homogeneous bilayer graphene films by chemical vapor deposition." *Nano letters* **10**.11, 4702- 4707, doi:10.1021/nl1029978 (2010)

10 Yan, Kai, et al. "Formation of bilayer bernal graphene: layer-by-layer epitaxy via chemical vapor deposition." *Nano letters* **11**.3, 1106-1110, doi: 10.1021/nl104000b (2011)

11 Luo, Zhiqiang, et al. "Pyridinic N doped graphene: synthesis, electronic structure, and electrocatalytic property." *Journal of Materials Chemistry* **21**.22, 8038-8044, doi:10.1039/C1JM10845J (2011)

12 Roddaro, S., et al. "The optical visibility of graphene: Interference colors of ultrathin graphite on SiO2." *Nano letters* **7**.9, 2707-2710, doi: 10.1021/nl071158l (2007)

13 Li, Qiongyu, et al. "Growth of adlayer graphene on Cu studied by carbon isotope labeling." *Nano letters* **13**.2, 486-490, doi: 10.1021/nl303879k (2013)

14 Lenski, Daniel R., and Michael S. Fuhrer. "Raman and optical characterization of multilayer turbostratic graphene grown via chemical vapor deposition." *Journal of Applied Physics* **110**.1, 013720, doi: (2011)

15 Gao, Libo, et al. "Efficient growth of high-quality graphene films on Cu foils by ambient pressure chemical vapor deposition." *Applied Physics Letters* **97**.18, 183109, doi: 10.1063/1.3512865 (2010)

16 Ferrari, A. C., et al. "Raman spectrum of graphene and graphene layers." *Physical review letters* **97**.18, 187401.17, doi: 10.1103/PhysRevLett.97.187401 (2006)

17 Malard, L. M., et al. "Probing the electronic structure of bilayer graphene by Raman scattering." *Physical Review B* **76**.20, 201401, doi: 10.1103/PhysRevB.76.201401 (2007)

18 Graf, Davy, et al. "Spatially resolved Raman spectroscopy of single-and few-layer graphene." *Nano letters* **7**.2, 238-242, doi: 10.1021/nl061702a (2007)

19 R. Wellman , A. Bottcher , M. Kappes , U. Kohl , H. Niehus , *Surf. Sci.* **542** , 81 – 93, (2003)

20 Y. R. Luo , in Handbook of Bond Dissociation Energies in Organic Compounds , *CRC Press* , Boca Raton, FL , 2009 , pp 65 – 80 .

21 Wang, Hong, et al. "Controllable synthesis of submillimeter single-crystal monolayer graphene domains on copper foils by suppressing nucleation." *Journal of the American Chemical Society* **134**.8, 3627-3630, doi: 10.1021/ja2105976 (2012)

22 Wu, Tianru, et al. "Triggering the Continuous Growth of Graphene Toward Millimeter-Sized Grains." *Advanced Functional Materials* **23**.2, 198-203, doi: 10.1002/adfm.201201577 (2013)

23 Robertson, Alex W., and Jamie H. Warner. "Hexagonal single crystal domains of few-layer graphene on copper foils." *Nano letters* **11**.3, 1182-1189, doi: 10.1021/nl104142k (2011)

24 Li, Xuesong, et al. "Large-area graphene single crystals grown by low-pressure chemical vapor deposition of methane on copper." *Journal of the American Chemical Society* **133**.9, 2816-2819, doi: 10.1021/ja109793s (2011)

25 Xing, Sirui, et al. "Kinetic study of graphene growth: Temperature perspective on growth rate and film thickness by chemical vapor deposition." *Chemical Physics Letters* **580**, 62-66, doi: 10.1016/j.cplett.2013.06.047 (2013)

26 Hao, Yufeng, et al. "The role of surface oxygen in the growth of large single-crystal graphene on copper." *Science* **342**.6159, 720-723, doi: 10.1126/science.1243879 (2013)

27 Yu, Qingkai, et al. "Graphene segregated on Ni surfaces and transferred to insulators." *Applied Physics Letters* **93**.11, 113103, doi: http://dx.doi.org/10.1063/1.2982585 (2008)

28 Park, Hye Jin, et al. "Growth and properties of few-layer graphene prepared by chemical vapor deposition." *Carbon* **48**.4, 1088-1094, doi:10.1016/j.carbon.2009.11.030 (2010)

29. Baraton, Laurent, et al. "Study of Graphene Growth Mechanism on Nickel Thin Films." *GraphITA 2011. Springer Berlin Heidelberg*, 1-7,doi: 10.1007/978-3-642-20644-3_1, (2012)

30 Kim, Seon Joon, Dae Woo Kim, and Hee-Tae Jung. "Key growth parameters affecting the domain structure of chemical vapor deposition (CVD)-grown graphene on nickel." *RSC Advances* **3**.45, 22909-22913, doi: 10.1039/c3ra44751k (2013)

31 Liu, Wei, et al. "Chemical vapor deposition of large area few layer graphene on Si catalyzed with nickel films." *Thin Solid Films* **518**.6 , S128-S132, doi:10.1016/j.tsf.2009.10.070 \ (2010)

32 Wang, Yanjie, et al. "Scalable synthesis of graphene on patterned Ni and transfer." *Electron Devices, IEEE Transactions on* **57**.12, 3472-3476, doi: 10.1109/TED.2010.2076337, (2010)

33 Pereira, Vitor M., et al. "Geometry, mechanics, and electronics of singular structures and wrinkles in graphene. *Phys. Rev. Lett*. **105**, 156603, doi:10.1103/PhysRevLett.105.156603 (2010)

34 Kwak, Jinsung, et al. "Near room-temperature synthesis of transfer-free graphene films." *Nature communications* **3**, 645, doi: 10.1038/ncomms1650 (2012)

35 Addou, Rafik, et al. "Monolayer graphene growth on Ni (111) by low temperature chemical vapor deposition." *Applied Physics Letters* **100**.2, 021601, doi: /10.1063/1.3675481 (2012)

36 Chen, Shanshan, et al. "Synthesis and characterization of large-area graphene and graphite films on commercial Cu–Ni alloy foils." *Nano letters* **11**.9, 3519-3525, doi:.10.1021/nl201699j (2011)

37 Liu, Xun, et al. "Segregation growth of graphene on Cu–Ni alloy for precise layer control." The *Journal of Physical Chemistry C* **115**.24 , 11976-11982, doi: 10.1021/jp202933u (2011)

38 Liu, Wei, et al. "Controllable and Rapid Synthesis of High-Quality and Large-Area Bernal Stacked Bilayer Graphene using Chemical Vapor Deposition." *Chemistry of Materials* **26**.2, 907-915, doi:/10.1021/cm4021854 (2013)

39 Woo, Yun Sung, et al. "Low temperature growth of complete monolayer graphene films on Ni-doped copper and gold catalysts by a self-limiting surface reaction." *Carbon* **64**, 315-323, doi:/10.1016/j.carbon.2013.07.081 (2013)

40 Vlassiouk, Ivan, et al. "Graphene Nucleation Density on Copper: Fundamental Role of Background Pressure." *The Journal of Physical Chemistry C* **117**.37, 18919-18926, doi:10.1021/jp4047648 (2013)

Chapter 3: Isolation and Transfer of CVD Graphene Films

High quality films of graphene are achieved using chemical vapor deposition (CVD) techniques where varying the pressure, temperature, growth substrate and concentration of carbon feedstock serve to optimize the intrinsic properties of graphene. Just as important as the growth of the films is the post-processing of graphene in order to isolate the films for a multitude of applications. The method chosen to isolate the as grown films of graphene can drastically affect the quality of films and significantly degrade the properties of graphene. Transfer of graphene must take into account the use of etchant, the contamination of films by polymer-assisted transfer, and the high temperature annealing of samples to remove contaminants. To make microelectronic or optoelectronic devices, a reliable method is required to transfer the graphene sheets from metallic Cu substrates to various substrates, including plastic, silicon or glass.

Traditional methods of CVD graphene transfer:

CVD films of graphene were first isolated by polymer assisted transfer in 2009.[3] Briefly, single layer graphene (SLGs) and few layer graphenes (FLGs) grown on Ni were isolated by depositing a polymethyl methacrylate (PMMA) sacrificial layer on top of the graphene/metal growth catalyst followed by subsequent etching of the underlying Ni by aqueous HCl solution (Figure 3.1). Not long after that, Cu was demonstrated to grow single layer graphene[2] and the most commonly used chemical solvents in the literature to etch the copper substrate have been ammonium persulfate ($(NH_4)_2S_2O_8$), ferric chloride ($FeCl_3$), and ferric nitrate ($Fe(NO_3)_3$). Aqueous $FeCl_3$ in particular is widely used because it can etch both Cu and Ni without producing hydrogen bubbles, which may damage graphene when acid etching is used.[7]

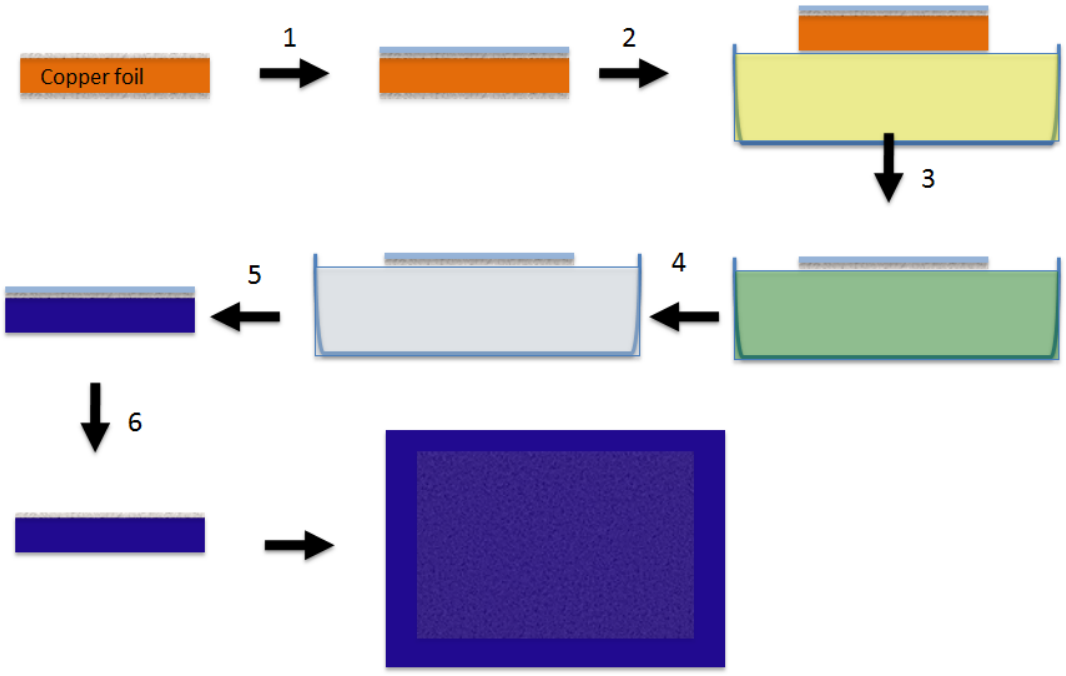

Figure 3.1 | Schematic of the polymer-assisted transfer (PAT) of graphene. 1. Spin-coat a polymer support layer onto CVD grown graphene/metal catalyst. 2. Place into etchant bath. 3. Etch away the underlying metal catalyst. 4. Fish out polymer/graphene film and rinse in DI water. 5. Fish out film onto substrate of choice for transfer. 6. Remove the polymer support layer with appropriate chemical solvent.

Polymer-assisted transfers (PATs) have utilized a variety of polymer supports beyond PMMA including polydimethylsiloxane (PDMS),[8,19] thermal released tape,[4] poly (bisphenol A carbonate) (PC)[9] or special self-release polymers.[10] Unlike PMMA, PDMS can be used as a stamp to attach directly to the graphene surface. Once the metal growth catalyst is chemically etched by $FeCl_3$, the graphene is left attached to the PDMS then transferred to SiO_2 by pressing and peeling the PDMS stamp. Roll-to-roll (R2R) transfer of graphene grown by CVD on Cu foils as large as 30 x 30 in^4 have been recently demonstrated. Again, this is a PAT process whereby graphene covered Cu foils are guided through a series of rolls and a thermal release tape (i.e. a tape adhesive at room temperature, but that peels off when heated) is attached as the polymer support while the Cu is removed by an etchant. The tape + graphene film can be attached to a (flexible) target

substrate (e.g. PET) and the supporting tape removed by heating. The graphene film is left attached onto the target substrate. Mechanical defects caused by a R2R transfer can be mitigated by use of a hot-pressing process[11]. Most recently, it has been demonstrated that the graphene/metal growth catalyst can act as an electrode for the splitting of water to form hydrogen and oxygen gas.[13,14] The bubbling created at the interface of the graphene/metal surface gently exfoliates the grown graphene film off the growth catalyst allowing for its reuse. While removing the need for an etchant, this process still requires the use of a sacrificial support layer for transfer. In all cases, PAT creates free-floating polymer–graphene films that can be fished out (and dried if necessary) and placed onto almost any substrate. Unfortunately, PAT wet transfers rarely give continuous large-area sheets and are not amenable to automated batch processing. Worse yet, interactions between the surface tension of the water and the underlying graphene film can cause wrinkles and tears that diminish its electronic properties.

Gao et al.[16] have shown an interesting way to isolate wafer scale graphene using a PAT process. The use of a nitrogen plasma treatment to clean the surface of the insulating Si/SiO_2 substrate before the deposition of the metal catalyst results in the generation of gas bubbles during the high-temperature growth of graphene (Figure 3.2). This 'bubble seeding' creates capillary bridges between the graphene and the substrate. The formation of narrow bubble channels between an insulating substrate and graphene produces long-range attractive forces, even in the presence of infiltrating water from the etching bath. While the water-based etchant acts to remove the catalyst, voids are created allowing water to infiltrate the substrate/graphene interface, but the strong attractive capillary forces arising from bubble formation keeps the graphene anchored onto the surface of the substrate. After wet etching of the metal layer, the

remaining water can simply be removed by baking the sample, the polymer support is removed by chemical solvent, and the graphene layer is deposited face-to-face on the insulating substrate without cracking or being damaged.

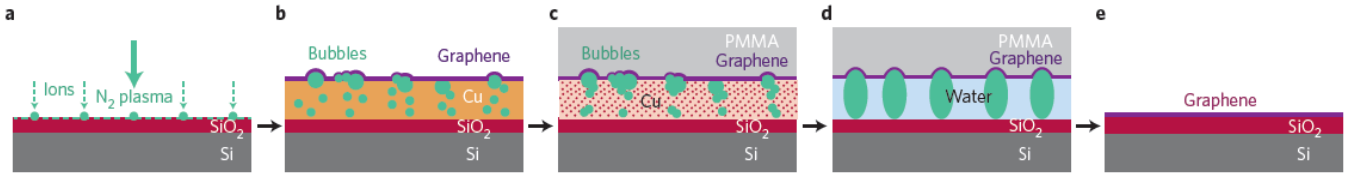

Figure 3.2 | Schematic of face-to-face transfer of CVD grown monolayer graphene: a. Nitrogen ion species are adsorbed onto the surface of a rigid substrate. **b.** During graphene growth, ions form bubbles that are trapped in the Cu catalyst layer by the graphene film. **c.** Water infiltrates into the graphene/SiO_2 interface during catalyst etching, forming capillary bridges. **d.** Bubble capillary bridges keep graphene anchored to the SiO_2 surface. **e.** After baking, the water is removed, the PMMA is stripped and the graphene is transferred on the substrate. (reprinted with permission[16] © Nature Publishing Group)

This is demonstrated by the excellent electronic properties of the transferred graphene films measuring up to eight inches in diameter: the researchers measured a uniform conductivity along the wafers reaching up to 4,000 S cm^{-1}, indicative of high crystallinity. Just as with all other PAT processes, once the support polymer is removed, the sample must be annealed under reducing atmosphere at high temperature (>300 °C)[19] in order to remove any polymer residues and maximize the intrinsic properties of the graphene. This precludes the use of flexible substrates that will not survive such high temperature post-processing.

The Use of Ammonium Persulfate Etchants

The wet transfer of CVD graphene via the use of polymer support and ferric chloride ($FeCl_3$) has been shown to severely weaken the grain boundaries in CVD graphene.[19]

Additionally, iron contaminants from ferric chloride and ferric nitrate have been shown to negatively affect the thermal and electronic properties of the graphene by doping the material.[16]

The decrease in mechanical, thermal and electronic properties may be due the catalytic etching of graphene by the presence of residual metal nanoparticles.[23,24] Various metal nanoparticles including iron from ferric chloride are known to create voids and defects in suspended graphene sheets.[21,22] This most likely occurs do to the insolubility of the by-products of etching with ferric chloride. The ferric ions in solution will partially combine with the hydroxide ions in water to form ferric hydroxide, a compound which is only slightly soluble and precipitates from solution as a brown solid. Ammonium peroxysulfate (APS) etching, on the other hand, produces only water soluble by-products such as copper sulfate and ammonium sulfates via the following reaction:

$$Cu(s) + S_2O_8^{-2} \longrightarrow CuSO_4(aq) + SO_4^{-2} \qquad [3.1]$$

The etching of copper with APS produces bubbling, possibly from the decomposition of the peroxysulfate to produce oxygen gas via the following reaction[27]:

$$S_2O_8^{-2} + H_2O \longrightarrow 2HSO_4^{-2} + 1/2O_2 \qquad [3.2]$$

The formation of these bubbles may lead to the ripping of the graphene films due to an increase in the pressure exceeding several MPa.[25]

Polymer-Free Transfer of Graphene:

As previously mentioned for the case of CVD-grown graphene, polymer-assisted transfer (PAT) of graphene from a metal growth substrate to arbitrary substrates is a common method utilized in

research and in preliminary plant scale fabrication. The choice of transfer polymer layer includes polymethyl methacrylate (PMMA), polydimethylsiloxane (PDMS), thermal released tape, poly (bisphenol A carbonate) (PC) or special self-release polymers as a temporary rigid support to prevent folding or tearing of the graphene film during the metal-etching step. PAT allows for the handling of the film once the rigid metal growth substrate is removed, but can cause unwanted doping and tearing once the support polymer is removed, typically by the use of some chemical solvent or temperature annealing step. Cleanliness is important if one wants to study or utilize the intrinsic properties of the graphene such as its electronic, thermal, or photonic capabilities. Temperature annealing steps are particularly problematic because they require the use of high temperatures (>300 °C) that eliminate the use of plastic substrates for transfer and device fabrication. We have found this to be the case when attempting to transfer very large graphene films (2 inch x 2 inch) onto polycarbonate or polysulfone water filtration membranes. First, the chemical compatibility between support substrate and the solvent used to strip off the support polymer (PMMA in our case) made clean, large area transfers unachievable. Second, complete removal of the transfer polymer via annealing could not occur on the membranes because they had been soaked in water, thus trying to bring them into a vacuum environment would prove disastrous. The high temperature may also cause deformation of the track etched pores in the membranes themselves, assuming the chemical solvent did not already cause pore collapse through the partial dissolution of the membrane material.

We decided to grow large area films on Cu, Ni, and Cu-Ni alloy foils and transfer them into diluted solutions of ferric chloride and APS etching solutions without the use of a polymer-assisted support layer.

Initially we tried using Ni grown samples because they are few layer graphene films (FLG) and since at the time we only had ferric chloride etchant available. Figure 3.3 demonstrates what occurs in the presence of ferric chloride diluted 1:6 parts by volume in DI water. Ferric chloride purchased from Transene typically corresponds to 30% $FeCl_3$, 4% HCl in water (w/w%). Diluting it to 1:6 of etchant to water is the equivalent of using a 5% solution of etchant. The etching of the underlying Ni leads to pits and tears within the sheet (Figure 3.3) and the water's surface tension pulls the sheet apart, especially when using high percentages of the etchant.[29]

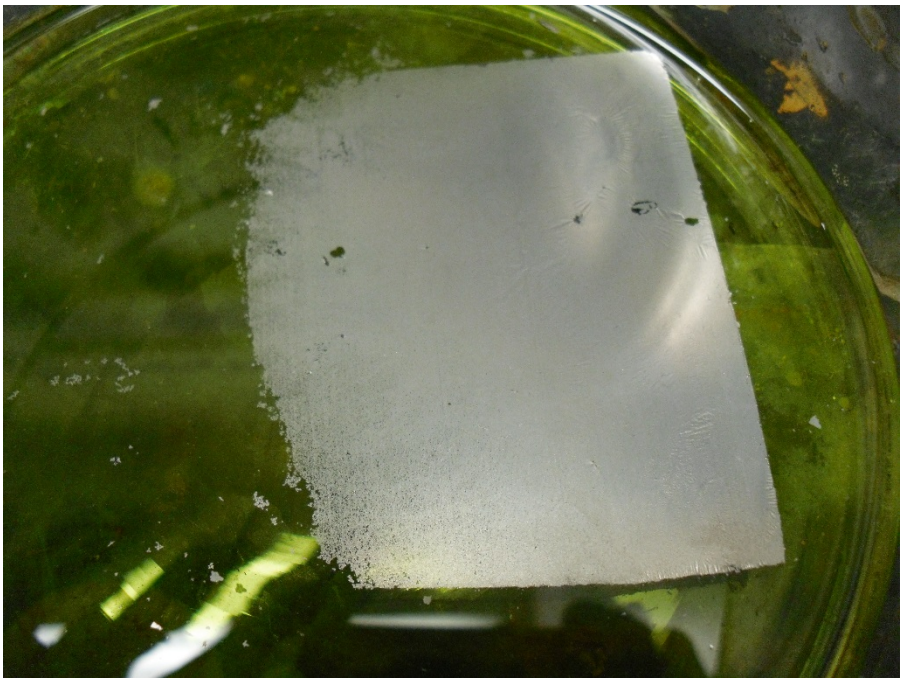

Figure 3.3 | Polymer-less transfer of few layer graphene in $FeCl_3$. The concentrated ferric chloride causes pits and tears on the graphene sheet.

We hypothesized that reducing the surface tension of the overall etching solution would lead to better and more continuous transfers of graphene. We decided to compare several transferred samples diluted 1:6 with ferric chloride and either water, ethanol, or isopropanol. The surface

tension of water, ethanol and IPA is 72, 22 and 21.7 dyn/cm at 20 °C, respectively. Table 3.1 summarizes our observed results.

Table 3.1 | Solvent Effects on the Quality of Transferred Graphene Films

Etchant	Solvent	Dilution	Notes
$FeCl_3$	None*	NA	Fast → Large holes
$FeCl_3$	Water	1:6	Smooth, Small holes
$FeCl_3$	Ethanol	1:6	Wrinkles, Fewer holes
$FeCl_3$	Isopropanol	1:6	Poor metal dissolution/suspension
$(NH_4)_2S_2O_8$	None*	NA	Little activity after 12 hrs

*Undiluted manufacturer's aqueous solution

Figure 3.4 depicts the effect of the solvent on the surface tension of the etchant. As the etchant decreases in surface tension, the graphene film no longer floats on the surface. Transferred films were more continuous as a result, but unwanted wrinkling began to occur. Wrinkling may lead to mechanical failure upon drying, although it may also lead to interesting wrinkled surfaces for use in sensing and capacitance.

Figure 3.4 | The effect of lowered surface tension in the water-based etchant on the transfer of graphene. Going from left to right, the surface tension of the solvent decreases.

Figure 3.5 shows optical microscope images of the as-transferred films onto Si/SiO_2 substrates. Use of ferric chloride in water without tailoring the surface tension leads to ripped and torn sheets. Much better transfers are achieved with decreasing surface tension, although this occurs at the expense of ferric chloride solubility and increased etching times.

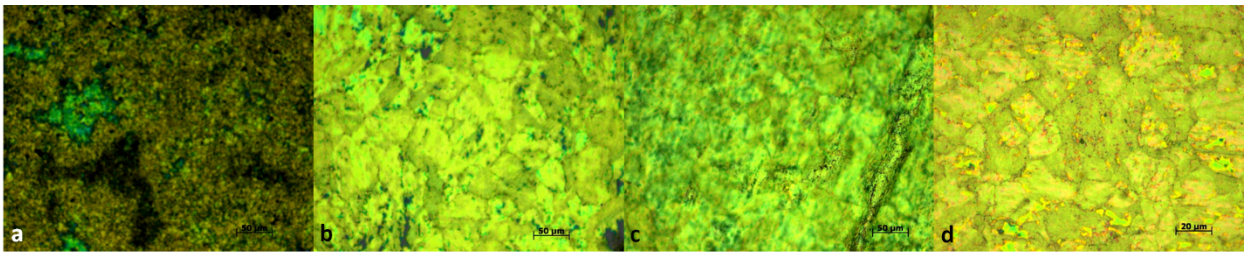

Figure 3.5 | Micrographs of transferred graphene films showing the effect of surface tension. a. Film transferred from concentrated $FeCl_3$. **b.** Film transferred from diluted etchant **c**. Film transferred from ethanol **d.** Film transferred from isopropanol.

We decided to dilute the etchant even further and add just a slight amount of ethanol to subsequent etchant baths. Adding 10% of ethanol to the etchant/water solution will decrease the surface tension from 72 to 48 dyn/cm at 20 °C.[30] The resulting samples had considerably less rips, tears, and wrinkles giving relatively large continuous sheets on PTFE (Figure 3.6c).

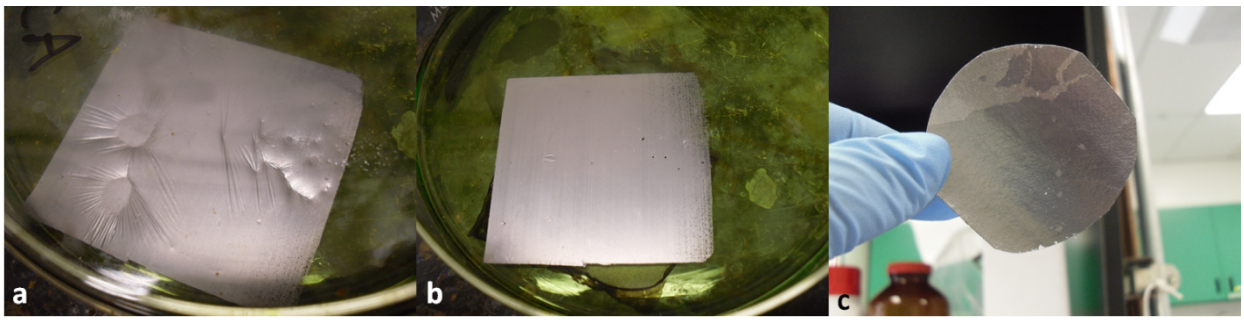

Figure 3.6 | Transfer of graphene films in diluted etchant with a small amount of ethanol added to decrease the surface tension. a. The graphene film in diluted etchant with 10% ethanol added. The wrinkling is caused by the etching of the underlying nickel. **b.** Film after all the nickel has been etched away. **c**. Transferred film onto PTFE with noticeably fewer rips and tears.

We also tried using dilute ferric chloride solutions to transfer graphene samples grown on a Cu-Ni alloy. We discovered (Figure 3.7) that the use of ferric chloride leads to torn sheets of graphene, most likely due to the presence of metal nanoparticles on the grain boundaries of the graphene sheet coupled with the surface tension of the water pulling the sheets apart. We switched the etchant to Transene APS-100 (Figure 3.7c) diluted to a ratio of 1:6 etchant to water. APS out of the bottle is 20% $(NH_4)_2S_2SO_8$ in water by weight. Initial etching proved visibly better than the ferric chloride, but the final transferred film (Figure 3.7d) suffered from rips and tears. We hypothesized decreasing the etch rate by dilution may lead to more continuous films so we diluted the APS down to a 1:20 ratio.

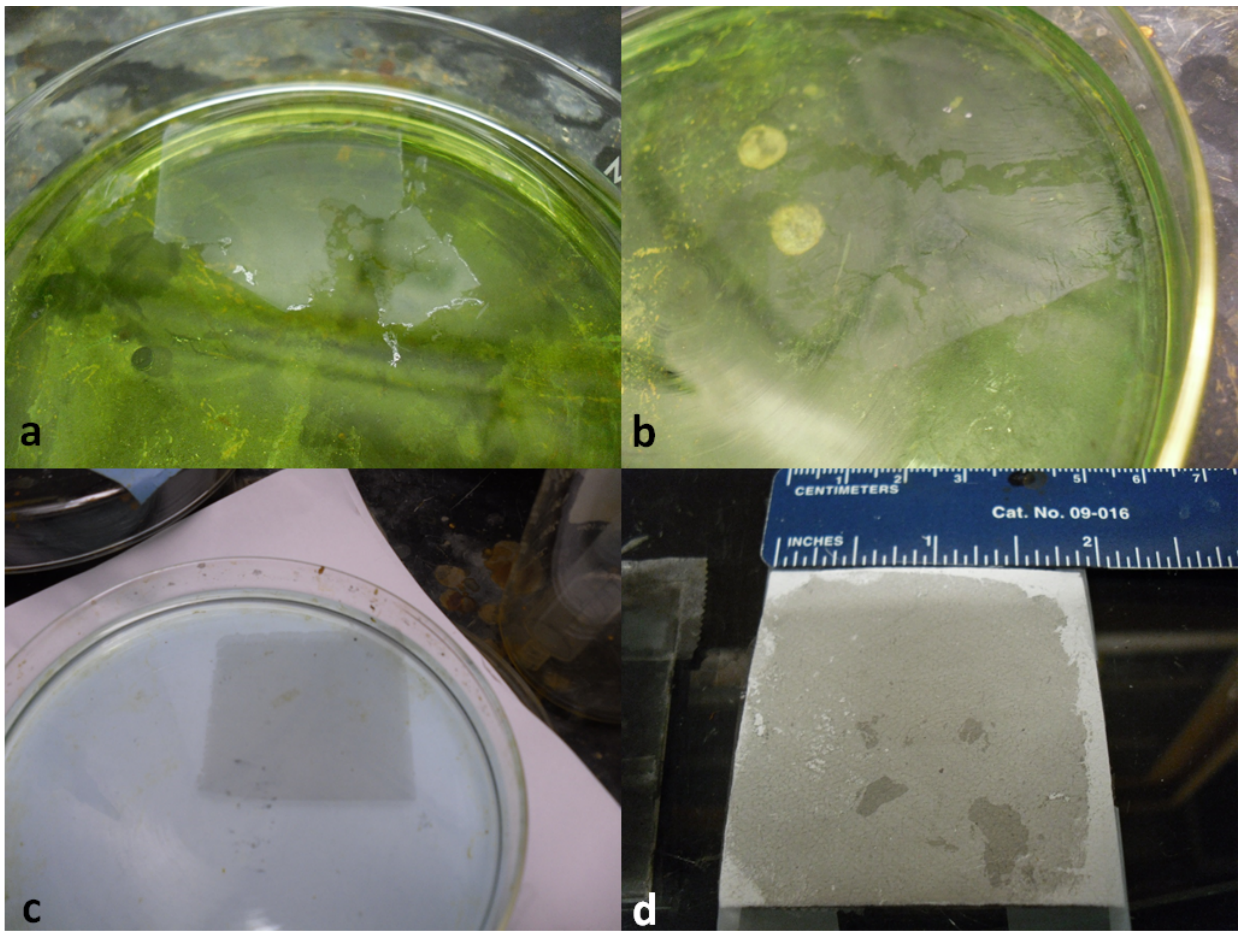

Figure 3.7 | Comparison of $FeCl_3$ vs. ammonium persulfate transfers of Cu-Ni alloy grown graphene films. a. Transfer in concentrated $FeCl_3$. **b.** Transfer in dilute $FeCl_3$. **c**. Transfer in APS. **d.** Film transferred onto PTFE membrane support.

The highly dilute APS gave the best quality transfers and most continuous sheets. We are currently exploring the use ethanol to decrease the surface tension of the APS etchant. Unlike ferric chloride, the reagents and products of the APS etching reaction are all highly soluble in water and ethanol mixtures.[31]

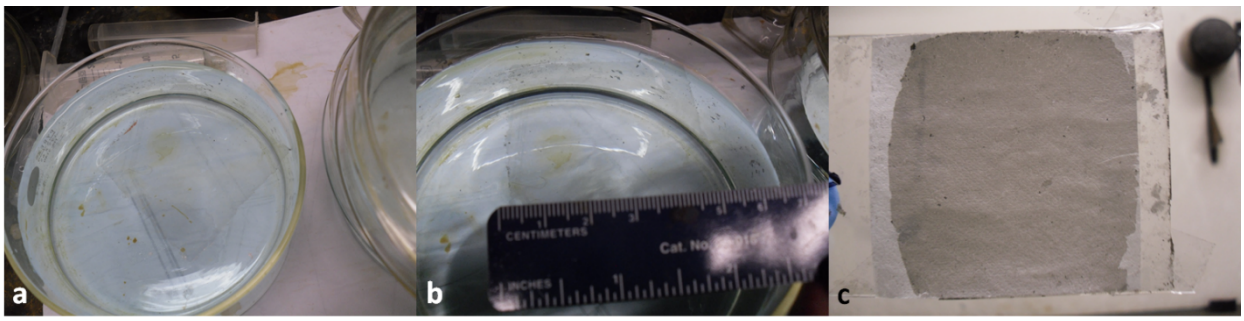

Figure 3.8 | Transfer of Cu-Ni alloy grown graphene film using diluted APS etchant. a. The film as it etches in dilute APS. Unlike Ni foil, the alloy readily etches in APS. **b.** Completely etched film. **c**. Transferred film onto PTFE support membrane. The transfer is much better with a slower etch rate.

Transferred films onto Si/SiO_2 were SEM imaged for quality and for Raman analysis. Films were also transferred onto lacy carbon TEM grids for selective area electron diffraction (SAED) (as previously shown in Chapter 2). Figure 3.9 a-b demonstrates the continuous nature of the polymer-less transferred films. The film covered half the TEM grid (Figure 3.9c-d) and the interface of the film and the bare grid are shown.

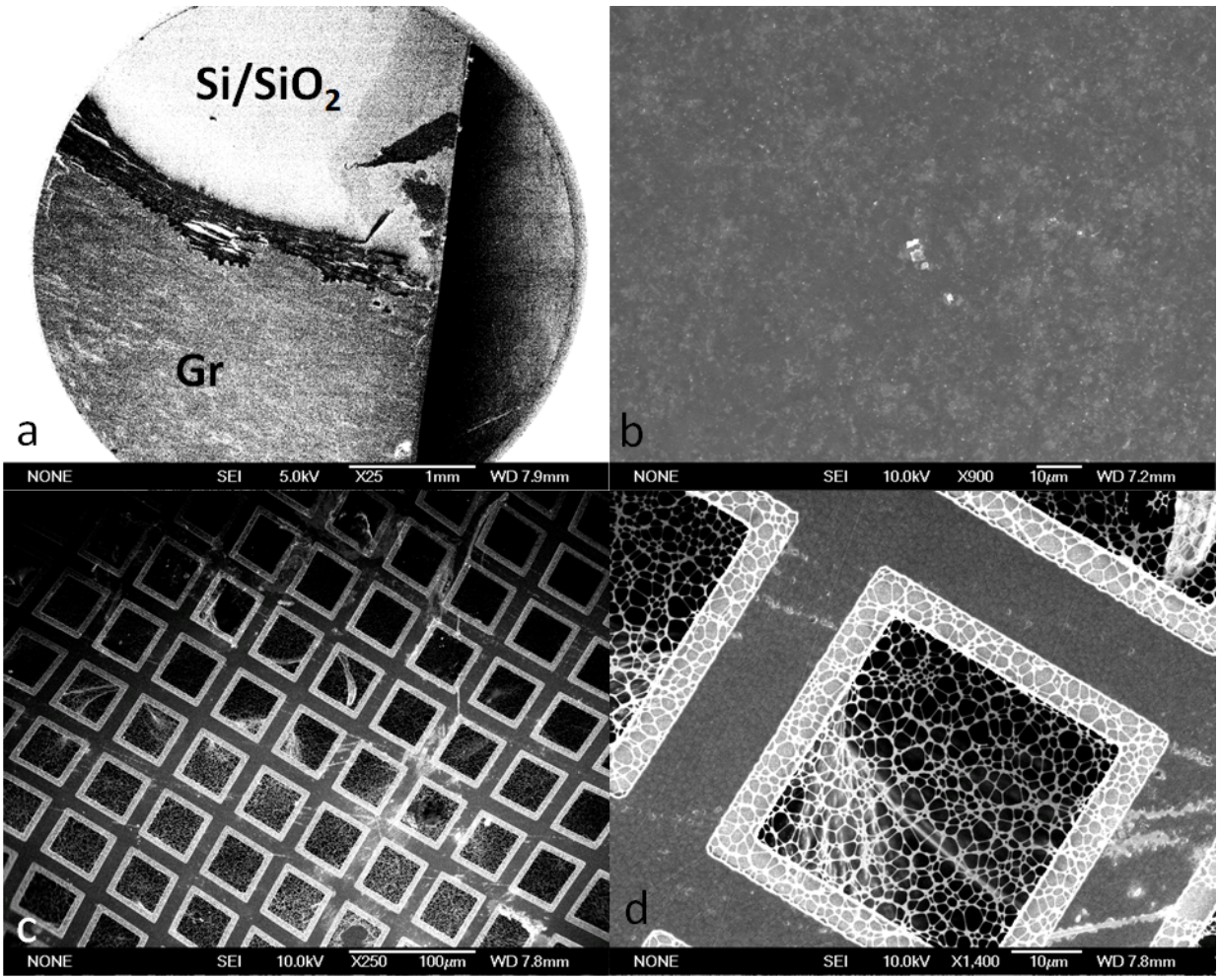

Figure 3.9 | Micrographs of transferred Cu-Ni alloy grown graphene. a. SEM of a graphene film on Si/SiO_2. **b.** SEM of the graphene film demonstrating its continuity. **c**. TEM grid half covered with alloy grown graphene. This image is taken at the interface of the graphene/bare TEM grid. **d.** Freestanding graphene film suspended over a TEM grid well.

Conclusions and Outlook:

We present a route to eliminate the polymer-residue contamination of large area sheets of continuous graphene suitable for use as membrane materials or transparent conducting films. There are many ways to transfer graphene and the method chosen will depend greatly on the final application and the compatibility of the substrate with post-processing techniques.

Electronic use of graphene films demands contamination free films. It would be best not to introduce polymer residue in the first place, but if the substrate of choice can withstand high temperature annealing, then there is no issue with using a transfer polymer as it will not significantly impact the final quality of the graphene. However, for use with flexible or porous substrates, issues such as chemical compatibility, the mechanical quality of graphene films, and temperature compatibility will exclude the use of transferred polymers. The good news is now there exists a choice.

References:

1 Berger, Claire, et al. "Ultrathin epitaxial graphite: 2D electron gas properties and a route toward graphene-based nanoelectronics." *The Journal of Physical Chemistry B* **108**.52, 19912-19916, doi: 10.1021/jp040650f (2004)

2 Li, Xuesong, et al. "Large-area synthesis of high-quality and uniform graphene films on copper foils." *Science* **324**.5932, 1312-1314, doi: 10.1126/science.1171245 (2009).

3 Reina, Alfonso, et al. "Large area, few-layer graphene films on arbitrary substrates by chemical vapor deposition." *Nano letters* **9**.1, 30-35, doi:10.1021/nl801827v (2008)

4 Bae, Sukang, et al. "Roll-to-roll production of 30-inch graphene films for transparent electrodes." *Nature nanotechnology* **5**.8, 574-578, doi: 10.1038/nnano.2010.132 (2010)

5 Li, Xuesong, et al. "Transfer of large-area graphene films for high-performance transparent conductive electrodes." *Nano letters* **9**.12, 4359-4363 doi: 10.1021/nl902623y (2009)

6 Suk, Ji Won, et al. "Transfer of CVD-grown monolayer graphene onto arbitrary substrates." *ACS nano* **5**.9, 6916-6924, doi: 10.1021/nn201207c (2011)

7 Reina, Alfonso, et al. "Transferring and identification of single-and few-layer graphene on arbitrary substrates." *The Journal of Physical Chemistry C* **112**.46, 17741-17744, doi: 10.1021/jp807380s (2008)

8 Kim, Keun Soo, et al. "Large-scale pattern growth of graphene films for stretchable transparent electrodes." *Nature* 457.7230, 706-710, doi: 10.1038/nature07719 (2009)

9 Lin, Yung-Chang, et al. "Clean transfer of graphene for isolation and suspension." *ACS nano* **5**.3, 2362-2368, doi: 10.1021/nn200105 (2011)

10 Song, Jie, et al. "A general method for transferring graphene onto soft surfaces." *Nature nanotechnology* **8**.5, 356-362, doi: 10.1038/nnano.2013.63 (2013)

11 Kang, Junmo, et al. "Efficient transfer of large-area graphene films onto rigid substrates by hot pressing." *ACS nano* **6**.6, 5360-5365, doi: 10.1021/nn301207d (2012)

12 Pirkle, A., et al. "The effect of chemical residues on the physical and electrical properties of chemical vapor deposited graphene transferred to SiO2." *Applied Physics Letters* **99**.12, 122108, doi: 10.1063/1.3643444 (2011)

13 Hong, Seul Ki, et al. "Carboxylic Group as the Origin of Electrical Performance Degradation during the Transfer Process of CVD Growth Graphene." *Journal of The Electrochemical Society* **159**.4, K107-K109, doi: 10.1149/2.101204jes (2012)

14 Gao, Libo, et al. "Repeated growth and bubbling transfer of graphene with millimetre-size single-crystal grains using platinum." *Nature communications* **3**, 699, doi: 10.1038/ncomms1702 (2012)

15 de la Rosa, César J. Lockhart, et al. "Frame assisted H_2O electrolysis induced H2 bubbling transfer of large area graphene grown by chemical vapor deposition on Cu." *Applied Physics Letters* **102**.2, 022101, doi: 10.1063/1.4775583 (2013)

16 Gao, Libo, et al. "Face-to-face transfer of wafer-scale graphene films." **Nature** 505, 190–194 doi: 10.1038/nature12763 (2013)

17 Huang, Pinshane Y., et al. "Grains and grain boundaries in single-layer graphene atomic patchwork quilts." *Nature* **469**.7330, 389-392, doi: 10.1038/nature09718 (2011)

18 Ruiz-Vargas, Carlos S., et al. "Softened elastic response and unzipping in chemical vapor deposition graphene membranes." *Nano letters* **11**.6, 2259-2263, doi: 10.1021/nl200429f (2011)

19 Lee, Gwan-Hyoung, et al. "High-strength chemical-vapor–deposited graphene and grain boundaries." *Science* **340**.6136, 1073-1076, doi: 10.1126/science.1235126 (2013)

20 Wu, Zhang Ting, et al. "The influence of chemical solvents on the properties of CVD graphene." *Journal of Raman Spectroscopy*, doi: 10.1002/jrs.4582 (2014)

21 Ramasse, Quentin M., et al. "Direct experimental evidence of metal-mediated etching of suspended graphene." *ACS nano* **6**.5, 4063-4071, doi: 10.1021/nn300452y (2012)

22 Zan, Recep, et al. "Interaction of metals with suspended graphene observed by transmission electron microscopy." *The Journal of Physical Chemistry Letters* **3**.7, 953-958, doi: 10.1021/jz201653g (2012)

23 Booth, Tim J., et al. "Discrete dynamics of nanoparticle channelling in suspended graphene." *Nano letters* **11**.7, 2689-2692, doi: 0.1021/nl200928k (2011)

24 Severin, N., et al. "Rapid trench channeling of graphenes with catalytic silver nanoparticles." *Nano letters* **9**.1, 457-461, doi: (2008)

25 Yang, Shangjiong, et al. "Characterization of nanobubbles on hydrophobic surfaces in water." *Langmuir* **23**.13, 7072-7077, doi: 10.1021/la070004i (2007)

26 Hallam, Toby, et al. "Strain, Bubbles, Dirt, and Folds: A Study of Graphene Polymer-Assisted Transfer." Advanced Materials Interfaces, doi: 10.1002/admi.201400115 (2014)

27 Kolthoff, I. M., and I. K. Miller. "The chemistry of persulfate. I. The kinetics and mechanism of the decomposition of the persulfate ion in aqueous medium." *Journal of the American Chemical Society* **73**.7, 3055-3059, doi: 10.1021/ja01151a024 (1951)

28 Regan, William, et al. "A direct transfer of layer-area graphene." *Applied Physics Letters* **96**.11 113102, doi: 10.1063/1.3337091 (2010)

29 Lin, Wei-Hsiang, et al. "A Direct and Polymer-Free Method for Transferring Graphene Grown by Chemical Vapor Deposition to Any Substrate." *ACS nano* **8**.2, 1784-1791, doi:10.1021/nn406170d (2014)

30 Vazquez, Gonzalo, Estrella Alvarez, and Jose M. Navaza. "Surface tension of alcohol + water from 20 to 50 ° C." *Journal of chemical and engineering data* **40**.3, 611-614, doi: 10.1021/je00019a016 (1995)

31 Urréjola, Santiago, Angel Sánchez, and Martín F. Hervello. "Solubilities of Sodium, Potassium, and Copper (II) Sulfates in Ethanol− Water Solutions." *Journal of Chemical & Engineering Data* **56**.5, 2687-2691, doi: 10.1021/je100979d (2011)

32 Dean, C. R., et al. "Boron nitride substrates for high-quality graphene electronics." *Nature nanotechnology* **5**.10, 722-726, doi:10.1038/nnano.2010.172 (2010)

Chapter 4: Graphene-assisted solution growth of vertically-oriented organic semiconducting single crystals

In addition to the excellent electronic, thermal, mechanical and optical properties of graphene, it should be noted that graphene also contains numerous π-conjugated bonds that can participate in organic reactions [46,47]. This property has very interesting consequences including formation of covalent bonds via Diels-Alder chemistry or surface-directed molecular assembly via strong π-interactions[48]. The latter property is especially attractive for conjugated materials including polymeric and small molecule conductors and semiconductors, which mostly consist of π-conjugated arenes. As a consequence, these molecules can interact with underlying surfaces containing π-π interactions such as graphene. Conjugated semiconductors have garnered a tremendous amount of attention in recent years largely due to their tunable properties and mechanical flexibility[4,8,9]. Solution-processable conjugated materials hold great promise in realizing next-generation electronic and optoelectronic devices because of their compatibility with low-cost processing methods such as spray-coating and roll-to-roll printing.[10,12] Solution processed single crystals of these materials possess the long-range order necessary to allow the intrinsic transport limits to be realized.[8]

Large area, high-density, high throughput device arrays are highly desirable, but alignment of these single crystals remains challenging.[5,13,14] Although alignment of single crystals that are oriented parallel with respect to the substrate have been developed for 1-D or 2-D devices[12,13,15] for applications that benefit from high surface area and directional transport in the vertical direction (e.g. solar cells and sensors), perpendicular (with respect to the substrate) alignment in

high density[1,2,4] is still challenging and sought after. Numerous "top-down" and "bottom-up" techniques have been developed to achieve such vertical orientation for inorganic materials and have led to breakthroughs in various fields including photovoltaic devices, vertical transistor arrays, energy-storage devices, self-powered generators, and intercellular interfacing.[1,16-19] However, approaches for creating such structures for organic materials are scarce and rely on the guidance of an external template.[5-7] These approaches are incompatible for vertical array alignment of organic semiconductors because they require harsh processing conditions for template removal that are detrimental to the delicate conjugated materials. Additionally, they expand the time and ultimately the cost of fabrication for these devices.

Development of a template-free method for producing vertically oriented single crystals for soluble conjugated materials would be disruptive. A novel "bottom-up" growth of vertically oriented single crystal arrays of various conjugated materials with a one-step, low cost, solution-based method by using a layer of graphene as the guiding substrate was developed. The crystal arrays possess excellent morphological and crystallographic orientation with the most efficient π-π stacking carrier transport direction perpendicular to the graphene substrate, which is desirable for the aforementioned applications.

The use of graphene wields excellent morphological and crystallographic orientational control of conducting polymers:

Tetraaniline (TANI) was chosen as a representative molecule for exploring graphene-assisted vertical crystallization since its monodispersity allows TANI to serve as a good model system for the crystallization of polyaniline, a benchmark conducting polymer.[20-22] In a typical crystallization, a loosely covered container is filled with a non-solvent for TANI, such as n-

hexane. A TANI solution is dropped onto a SiO_2/Si substrate coated with a layer of chemical vapor deposited (CVD) graphene[23] raised above the n-hexane liquid level (Figure 4.1a).

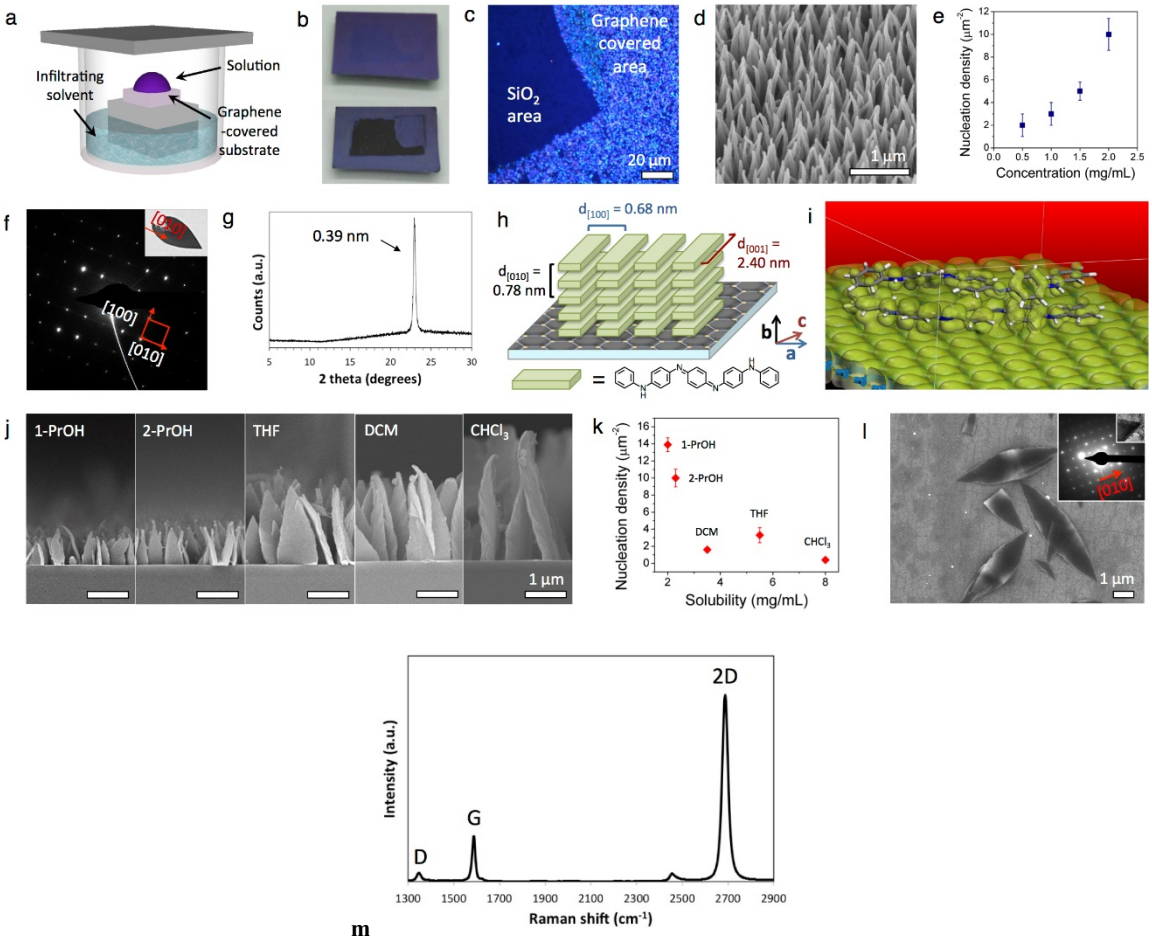

Figure 4.1 | Crystallization of tetraaniline on graphene. a. Vapor-infiltration setup used for the experiments. **b**. A graphene-coated SiO_2/Si wafer before (top panel) and after (bottom panel) the crystallization of tetraaniline. **c**. Polarized optical microscope image showing the SiO_2/graphene interface where crystals only grow on the graphene-covered areas. **d**. SEM image showing the plate-shaped tetraaniline crystals are oriented vertically on graphene. **e**, Control of crystal nucleation density by varying solution concentration. **f**. Top-view electron diffraction pattern of a vertical plate (shown in inset) transferred to a TEM grid. **g**. Powder XRD pattern of the crystal arrays. **h**. Proposed packing arrangement for the tetraaniline crystals obtained from SAED and XRD information. **i**. DFTB modeling illustrates the electron density overlap between two tetraaniline molecules and graphene leading to the preferred face-on orientation. **j**. Size control of the crystals achieved by using different solvents. **k**. Correlation between solubility and nucleation density of the crystals. **l**. Control over the orientation of tetraaniline crystals on graphene: horizontal crystals are obtained by using an aromatic infiltrating solvent. Inset shows the corresponding SAED pattern. **m**. Raman of the CVD graphene after transferring to the SiO_2/Si substrate.

The vapor of the non-solvent saturates the closed chamber and infiltrates into the TANI solution, creating supersaturation, which induces crystallization. At the end of the process, dark colored TANI can be observed on the graphene-covered area, while the SiO_2 area remains intact (Figure 2.1b). A cross-polarized optical micrograph further illustrates the high nucleation affinity of tetraaniline on graphene as evidenced by a sharp interface between the graphene and SiO_2 surfaces with the strongly birefringent tetraaniline crystals only observed on graphene (Figure 4.1c). SEM analysis reveals these crystals are oriented vertically with respect to graphene and exhibit uniform morphological orientation and height (Figure 4.1d). The nucleation density of these crystals can be readily controlled by varying the solution concentration (Figure 4.1e). For instance, 2-propanol solutions of TANI with concentrations of 0.5, 1.0, 1.5, and 2.0 mg/mL lead to nucleation densities of 2, 3, 5, 10 crystals per square micrometer, while the crystal height and size remain constant (Figure 4.1e).

Selected area electron diffraction (SAED) analysis by TEM allowed us to decipher the crystallographic orientation of the resulting crystals. Several crystals were transferred to TEM grids for inspection and the electron diffraction pattern of a plate laying flat on a TEM grid (Figure 2.1f) shows sharp Bragg spots, indicating these plates are single crystals. A (020) d-spacing of 0.39 nm is obtained, suggesting that the tetraaniline molecules π-stack parallel to the graphene substrate along the long-axis of the crystals.

When a large-area crystal array (~1 cm^2) was analyzed by powder XRD, only one intense peak at 23.8° 2θ was observed (Figure 4.1f). It corresponds to a d-spacing of 0.39 nm, agreeing with the (020) spacing obtained from SAED, which indicates that all molecules are uniformly π-stacked along the vertical direction in each crystal over a large area. As demonstrated by the diffraction results, our graphene-assisted approach exerts both excellent morphological and crystallographic

orientational control. Contrast this to conventional template-guided methods which provide alignment for the supramolecular morphology, yet offer little control over the molecular packing direction.[5-7] The uniform orientation in solid-state packing allows for stable and consistent device performance at the macroscopic scale for anisotropic materials such as organic semiconductor crystals in important applications such as solar cells and sensors.[1,2,4]

We performed experimental and theoretical investigations into (1) the surface requirements, (2) the energetics in binding affinity, and (3) the influence of the solvent system in order probe the mechanism behind the graphene-assisted crystallization.

Fully sp2 conjugated carbon lattices offer the most energetically stable surfaces for vertical alignment:

We transferred mechanically exfoliated graphene,[24] chemically converted graphene (CCG),[25] and laser scribed graphene (LSG)[26] onto SiO_2/Si substrates for tetraaniline crystallization, to compare with CVD-grown graphene[23] (Figure 4.2). Among these, oriented vertical crystal arrays grow selectively on the mechanically exfoliated graphene flakes, in a fashion identical to that on CVD graphene. On the other hand, clusters of crystals form when CCG or LSG serve as the substrate, similar to crystallization on conventional surfaces such as SiO_2. The crystallization does not show any selectivity in nucleation sites when either CCG or LSG and SiO_2 surfaces are present.

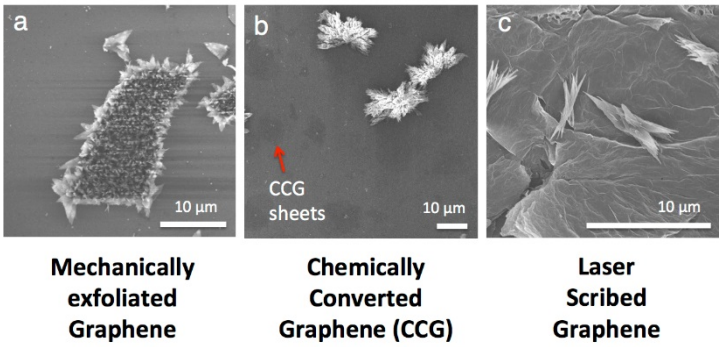

Figure 4.2 | Crystallization of tetraaniline on graphene and graphene-like surfaces. SEM images showing crystals formed on **a.** mechanically exfoliated graphene, **b.** chemically converted graphene, and **c.** laser scribed graphene.

It has been well established that CVD-grown and peeled graphene both possess a fully sp^2 conjugated carbon lattice,[23,24,27] whereas a small amount of oxygenated groups remain on the basal plane of the graphene sheets reduced from graphene oxide either chemically (CCG) or photothermally (LSG).[25,26] Therefore, an atomically homogeneous and defect-free sp^2 hybridized surface is necessary for achieving vertical crystallization of conjugated compounds such as tetraaniline as it provides preferred orbital, electronic density and dipole overlap at the interface between the substrate and the molecules, which has been demonstrated to be critical factors for controlling the orientation of organic molecules adsorbed on a substrate.[28,29] In fact, tight-binding density functional theory (DFTB) calculations indicate that TANI adsorbs on graphene favorably in a face-on orientation. This configuration provides the strongest overlap of electron densities between the two, while minimizing the repulsive interactions (Figure 4.1i). The binding energy is calculated to be 68 kcal/mol, which indicates an off-centered overlap of the π-electrons of graphene and tetraaniline. Since the preferred orientation between tetraaniline and graphene is face-on, and crystals of conjugated molecules tend to grow along their π-π stacking direction, tetraaniline crystals grow vertically from the graphene-coated substrate with the π-π stacking direction perpendicular to graphene.

Solvation effects aid in directing the orientation of tetraaniline crystal growth on graphene:

In addition to the surface and energetic factors, both the solvation and infiltrating solvents play important roles in dictating the preferred nucleation and controlling the orientation of tetraaniline crystal growth on graphene. Tetraaniline is soluble in a variety of polar solvents. Various solutions were cast onto graphene coated SiO_2/Si substrates for tetraaniline crystallization. We observed that when the solvent has a dielectric constant that is the same or lower than that of 1-propanol, arrays of vertical crystals form selectively on the graphene-coated area. Such solvents include 1-propanol, 2-propanol, dichloromethane, tetrahydrofuran, and chloroform.[30] On the other hand, when the solvation solvent's dielectric constant is higher than that of 1-propanol, e.g. acetone, ethanol, methanol, acetonitrile, and dimethyl sulfoxide, [30] randomly oriented clusters of crystals form all over the substrate, without selectivity for the graphene-coated area. Since graphene is a non-polar surface,[31] it is important to use a solvent with a lower dielectric constant so that the solution thoroughly wets the graphene-covered area while supersaturation is reached, so that preferred nucleation of tetraaniline can occur directly on the graphene. Conversely, more polar solvents, e.g. ethanol, acetonitrile, etc., do not favor the non-polar graphene surface. In fact, it can often be observed that as the solvent evaporates, the remaining droplet tends to migrate away from graphene to the SiO_2 area, leading to large clusters of crystals forming on the SiO_2 substrate, while the deposition density on graphene remains low.

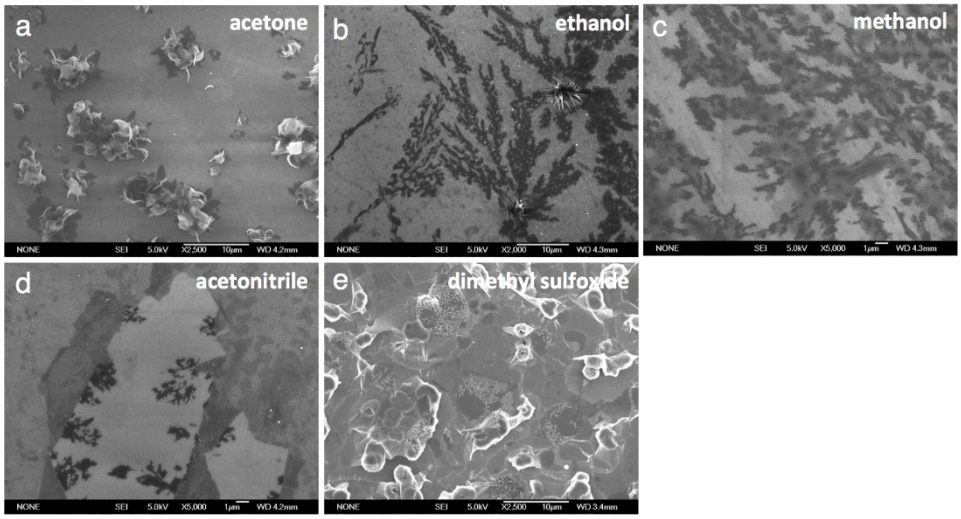

Figure 4.3 | The effect of various solvents on the crystallization of tetraaniline on graphene. SEM images of tetraaniline assemblies formed on graphene by using **a.**acetone, **b.** ethanol, **c.** methanol, **d.** acetonitrile, and **e.** dimethyl sulfoxide as the solvation solvent.

The solvation solvent also offers control over the nucleation density and crystal size of the vertical crystal arrays. As shown in Figure 4.1j, crystals of different sizes can be obtained by using different solvents at the same concentration (e.g. 2 mg/mL), with larger crystals corresponding to lower nucleation density, and smaller ones to higher nucleation density. Plotting the solubility of TANI in these solvents against their nucleation density reveals a nearly inversely proportional relationship (Figure 4.1k). Since the TANI concentration is close to saturation in solvents such as 1-propanol or 2-propanol, supersaturation is quickly reached as soon as n-hexane starts to infiltrate, resulting in rapid nucleation that leads to a larger number of smaller crystals. Conversely, a longer non-solvent infiltration period is needed to induce supersaturation for solvent systems in which TANI is more soluble (i.e. DCM, THF, chloroform). Therefore, a slower nucleation process is created, which leads to larger crystals with lower nucleation densities.[32]

The ability to tailor crystal orientations on a certain substrate is necessary and desirable for expanding the realm of device applications. Here, we demonstrate that the orientation of the tetraaniline crystals on graphene can be controlled by the choice of infiltrating solvents. We observe that when a solvent with suitable solvation properties is used, all of the tested hydrocarbon infiltrating solvents lead to vertical crystal growth (Figure 4.4).

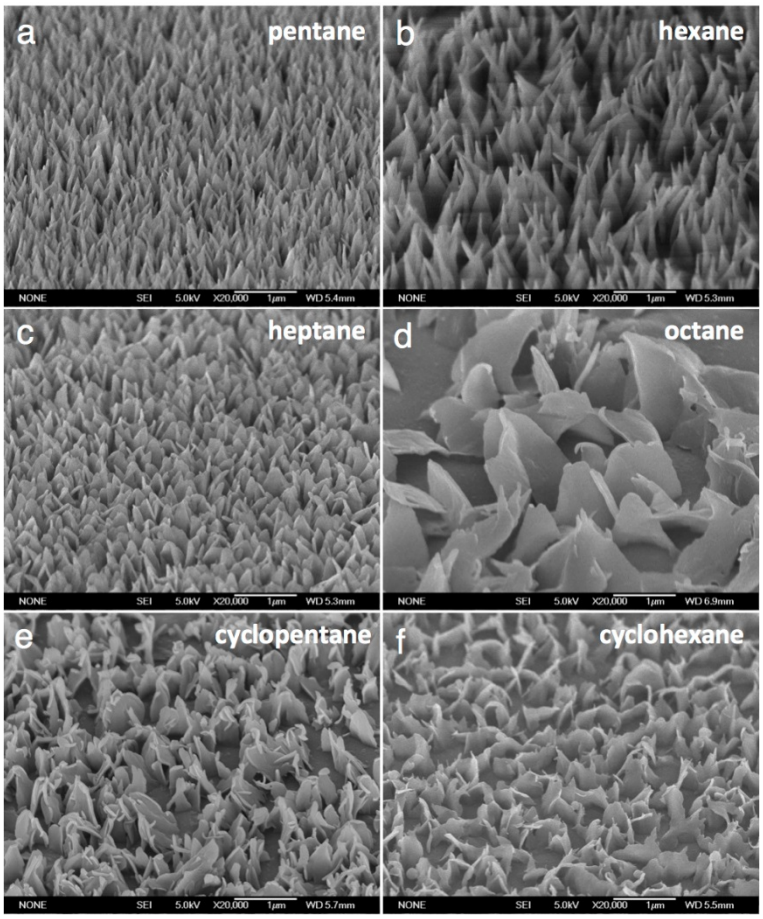

Figure 4.4 | Crystallization of tetraaniline on graphene using various solvents. Tilted SEM images of tetraaniline crystallized on graphene using **a.** n-pentane, **b.** n-hexane, **c.** n-heptane, **d.** n-octane, **e.** cyclopentane and **f.** cyclohexane as the infiltrating solvent. All these hydrocarbon solvents lead to vertically oriented crystal arrays.

On the other hand, when an aromatic solvent (e.g. benzene or toluene) is chosen as the infiltrating solvent, tetraaniline crystals grow in a horizontal orientation, i.e. parallel to the graphene substrate (see Figures 4.5 and 4.1l). SAED patterns of such crystals show their π-π stacking direction is also along their long-axis, which is now parallel with respect to graphene (inset to Figure 4.1l).

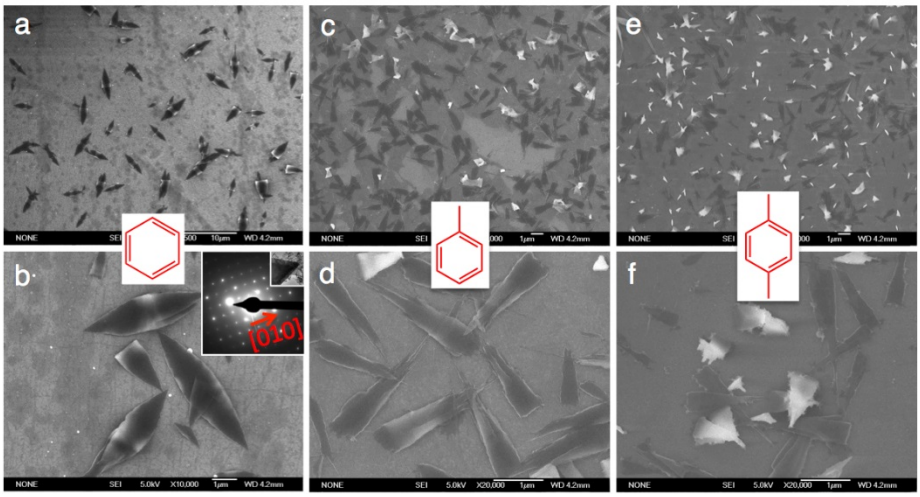

Figure 4.5| **Crystallization of tetraaniline on graphene using aromatic solvents**. SEM images illustrating that when an aromatic solvent such as (**a-b**) benzene, (**c-d**) toluene, or (**e-f**) xylene is used as the infiltrating solvent, the crystals lie horizontal with respect to the graphene substrate. Inset in (b) is an electron diffraction pattern of a horizontal crystal, which shows an identical diffraction pattern as those grown vertically on graphene when a non-aromatic hydrocarbon infiltrating solvent was used.

The vertical growth of the conjugated tetraaniline crystals is largely a result of the strong affinity for the molecules to bind in a face-on configuration with respect to graphene due to the strong electron density overlap (Figure 4.1i). However, aromatic molecules such as benzene also have a high binding affinity for graphene. DFTB calculations show that benzene adsorbs strongly on the graphene surface with an energy of ~17 kcal/mol per benzene molecule. The nucleation sites available for tetraaniline depend on the surface coverage level. At half or even a quarter of a monolayer coverage of a graphene surface by benzene, the probability of tetraaniline adsorbing

in a face-on configuration is severely reduced. Although tetraaniline is adsorbed at 68 kcal/mol per molecule according to DFTB calculations, the kinetics of face-on adsorption become unfavorable due to the high solvent-to-tetraaniline ratio. Thus, tetraaniline molecules stack more favorably in an edge-on fashion, which in turn alters the crystal growth direction and leads to the horizontal orientation (Figure 4.6).

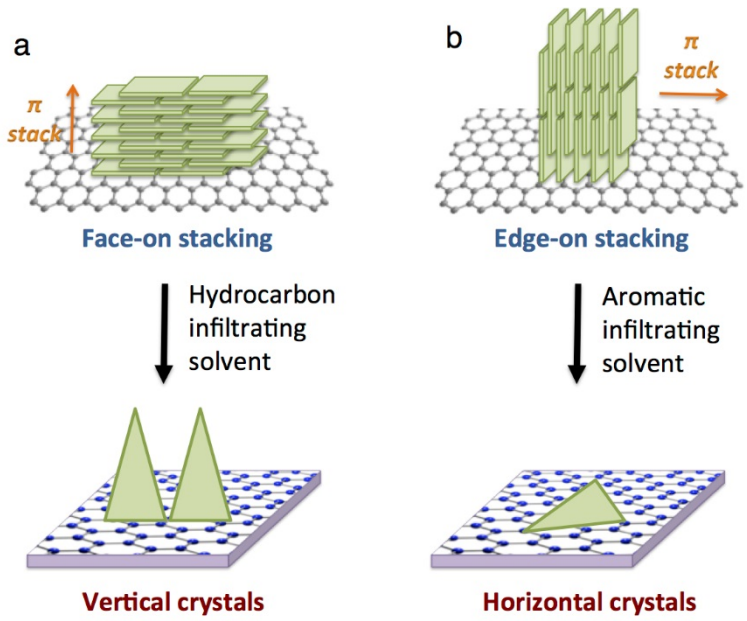

Figure 4.6 | Schematic of the crystallization of tetraaniline on graphene when using two classes of solvents. The stacking arrangement in relation to the nature of the infiltrating solvent influences the final crystal orientation.

The ability to readily control tetraaniline crystal orientation on graphene offers the opportunity to study its anisotropic electrical transport properties along different crystallographic axes using conductive atomic force microscope (cAFM). The transport properties along the interfacial stacking direction (i.e. the b-axis) can be obtained by placing the AFM tip as the top electrode on a vertical crystal, while using the graphene substrate as the bottom electrode (Figure 4.7a). On the other hand, when the same electrode configuration is applied to crystals grown horizontally

on graphene, the transport properties along the oligomer backbone (i.e. the c-axis) can be studied (Figure 4.7c). Figure 2.7b and d show AFM images of vertical and horizontal crystals on graphene, respectively.

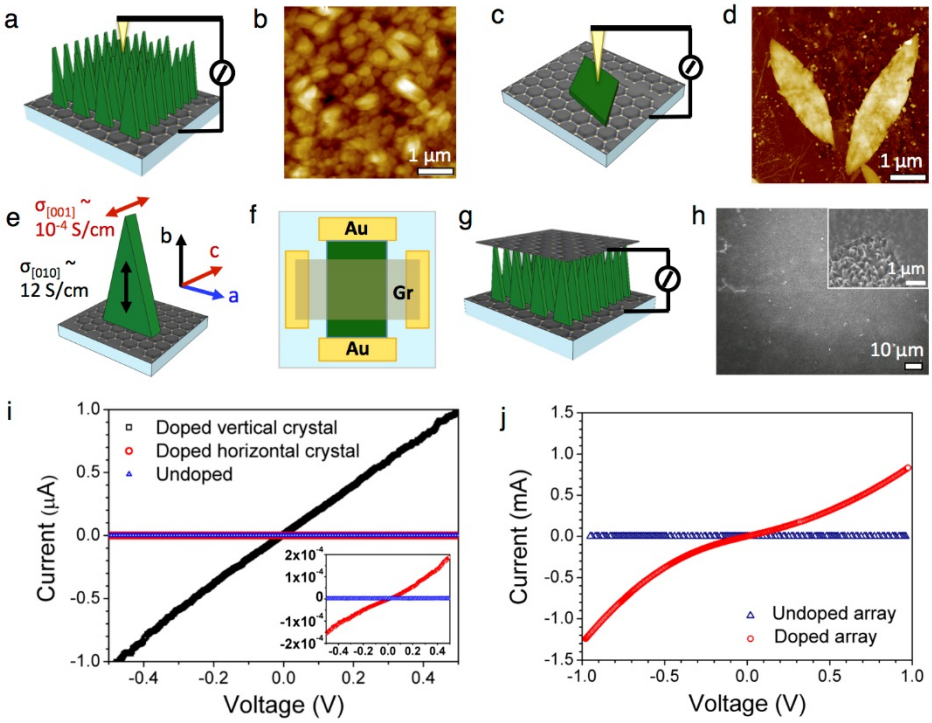

Figure 4.7 | Anisotropic electrical properties of the tetraaniline crystals grown on graphene. a. Schematic of the conductive-AFM measurement setup for the vertical crystals probing current along the b-axis. **b.** Topographic AFM image of a high density array of the tetraaniline vertical crystals. **c.** Schematic of the conductive-AFM measurement setup for the horizontal crystals where the transport along the c-axis can be obtained. **d.** Topographic AFM image of a crystal laying horizontally on graphene. **e.** Different conductivity values along the different crystallographic axes. **f. and g.** Schematics showing the top view (f) and the cross-sectional view (g) of the graphene/tetraaniline array/graphene (Gr/TANI/Gr) sandwich device. **h.** SEM image showing the top graphene electrode laminated on top of the vertical crystals. Inset illustrates a more magnified view at an edge of the top graphene layer. **i.** Typical I-V curves obtained for undoped crystals, a single vertical plate and a single horizontal plate after vapor doping. Inset has a smaller current scale showing the lower current for the horizontal plates. **j.** I-V plots of the Gr/TANI/Gr sandwiched devices.

Current-voltage (I-V) curves collected via cAFM are shown in Figure 4.7i. An insulating baseline was obtained for the as-grown undoped crystals regardless of the orientation (blue

triangles). Once doped with an acid (e.g. HCl vapor), the current increases by over six orders of magnitude (black squares) for the vertically oriented crystals, revealing a conductivity of ~12.3 S/cm. The conductivity is one order of magnitude greater than the highest previously reported value for tetraaniline,[21] and this could be largely attributed to (1) the high molecular symmetry of the phenyl/phenyl-capped tetraaniline used here as opposed to the phenyl/amine-capped ones in most previous literature reports.[21] The symmetry can suppress the number of isomers, which leads to more ordered packing and more extended molecular orbitals;[33] and (2) the intimate contact at the interface between the tetraaniline crystal and the bottom graphene electrode as a result of the bottom-up growth, as opposed to the bottom-contact configuration typically used where contact quality is known to be non-ideal (Figure 4.8). The current for the horizontal crystals (red circles) is significantly lower than that observed for their vertical counterparts (Fig. 6i and inset). The conductivity is calculated to be at most ~1.06×10^{-4} S/cm. Therefore, the conductivity along the backbone of the oligomer crystals (i.e. c-axis) is at least five orders of magnitude lower than that along the π-π stacking b-axis (Figure 4.7e).

The observed anisotropic transport in tetraaniline crystals is most likely a result of the different conduction mechanisms operating along the various crystallographic orientations. Due to the short conjugation length of tetraaniline, the carrier transport along the molecule's backbone is limited and relies on a hopping mechanism between molecules.[34-36] In contrast, the extended conduction network comprised of π-orbital overlap is more efficient, therefore leading to a higher conductivity.[37,38] The fact that the vertical direction is the most efficient conduction pathway with a high conductivity renders these structures important for applications that can benefit from directional 3-D transport such as organic solar cells, batteries, or sensors.[4,39,40]

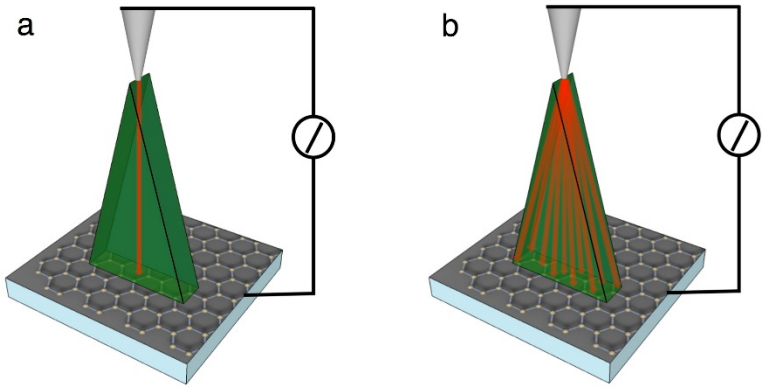

Figure 4.8. **Schematic of the two possibilities for carriers to travel between the top AFM tip and bottom graphene electrodes. a.** If the conductivity along the b-axis is significantly higher than the other axes. **b.** If the conductivity is higher along other axes. The red arrow lines represent the travel pathway of carriers from the conductive AFM tip to the bottom graphene layer.

In order to harness the current for all the vertical crystals collectively, another layer of graphene can be laminated on top of the crystal arrays to make a graphene/tetraaniline/graphene (Gr/TANI/Gr) sandwich structure. Figure 4.7f illustrate a top-view device schematic with the cross-sectional structure shown in Figure 4.7g. Figure 4.9a depicts the fabrication process.

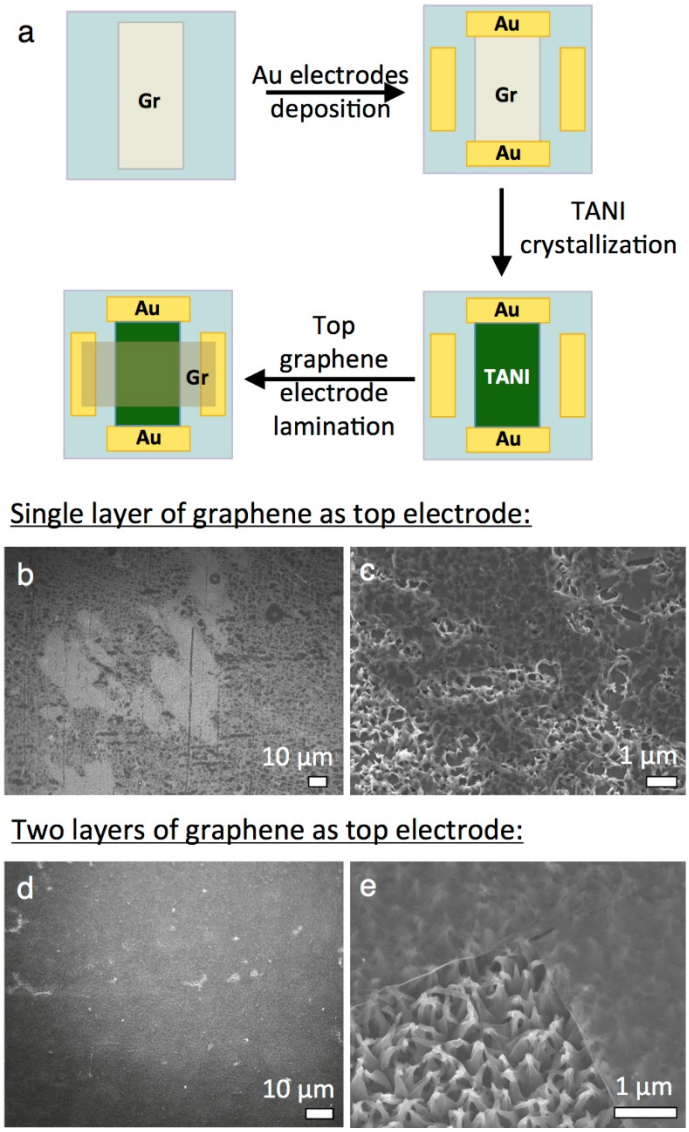

Figure 4.9 | Schematic for fabrication of a(Gr/TANI/Gr) sandwich structure. **a.** Fabrication steps for the graphene/TANI/graphene sandwiched devices. **b. and c.** SEM images showing when a single layer of CVD graphene is laminated on top of the crystal arrays as the top electrode, as compared to **d. and e.** when two layers of graphene are used.

We found that a single layer of graphene does not have the mechanical strength to withstand the spiky crystal tips (Figure 4.9b, c); however, two layers of graphene can serve as a rigid, continuous top electrode for the vertical crystal arrays (Figure 4.6h). A tilted SEM image taken at an edge of the graphene top electrode (Figure 4.6h inset), shows that the bilayer graphene is

indeed laminated on top of the crystal tips. I-V curves for the undoped vertical crystal arrays and that after HCl vapor doping are shown in Fig. 2j. Prior to acid doping, an insulating baseline was obtained, indicating that the top and bottom layers of graphene were separated by the undoped crystal arrays. Once doped, approximately 1.25 mA of current were detected at an applied voltage of 1.0 V. The current scale for arrays is three orders of magnitude higher than that of a single vertical crystal measured by cAFM, indicating that the vertical crystals sandwiched between graphene are indeed connected in parallel where their current can be harnessed collectively, illustrating the potential of such a structure for large-area device applications.

Patterning of electronic materials is vital for defining device position, down-sizing component dimensions and minimizing inter-device cross-talk.[41-43] Unfortunately, this is challenging for organic materials due to their sensitivity to the harsh processing conditions involved in conventional lithography methods.[12,15] However, because of the high nucleation selectivity tetraaniline exhibits for graphene, the deposition locations of tetraaniline crystal arrays can be precisely controlled simply by patterning the graphene substrates. Figure 4.10a shows an optical microscope image of graphene dots that are 10 μm in diameter patterned via photolithography. After the tetraaniline crystallization, only the area covered by the graphene dots turned dark, indicative of tetraaniline binding, while the SiO_2 area remains intact (Figure 4.10b). An SEM image of a 4 by 4 dot array further illustrates the high selectivity that tetraaniline crystals have for graphene (Figure 4.10c). Tilted and more magnified images in Figure 4.10d and e confirm the vertically-oriented nature of the crystals and the sharp interface between the graphene covered and the SiO_2 covered areas.

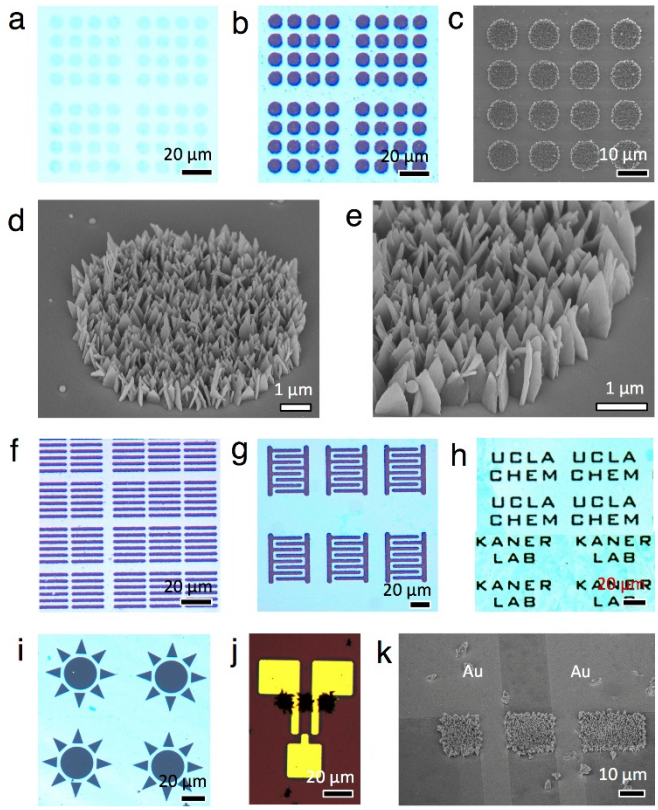

Figure 4.10 | Patterning of vertical organic crystal arrays. a. Patterned graphene on a SiO_2/Si substrate. The blue circles are graphene. **b**. Same substrate after crystallization. Tetraaniline crystals only grow on the circular-shaped graphene, leaving the SiO_2 area intact. **c**. SEM image of a 4×4 circle pattern array showing the high selectivity of the growth location. **d**. Tilted view of an array of vertical crystals arranged in the shape of the graphene substrate. **e**. A magnified view of a corner of the circle in d. **f-i**. Tetraaniline vertical crystal arrays grown in the shapes of lines, interdigitated electrodes, letters, and suns, respectively. **j**. Vertical crystals selectively grown onto a patterned graphene FET with Ti/Au top contact electrodes. **k**. SEM image showing the crystal arrays grown on the graphene strip in j.

Other patterns of vertically-oriented tetraaniline crystal arrays can also be readily created by patterning graphene into desired shapes at desired locations; for example, different sizes of micro-scaled lines, interdigitated electrodes, letters making up the words "UCLA CHEM" and "KANER LAB," suns, triangles and the entire alphabet can be made via the growth of vertical crystals (Figure 4.10f-i). Since the photolithography patterning step is carried out before the tetraaniline crystallization process, this approach is completely benign towards the intrinsic

properties of conjugated materials and can lead to exciting new opportunities for patterning, miniaturization, and prevention of cross-talk in organic electronic devices.

This graphene-assisted vertical crystallization method is also widely applicable to other solution-soluble conjugated materials. As a proof-of-concept, using the solvent-annealing method and the solvent systems demonstrated in Figure 4.1j, vertically-oriented crystal arrays of octaaniline (Fig. 10a), sexithiophene (Figure 4.10c), and bis(*N*-carbozolyl) biphenyl (Figure 4.10e) have been produced on graphene.

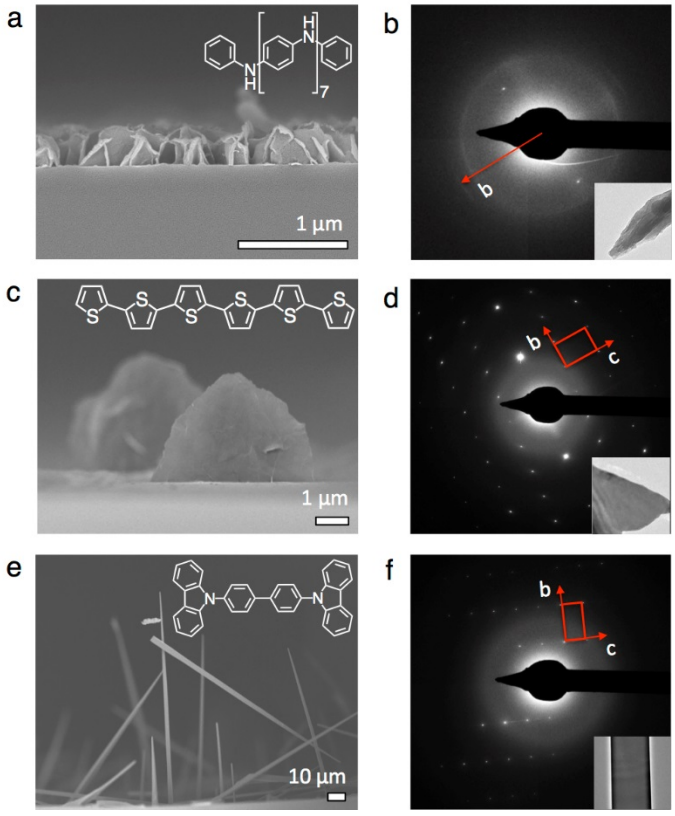

Figure 4.11 | Vertical crystallization of other soluble conjugated compounds on graphene. a. Vertically oriented octaaniline plates. **b**. SAED pattern of a single octaaniline plate showing the preferred packing orientation. **c**. Sexithiophene vertical plates. The density of the plates is low because of the poor solubility of sexithiophene in virtually all solvents. **d**. Spot pattern from the SAED of a sexithiophene plate illustrates it is a single crystal. **e**. Vertical wires of bis(*N*-carbozolyl) biphenyl. **f**. The corresponding SAED pattern shows that each wire is a single crystal.

The former two exhibit plate-like morphology, while the latter appears as 1-D wires. The corresponding SAED patterns for the vertical crystals dry-transferred to TEM grids are shown in Figure2.11b, d, and f, respectively. The interfacial stacking distances for these three crystals are 0.38, 0.39, and 0.37 nm, respectively, and all oriented along their crystal long-axis. The octaaniline plates appear to have preferential orientational packing, as indicated by the arc-pattern in SAED, rather than single crystalline as in the case for tetraaniline. This suggests that the higher molecular weight of octaaniline renders the molecular chains more flexible in conformations, thus allowing them to be packed in a preferred orientation, but with some molecular misorientations, leading to the arc-SAED pattern along the long axis of the plate. In contrast, sharp Bragg spots are obtained for both sexithiophene and bis(*N*-carbozolyl) biphenyl crystals under SAED analysis, demonstrating their single-crystalline nature. Therefore, graphene-assisted crystallization can be a general approach for obtaining vertically-oriented arrays of a wide variety of soluble conjugated materials. With graphene also conveniently serving as a bottom electrode, this method can create exciting new opportunities and potentially lead to technological advances for applications that benefit from ordered 3-D structures such as organic solar cells, sensors, batteries and supercapacitors.

Future Directions:

CVD graphene can be transferred to a variety of substrates beyond rigid semiconductors. In this case we utilized p-doped Si/SiO_2 in order to make a device for conductive AFM testing, but the results obtained for making ordered 3-D structures may translate to flexible substrates as well. The chemical compatibility of the solvents used may limit which substrates can be utilized for this application, but PTFE or other chemical resistant materials may be utilized. Fluorinated polymer substrates are of particular interest because of their ferroelectric behavior. These

polymers, such as polyvinylidene fluoride (PVDF)[49,50], are used in acoustic transducers and electromechanical actuators because of their inherent piezoelectric response. Perhaps coupled with conducting polymers they may be useful as actuators or energy storing devices. The use of ordered organic semiconductors on flexible substrates may lead to a breakthrough in ultralow-cost, lightweight electronic devices or energy storage media such as batteries.

References

1 Fan, Z. Y. *et al.* Three-dimensional nanopillar-array photovoltaics on low-cost and flexible substrates. *Nat Mater* **8**, 648-653, doi:Doi 10.1038/Nmat2493 (2009)

2 Greene, L. E. *et al.* General route to vertical ZnO nanowire arrays using textured ZnO seeds. *Nano letters* **5**, 1231-1236, doi:Doi 10.1021/Nl050788p (2005)

3 Ng, H. T. *et al.* Single crystal nanowire vertical surround-gate field-effect transistor. *Nano letters* **4**, 1247-1252, doi:Doi 10.1021/Nl049461z (2004)

4 Zhao, Y. S., Wu, J. S. & Huang, J. X. Vertical Organic Nanowire Arrays: Controlled Synthesis and Chemical Sensors. *Journal of the American Chemical Society* **131**, 3158-+, doi: 10.1021/Ja809360v (2009)

5 Thurn-Albrecht, T. *et al.* Ultrahigh-density nanowire arrays grown in self-assembled diblock copolymer templates. *Science* **290**, 2126-2129, doi:Doi 10.1126/Science.290.5499.2126 (2000)

6 Hu, J. C., Clark, K. W., Hayakawa, R., Li, A. P. & Wakayama, Y. Enhanced Electrical Conductivity in Poly(3-hexylthiophene)/Fluorinated Tetracyanoquinodimethane Nanowires Grown with a Porous Alumina Template. *Langmuir : the ACS journal of surfaces and colloids* **29**, 7266-7270, doi:Doi 10.1021/La304499k (2013)

7 Singh, V. *et al.* High Thermal Conductivity of Chain Oriented Amorphous Polythiophene. *Nat Nanotechnol*, doi:10.1038/NNANO.2014.44 (2014)

8 Salleo, A. Charge transport in polymeric transistors. *Materials Today* **10**, 38-45 (2007)

9 Wang, C. L., Dong, H. L., Hu, W. P., Liu, Y. Q. & Zhu, D. B. Semiconducting pi-Conjugated Systems in Field-Effect Transistors: A Material Odyssey of Organic Electronics. *Chemical Reviews* **112**, 2208-2267, doi:Doi 10.1021/Cr100380z (2012)

10 Sondergaard, R., Hosel, M., Angmo, D., Larsen-Olsen, T. T. & Krebs, F. C. Roll-to-roll fabrication of polymer solar cells. *Materials Today* **15**, 36-49 (2012)

11 Lim, J. A., Liu, F., Ferdous, S., Muthukumar, M. & Briseno, A. L. Polymer semiconductor crystals. *Materials Today* **13**, 14-24 (2010)

12 Minemawari, H. *et al.* Inkjet printing of single-crystal films. *Nature* **475**, 364-367, doi:Doi 10.1038/Nature10313 (2011)

13 Diao, Y. *et al.* Solution coating of large-area organic semiconductor thin films with aligned single-crystalline domains. *Nat Mater* **12**, 665-671, doi:Doi 10.1038/Nmat3650 (2013)

14 Huang, Y., Duan, X. F., Wei, Q. Q. & Lieber, C. M. Directed assembly of one-dimensional nanostructures into functional networks. *Science* **291**, 630-633, doi:Doi 10.1126/Science.291.5504.630 (2001)

15 Liu, S., Wang, W. M., Briseno, A. L., Mannsfeld, S. C. B. & Bao, Z. Controlled Deposition of Crystalline Organic Semiconductors for Field-Effect-Transistor Applications. *Advanced Materials* **21**, 1217-1232, doi:10.1002/adma.200802202 (2009)

16 Robinson, J. T. *et al.* Vertical nanowire electrode arrays as a scalable platform for intracellular interfacing to neuronal circuits. *Nat Nanotechnol* **7**, 180-184, doi:Doi 10.1038/Nnano.2011.249 (2012)

17 Xu, S. *et al.* Self-powered nanowire devices. *Nat Nanotechnol* **5**, 366-373, doi:Doi 10.1038/Nnano.2010.46 (2010)

18 Tomioka, K., Yoshimura, M. & Fukui, T. A III-V nanowire channel on silicon for high-performance vertical transistors. *Nature* **488**, 189-+, doi:Doi 10.1038/Nature11293 (2012)

19 Miller, J. R., Outlaw, R. A. & Holloway, B. C. Graphene Double-Layer Capacitor with ac Line-Filtering Performance. *Science* **329**, 1637-1639, doi:Doi 10.1126/Science.1194372 (2010)

20 Wang, Y. *et al.* Morphological and Dimensional Control via Hierarchical Assembly of Doped Oligoaniline Single Crystals. *Journal of the American Chemical Society* **134**, 9251-9262, doi:Doi 10.1021/Ja301061a (2012)

21 Wang, Y., Tran, H. D., Liao, L., Duan, X. F. & Kaner, R. B. Nanoscale Morphology, Dimensional Control, and Electrical Properties of Oligoanilines. *Journal of the American Chemical Society* **132**, 10365-10373, doi:Doi 10.1021/Ja1014184 (2010)

22 Li, D., Huang, J. X. & Kaner, R. B. Polyaniline Nanofibers: A Unique Polymer Nanostructure for Versatile Applications. *Accounts Chem Res* **42**, 135-145, doi:Doi 10.1021/Ar800080n (2009)

23 Li, X. S. *et al.* Large-Area Synthesis of High-Quality and Uniform Graphene Films on Copper Foils. *Science* **324**, 1312-1314, doi:Doi 10.1126/Science.1171245 (2009)

24 Novoselov, K. S. *et al.* Electric field effect in atomically thin carbon films. *Science* **306**, 666-669, doi:Doi 10.1126/Science.1102896 (2004)

25 Tung, V. C., Allen, M. J., Yang, Y. & Kaner, R. B. High-throughput solution processing of large-scale graphene. *Nat Nanotechnol* **4**, 25-29, doi:Doi 10.1038/Nnano.2008.329 (2009)

26 Strong, V. *et al.* Patterning and Electronic Tuning of Laser Scribed Graphene for Flexible All-Carbon Devices. *Acs Nano* **6**, 1395-1403, doi:Doi 10.1021/Nn204200w (2012)

27 Novoselov, K. S. *et al.* A roadmap for graphene. *Nature* **490**, 192-200, doi:Doi 10.1038/Nature11458 (2012)

28 Xiao, K. *et al.* Surface-Induced Orientation Control of CuPc Molecules for the Epitaxial Growth of Highly Ordered Organic Crystals on Graphene. *Journal of the American Chemical Society* **135**, 3680-3687, doi:Doi 10.1021/Ja3125096 (2013)

29 Wang, Q. H. & Hersam, M. C. Room-temperature molecular-resolution characterization of self-assembled organic monolayers on epitaxial graphene. *Nat Chem* **1**, 206-211, doi:Doi 10.1038/Nchem.212 (2009)

30 Smallwood, I. M. *Handbook of Organic Solvent Properties*. (Elsevier, 1996)

31 Li, Z. T. *et al.* Effect of airborne contaminants on the wettability of supported graphene and graphite. *Nat Mater* **12**, 925-931, doi:Doi 10.1038/Nmat3709 (2013)

32 Vekilov, P. G. Nucleation. *Crystal Growth & Design* **10**, 5007-5019, doi:Doi 10.1021/Cg1011633 (2010)

33 MacDiarmid, A. G., Zhou, Y. & Feng, J. Oligomers and isomers: new horizons in poly-anilines. *Synthetic Met* **100**, 131-140 (1999)

34 Ma, Z. Y., Geng, Y. H. & Yan, D. H. Extended-chain lamellar packing of poly(3-butylthiophene) in single crystals. *Polymer* **48**, 31-34, doi:Doi 10.1016/J.Polymer.2006.10.034 (2007)

35 Xiao, X. L., Hu, Z. J., Wang, Z. B. & He, T. B. Study on the Single Crystals of Poly(3-octylthiophene) Induced by Solvent-Vapor Annealing. *J Phys Chem B* **113**, 14604-14610, doi:Doi 10.1021/Jp9064505 (2009)

36 Kim, D. H. *et al.* Single-crystal polythiophene microwires grown by self-assembly. *Advanced Materials* **18**, 719-+, doi:Doi 10.1002/Adma.200502442 (2006)

37 Nardes, A. M., Kemerink, M. & Janssen, R. A. J. Anisotropic hopping conduction in spin-coated PEDOT : PSS thin films. *Phys Rev B* **76**, doi:Artn 085208 Doi 10.1103/Physrevb.76.085208 (2007)

38 Sundar, V. C. *et al.* Elastomeric transistor stamps: Reversible probing of charge transport in organic crystals. *Science* **303**, 1644-1646 (2004)

39 Mayer, A., Scully, S., Hardin, B., Rowell, M. & McGehee, M. Polymer-based solar cells. *Materials Today* **10**, 28-33, doi:10.1016/s1369-7021(07)70276-6 (2007)

40 Cui, L. F., Ruffo, R., Chan, C. K., Peng, H. L. & Cui, Y. Crystalline-Amorphous Core-Shell Silicon Nanowires for High Capacity and High Current Battery Electrodes. *Nano letters* **9**, 491-495, doi:Doi 10.1021/Nl8036323 (2009)

41 Briseno, A. L. *et al.* Patterning organic single-crystal transistor arrays. *Nature* **444**, 913-917, doi:10.1038/nature05427 (2006)

42 De Vusser, S., Steudel, S., Myny, K., Genoe, J. & Heremans, P. Integrated shadow mask method for patterning small molecule organic semiconductors. *Applied Physics Letters* **88**, doi:Artn 103501Doi 10.1063/1.2182008 (2006)

43 Menard, E. *et al.* Micro- and nanopatterning techniques for organic electronic and optoelectronic systems. *Chemical Reviews* **107**, 1117-1160, doi:Doi 10.1021/Cr050139y (2007)

44 Chen, S. S. *et al.* Millimeter-Size Single-Crystal Graphene by Suppressing Evaporative Loss of Cu During Low Pressure Chemical Vapor Deposition. *Advanced Materials* **25**, 2062-2065, doi:Doi 10.1002/Adma.201204000 (2013)

45 Li, X. S. *et al.* Transfer of Large-Area Graphene Films for High-Performance Transparent Conductive Electrodes. *Nano letters* **9**, 4359-4363, doi:Doi 10.1021/Nl902623y (2009)

46 Denis, P.A. Organic Chemistry of Graphene: The Diels-Alder Reaction. *Chemistry-A European Journal* **19**,46, 15719-15725,doi:Doi10.1002/chem.201302622 (2013)

47 Bekyarova, Elena, et al. "Chemical modification of epitaxial graphene: spontaneous grafting of aryl groups." *Journal of the American Chemical Society* **131**,4: 1336-1337,doi:Doi10.1021/ja8057327 (2009)

48 Lee, Wi Hyoung, et al. "Surface-directed molecular assembly of pentacene on monolayer graphene for high-performance organic transistors." *Journal of the American Chemical Society* **133**.12, 4447-4454, doi:Doi dx.doi.org/10.1021/ja1097463 (2011)

49 Ni, Guang-Xin, et al. "Graphene–ferroelectric hybrid structure for flexible transparent electrodes." *ACS nano* **6**.5: 3935-3942, doi:Doi10.1021/nn3010137 (2012)

50 Tan, Wei-Chun, Wei-Heng Shih, and Yang Fang Chen. "A Highly Sensitive Graphene-Organic Hybrid Photodetector with a Piezoelectric Substrate." *Advanced Functional Materials*,doi: DOI: 10.1002/adfm.201401421 (2014)

Chapter 5: CVD Graphene as a New Membrane Material for Ultrafiltration and Water Desalination

The field of membrane science constantly advances and evolves as new materials emerge[1,2] that increase flux, improve fouling resistance, and increase rejection. Due to its atomic thickness[8-10] and chemical and mechanical stability[11], graphene has emerged as a potential membrane candidate for water treatment. We set out to explore whether graphene would make a feasible membrane under true field operating conditions.

Water scarcity fuels membrane research:

As I write this, California is in the midst of the worst drought of the past century. The result of this has led to fierce wildfires, water shortages and restrictions, and potentially staggering agricultural losses. The ironic thing is California sits next to the Pacific Ocean and as recollected from the Rime of the Ancient Mariner, residents observe "Water, water, everywhere, nor any drop to drink." Of course, California's water troubles highlight that even in technologically advanced societies, water scarcity is still an ongoing problem. Indeed access to clean potable water for human consumption is a very large global problem as well[3]. As illustrated in Figure 5.1, water scarcity will continue to increase especially in developing nations as populations increase globally.

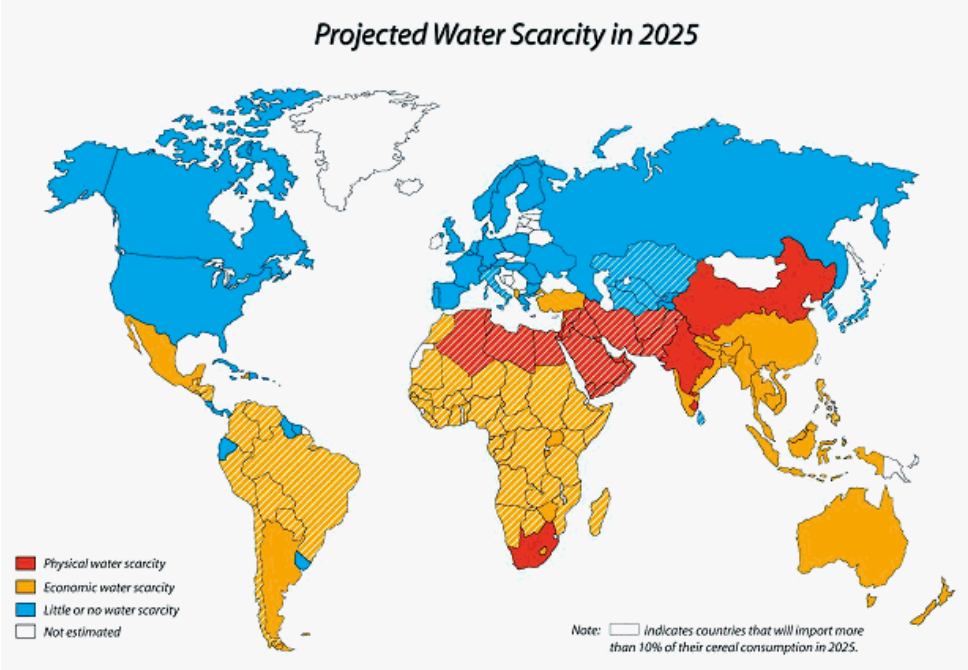

Figure 5.1 | The projected global map of water scarcity in 2025. Source:waternunc.com

Water reclamation and treatment will become more important as access to potable water declines.

At their heart, water filtration membranes work on the principle of size exclusion and the degree of selectivity of a membrane depends on the membrane pore size. Depending on the pore size, they can be classified as microfiltration (MF), ultrafiltration (UF), nanofiltration (NF) and reverse osmosis (RO) membranes. As wonderfully illustrated in Figure 5.2, the types of contaminants that can be removed by filtration membranes include metal ions, antibiotics, viruses, bacteria, and plastics.

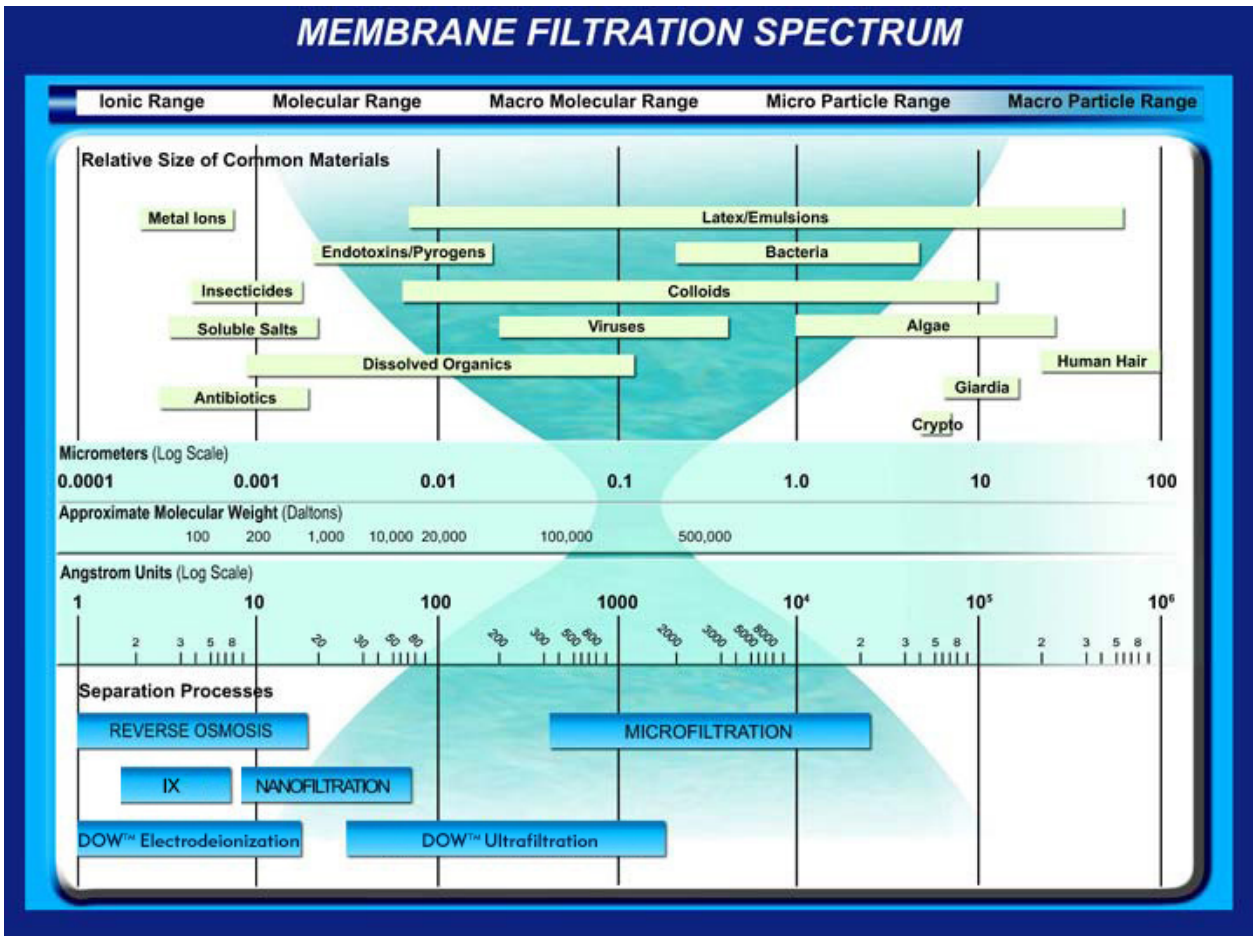

Figure 5.2 | The spectrum of water filtration technology by membrane pore size.

NF and RO are of particular interest due to their ability to treat waste/brackish water from industry and salt water from the ocean for the production of potable water. Indeed, these two technologies work in tandem to remove smaller and smaller particulates and increase the efficiency of the proceeding filtration process. Water's role in industry ranges from fracking to chemical production and will increase globally as developing nations industrialize. Even in the U.S., the ability to recycle waste water will help to keep costs low and minimize environmental pollution. Desalination of ocean water may be the long-term remedy to the shortage of water in the near future. It should be noted that the majority of human populations reside near coastlines

and saltwater treatment will play a crucial role in providing water security for many nations around the globe.

Any membrane process will depend on three key elements: flux, pressure, and rejection. Flux describes how fast water can permeate through a membrane, pressure is needed to overcome forces such as osmotic pressure in RO and to drive the permeate through a membrane, and rejection is the amount of particles that have been removed from the feed water. Flux and rejection can be understood as how fast and how well water can be treated, respectively.

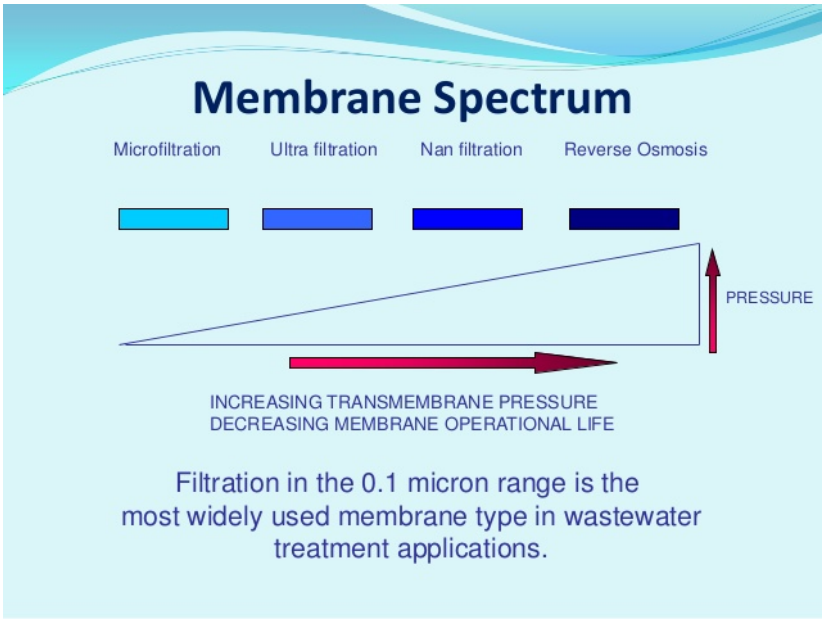

Figure 5.3 | The relationship between pore size and transmembrane pressure.

As the particle size decreases, the amount of pressure required to drive the permeate through the membrane increases. In RO desalination, for example, pressure is applied to the feed water to overcome osmotic pressure through an RO membrane. The process requires that a high pressure be exerted on the feed side of the membrane, usually 50-300 psi for surface and brackish water, and 500-1,000 psi for seawater, to overcome the osmotic pressure corresponding to the salt concentration. For comparison, the air pressure in a passenger car's tires range from 20-35 psi.

Graphene membranes exhibit the ideal properties to decrease flux:

Membrane flux is inversely related to the thickness of the membrane. In the case of a graphene membrane, the membrane thickness would effectively be the size of one carbon atom. Interest in graphene membranes has picked up considerably since 2010[10,19-25]. The dynamics of transport of both water and ions across a graphene membrane have been closely studied. Suk and Aluru[5] carried out molecular dynamic simulations and found that the water transport through graphene occurs through a single file of two molecule chains for a sufficiently small pore size as seen in Figure 5.5. The simulation consisted of a graphene membrane with a 0.75 nm pore diameter with 6 nm of water on either side of the graphene membrane under 100 MPa (14.5 Kpsi) pressure to drive the system.

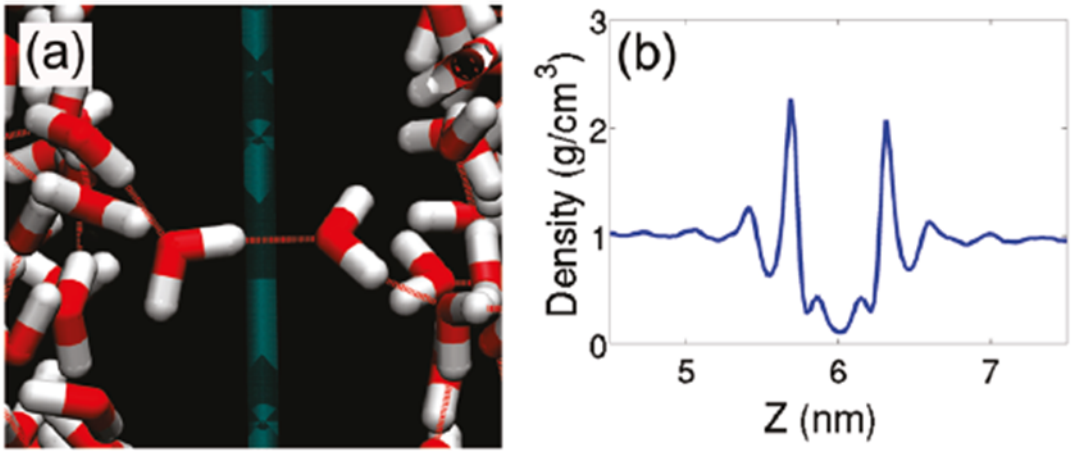

Figure 5.4 | Simulated water transport dynamics through a graphene membrane: a. Simulation of two molecule single-file water configuration across a 0.75 nm diameter pore; **b.** Density distribution of water molecules across the membrane. Concentration peaks near the graphene at z = 6 nm indicate favorable water position forming the single-file structure. (reprinted with permission[5] © American Chemical Society).

The density peaks of water molecules can be seen on either side of the graphene membrane. Their presence demonstrates that water molecules on either side of the membrane can interact in

a favorable position near the graphene membrane. As a consequence to the formation of the two molecule chain, the hydrogen bond interaction is much weaker in the water chains across graphene and both water molecules are more likely to flip their orientation and break the hydrogen bond, and subsequently, the two member chain. This may lead to a decrease in water flux and warrants further investigation.

Ionic transport through graphene is of equal interest for water desalination as well. Tanugi and Grossman[6] utilized molecular dynamic simulations to examine the effects of desalination across a graphene membrane. They came to the conclusion that desalination dynamics change with pore size, pore chemistry, and applied hydrostatic pressure. In the study, the initial system consisted of a box measuring 75 Å in the z-direction and periodic x−y plane with a unit cell cross-section of 30 × 30 Å. The graphene membrane was fixed at z = 60 Å, and a rigid piston was originally placed at z = 0 and subsequently allowed to push the water toward the membrane at a prescribed external pressure. The graphene membrane was modeled with a single pore varying in size from 1.5 to 62 Å. The saltwater in the system was modeled by 825 water molecules along with 16 Na and 16 Cl ions, which resulted in a salt concentration of 72 g/L, roughly twice the concentration of seawater. An applied pressure of 100-200 MPa was introduced to the feed water to simulate the RO process. The flow rate increases with pore size and applied pressure. The permeability scales linearly with pore area, as expected from the Hagen−Poiseuille equation in classical fluid dynamics[4] for flow across a cylindrical pore as shown in Figure 5.5.

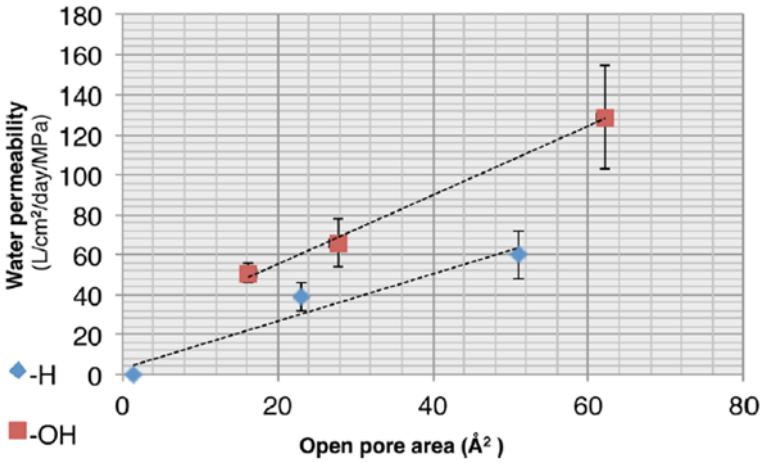

Figure 5.5 | The predicted water permeability of graphene. The blue diamonds denote hydrogenated pores and the red squares denote hydroxylated pores, respectively. (reprinted with permission[6] © American Chemical Society).

In all cases, water permeability was greatly enhanced by the hydroxylation of pores vs. the hydrogenated case. This behavior is due to the fact that hydrophilic functional groups increase the water flux by allowing for a greater number of hydrogen-bonding configurations inside the pore, as in Figure 5.6.

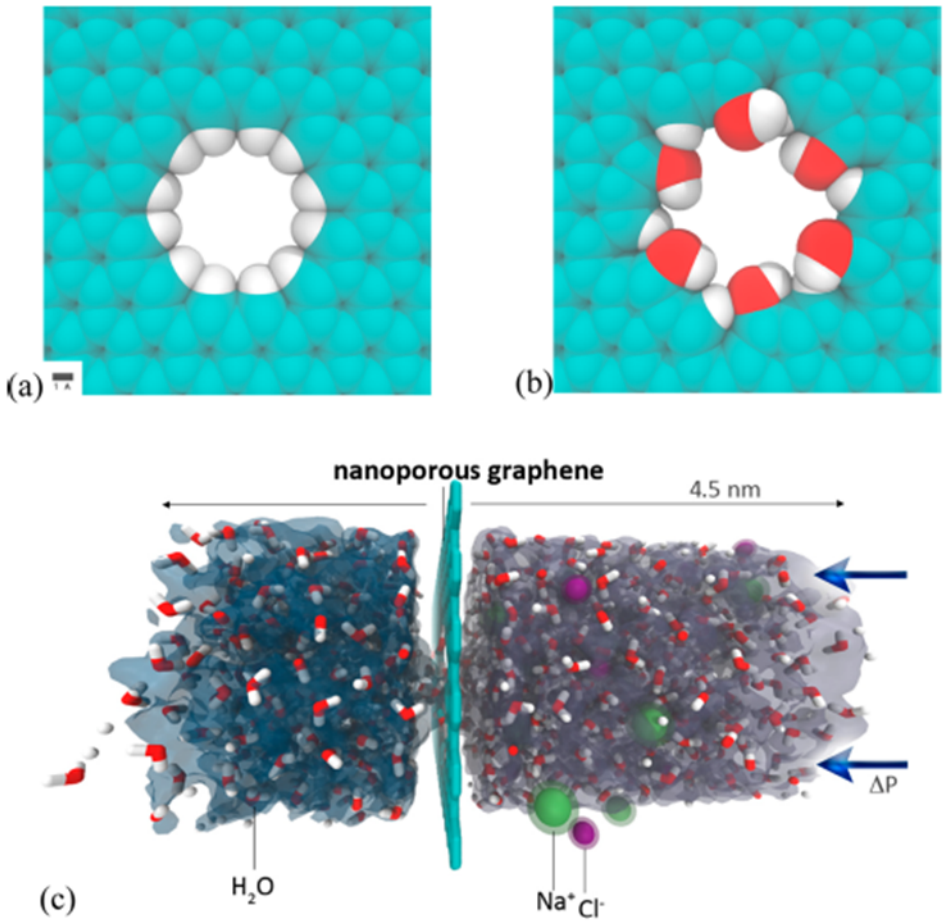

Figure 5.6| Functionalized graphene pores modeled as membranes: a. Hydrogenated and **b**. hydroxylated graphene pores; **c.** side view of modeled molecular dynamics simulation. Permeate is traveling from right to left under 100 MPa pressure. (reprinted with permission[6] © American Chemical Society).

Furthermore, Tanugi and Grossman show that at a maximum diameter of around 5.5 Å, the majority of salt ions approaching the pore entrance are able to pass through the membrane beyond this diameter. Figure 5.7 shows salt rejection as a function of applied pressure, different pore sizes and pore types. The higher number pores denote larger pore sizes and the effects of a deformable membrane under high pressures were considered. A scenario was tested in which the membrane was modeled as a deformable body. In the aspect of salt rejection, the results showed that hydrogenated pores had higher salt rejections than hydroxylated pores. The data also showed

that increasing the applied pressure tended to decrease salt rejection. The authors attribute this to the larger volume of solvated ions relative to water molecules in order to explain the observed salt rejection drop at higher pressures. Although salt and water permeation rates both increase linearly with pressure, the salt has a larger effective volume. Accordingly, the salt flow rate increase is steeper than that of water and results in a lower overall salt rejection with increasing pressure. Furthermore, the effects of a flexible membrane tended to be negligible.

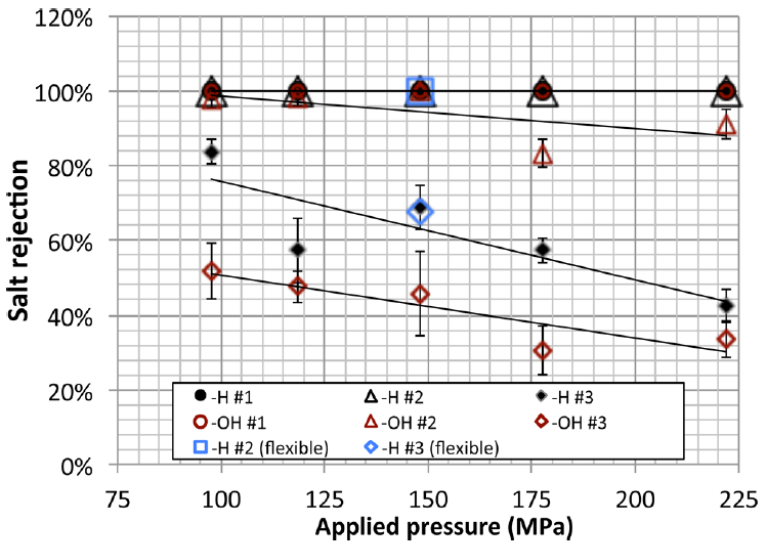

Figure 5.7 | The predicted salt rejection of a graphene membrane as a function of pore type and pressure differential. Hydrogenated pores exhibit a stronger salt rejection performance then the hydroxylated ones. (reprinted with permission[6] © American Chemical Society).

Their calculations demonstrate that water can flow across a graphene membrane at rates in range of 10−100 L/cm^2/day/MPa while still rejecting salt ions, which is 2 to 3 orders of magnitude higher than diffusive RO membranes. Figure 5.8 shows a comparison of graphene membranes to that of commercial RO membranes.

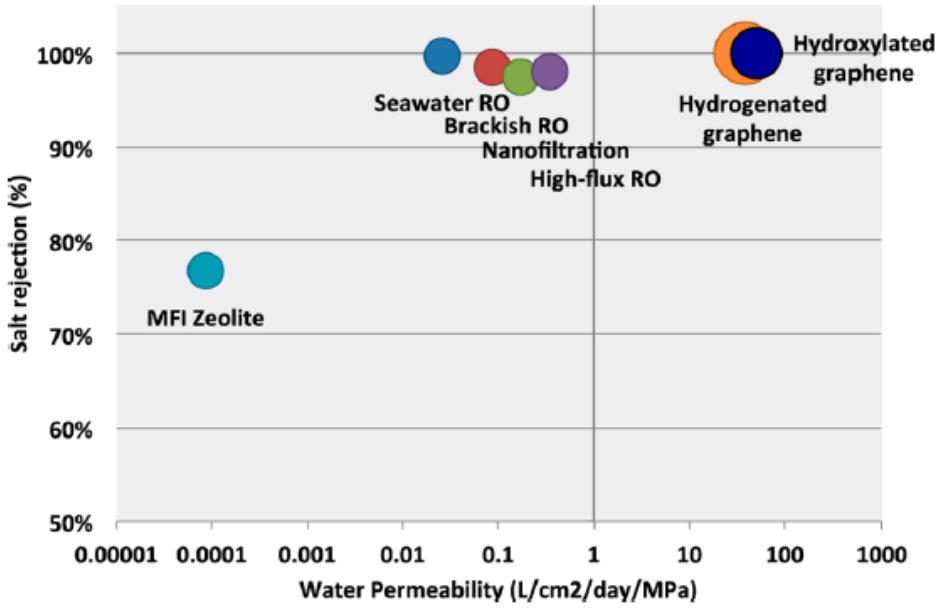

Figure 5.8 | Performance chart for functionalized nanoporous graphene vs. existing technologies. (reprinted with permission[6] © American Chemical Society).

Theoretically, graphene membranes should be capable of desalination with fluxes several orders of magnitude higher than that of existing technologies. Recently, a group from MIT lead by O'Hearn et al. attempted to make graphene membranes for salt rejection[22]. They report graphene composite membranes (GCM) with nominal areas of more than 25 mm^2 fabricated by transfer of a single layer of CVD graphene onto a porous polycarbonate substrate as seen in Figure 5.9.

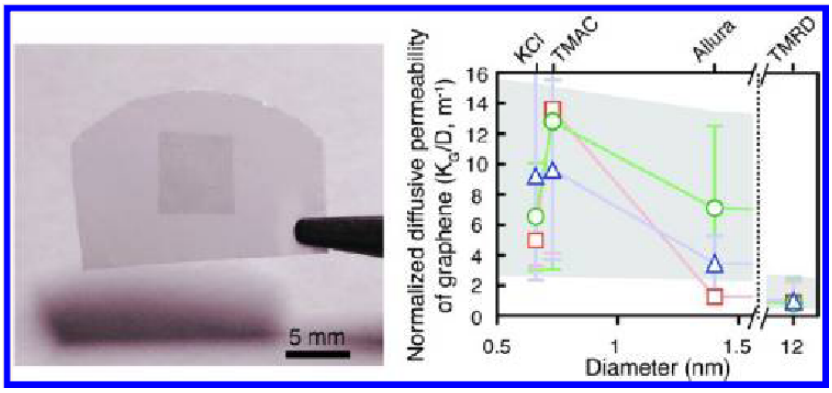

Figure 5.9 | As prepared graphene composite membranes (GCM): a. Single layer graphene transferred onto commercially available PCTE. **b.** Normalized diffusive permeability of graphene. The plot measures size exclusion of various molecular species through a GCM. Size exclusion is reached for TMRD with a diameter of 12 nm. (reprinted with permission[22] © American Chemical Society).

The group selected a polycarbonate track etched (PCTE) membrane with 200 nm pores (Sterlitech) as their target substrate. The straight, cylindrical pores of the membrane present a well-defined transport resistance for extraction of the intrinsic transport properties of graphene and provide adequate porosity, while avoiding excessively large areas of freestanding graphene. The transfer of graphene onto the commercial membrane results in intrinsic defects which are caused by the etching process to remove the underlying copper growth substrate. To mediate the effects of the etchant, APS was used as it is known to gently remove the copper without damaging the graphene film. However careful, the researchers discovered that, unlike pristine graphene, the low-pressure CVD graphene contained pores in the size range of 1-15 nm that appear to be distributed in a pattern analogous to the features on the copper foil used for CVD synthesis. The origin of these intrinsic holes are unclear, but may originate from the growth process itself. It should be noted that the researchers purchased the single layer graphene from Advanced Chemical Suppliers and depending on how the growth was carried out, may contain numerous defects. The presence of contamination from the handling of the copper growth substrates prior to CVD may lead to point defects (i.e. missing carbons in the graphene lattice or

the emergence of five and seven membered rings substituted into the lattice). In the supplemental section of the text, the author reveals the use of multiple transfers in order to alleviate the intrinsic defects of the graphene with slightly improved results.

The group measured the diffusive transport of molecular species of increasing sizes across the GCM: KCl, tetramethylammonium chloride (TMAC), Allura Red AC (496 Da dye), and tetramethylrhodamine dextran (70 kDa, TMRD). In the case of Allura Red and TMRD, which have low diffusivities, pressure gradients across the membrane during transport measurements were eliminated by fluidically connecting both sides to an external reservoir. It should be noted that with all these molecular species whose size is <80 kDa, ultrafiltration techniques should be used including the application of 50-300 psi pressures. Figure 5.10 demonstrates the set up. Here a gravitational pressure head drove the convective transport of 1 mM Allura Red AC solution from bath (1) through graphene composite membrane to bath (2), which then traveled through tubing to bath (3) to equalize liquid level. The change in absorbance in bath (3) was measured via a UV-vis spectrophotometer and used to extract the flow rate. For the diffusive measurement,

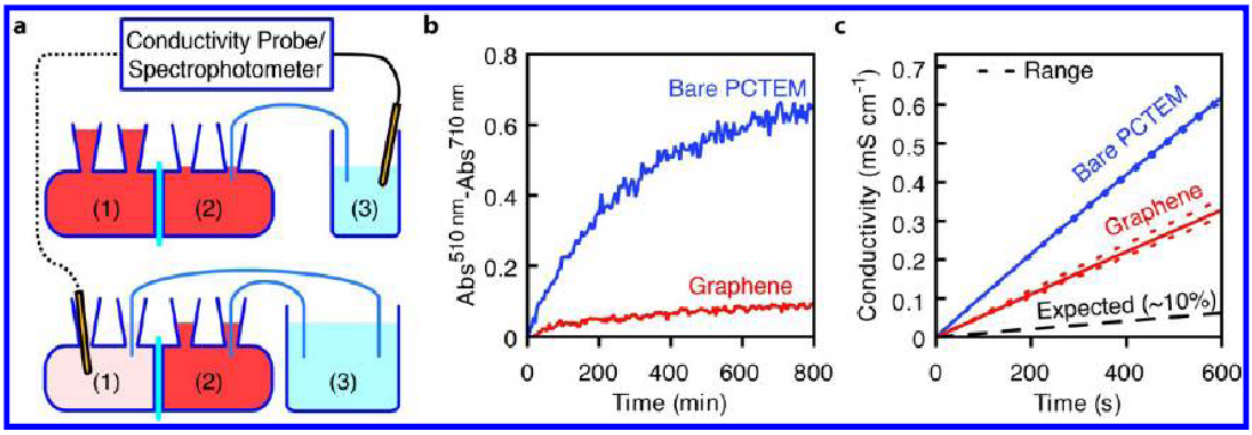

Figure 5.10 | The experimental set-up for diffusion testing of molecular species through GCMs: a. Diffusion testing of molecular species. **B.** Absorbance measurement of control bare PCTE membranes vs experimental GCM. **C.** Ionic conductivity of the control vs. experimental. (reprinted with permission[22] © American Chemical Society).

concentration gradient drives diffusion of solute (e.g., KCl) from bath (2) through GCM to bath (1). Change in conductivity (for salts) or absorbance (for organic molecule solutes) in bath (1) is measured via a UV-vis spectrophotometer or conductivity meter.

Figure 5.10b demonstrates the result of the convective transport through GCM is ~10% that of the bare PCTE membrane (PCTEM), indicating ~90% graphene coverage in GCM.

Figure 5.10c demonstrates that diffusive transport rate of KCl through GCM (M1) is 46% that of the transport through the bare PCTEM, much higher than the expected value of ~10% if the graphene were impermeable. This suggested that the CVD graphene was permeable to KCl. Dashed lines denote the range of data in three different experiments on the membrane. Why did KCl manage to diffuse so easily through the CVD membrane? The authors suspect there are various intrinsic holes that result from either growth of graphene on copper, the etching process, or some combination of both. How large are these holes? The authors attempted to find out by using large 70 kDa TMRD molecules and characterization by STEM. Based on the STEM, the authors conclude a distribution of 1-15 nm intrinsic defects in the CVD graphene.

The diffusivity tests described here required an outstanding ~3-4 weeks for triplicate measurements. O'hearn et al. found that the GCMs permitted transport of KCl and TMAC, but blocked the diffusion of the 70 kDa TMRD. Compared to the bare PCTE membrane, the GCM resulted in ~80-85% decrease in the diffusive flux of TMRD, which is consistent with the pore size distribution and graphene coverage measured using pressure-driven flow (Figure 5.10b). The results are neatly summarized in Figure 5.11a-d.

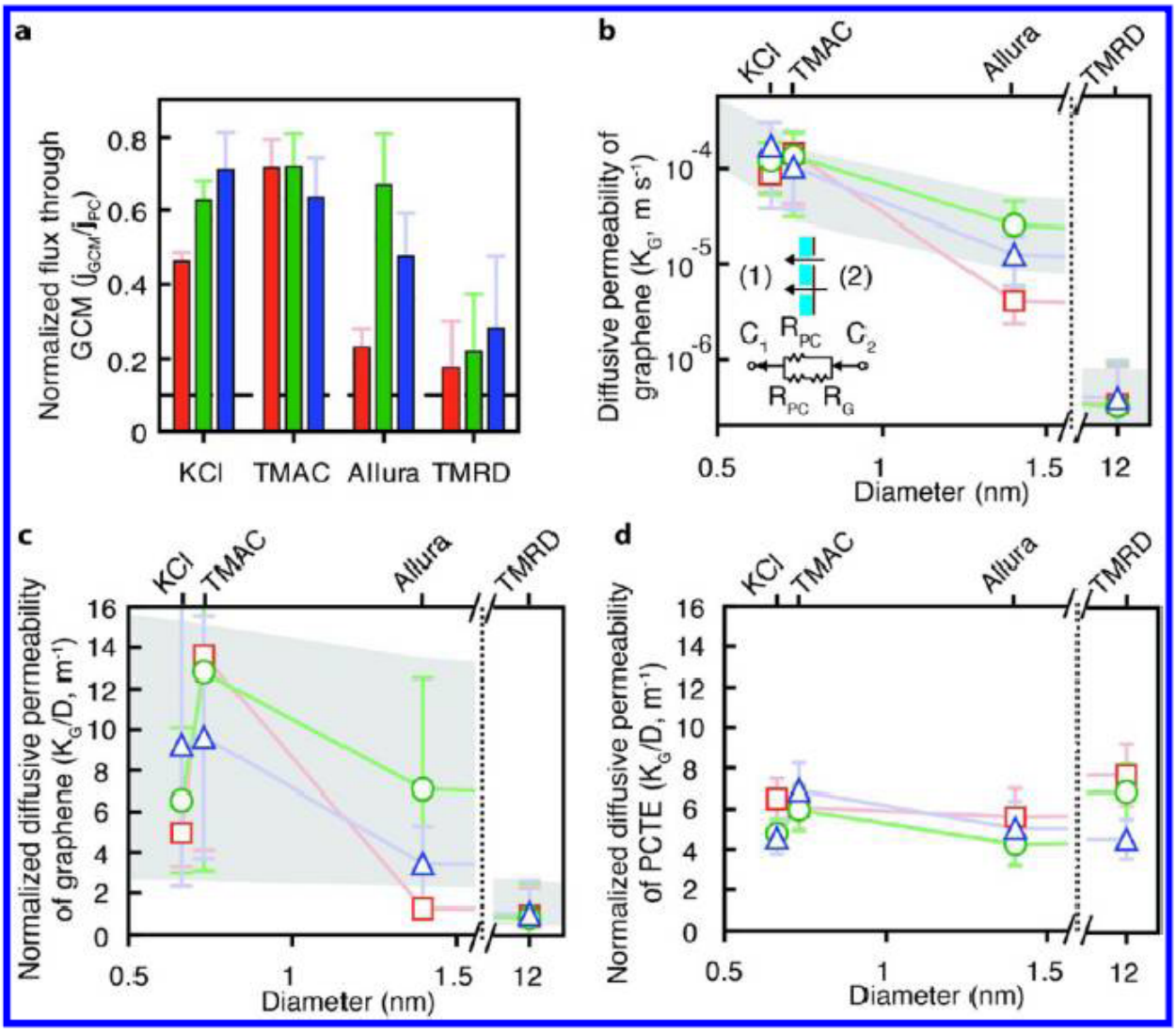

Figure 5.11 | The size-selective diffusion of molecules through GCMs: a. Diffusive flux through GCMs. **b.** Permeability of the CVD graphene indicating the presence of intrinsic nanopores. **C.** Permeability of the graphene normalized by the diffusivity of the molecules. Size selectivity is demonstrated for pore sizes greater than 12 nm. **D.** Measured permeability of the bare PCTE membrane normalized by the diffusivity of the measured molecules. The unmodified membrane shows no size selectivity. (reprinted with permission[22] © American Chemical Society).

As seen in Figure 5.11b, size selectivity exists based on the estimated pore size of the defects in the CVD graphene. Figure 5.11c shows a gray region denoting continuum model prediction with the same porosity range as in Figure 5.11b. In this case only TMRD, whose molecular size is too large to pass through the graphene, is attenuated and falls in line with the model. The agreement

between the experimentally measured permeability and the continuum theory further indicates that the observed transport behavior is due to the nanometer-scale pores in the graphene.

In light of O'hearn's findings, it would appear that CVD graphene may not give the appropriate pore size for RO desalination. Is there any way to further refine this work? Even if GCMs contain intrinsic nanometer pores, their size is suitable for ultrafiltration. However, this study did not approach the use of pressures suitable for RO and/or ultrafiltration as predicted by the theoretical studies of Tanugi and Grossman or as commonly used in applications. Beyond pressures, this study did not utilize samples large enough to demonstrate prototype feasibility.

Several strategies may be applied to provide more definitive results and demonstrate the practical use of graphene for membrane filtration. Use of multilayer graphene may provide a way to circumvent or eliminate intrinsic defects. The use of very dilute APS etchant may allow for larger (>mm^2) and more continuous transfers of graphene films onto plastic substrates. Tighter controls over the synthesis of CVD graphene may eliminate defects and improve the rejection of GCMs. The use of more hydrophobic surfaces than polycarbonate may also increase the affinity of graphene to commercially available membranes and enhance the quality of the transfers.

The use of multilayer graphene as membrane material:

The advantage of graphene films for RO and ultrafiltration are their atomically thin surfaces that increase the flux. However, use of multilayer graphene may be a suitable trade off as they may be more mechanically robust, contain fewer intrinsic defects, and are still less than 20 nm thick.

As described previously, multilayer graphene can be grown by altering the growth conditions on copper[32] or by use of a nickel[33] or copper-nickel[35] alloy catalyst. To differentiate our work from O'hearn, we decided to focus on 25 μm nickel and Cu-Ni alloys for multilayer growth. This was

done to test whether or not multilayer growth can prevent the occurrence of intrinsic defects or stand up to transfer with less micro rips and tears.

We began by testing a range of temperatures that would give us few layer graphene (FLG) as confirmed by Raman and TEM diffraction. As mentioned previously, for a Ni system, the cooling rate also plays a role in the formation of continuous sheets. After testing several conditions ranging from 500-1075 °C for 2-60 minutes of growth time followed by a cooling rate of 2-20 °/min we found that for our system 780 °C, 45 min long growths followed by a cooling rate of 10 °/min was suitable to produce few layer graphene as seen in Figure 5.12. The Raman of this condition reveals the characteristic G peak at 1578 cm^{-1} and the 2D peak at 2702 cm^{-1}. A 2D/G ratio of 0.9 was obtained, which is in line with few layer graphene. For comparison, a ratio of 4 indicates single layer graphene and a ratio of less than 0.5 is graphite[35]. Utilizing TEM and UV-vis spectroscopy, we estimate the number of a layers to be between 20 and 33. This would correspond to a thickness of 6-11 nm.

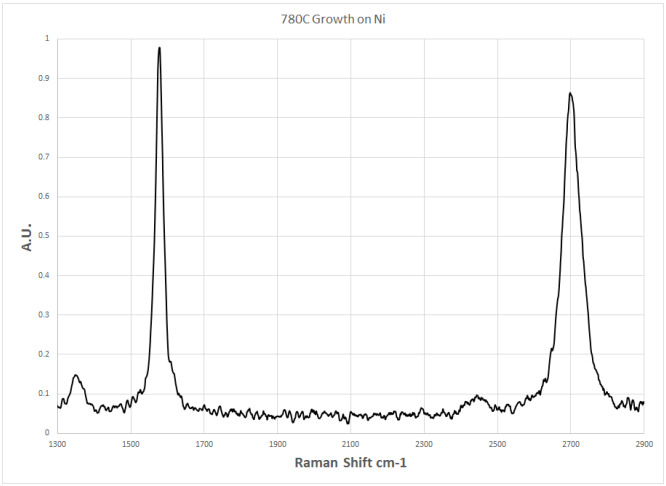

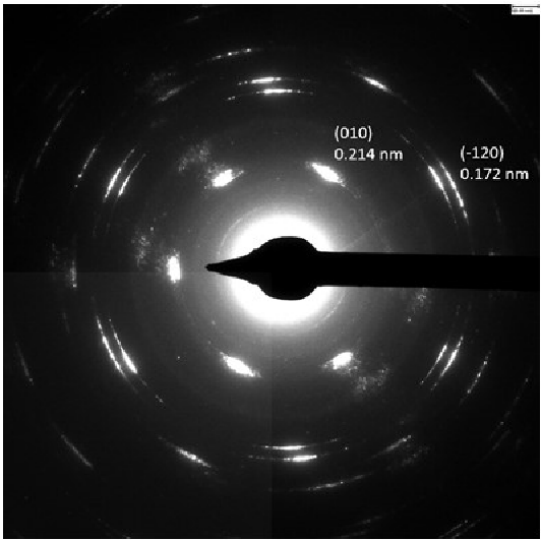

Figure 5.12 | Characterization of as prepared FLG films grown on Ni foil: a. Raman of transferred film. The characteristic G peaks appears at 1578 cm^{-1} and the 2D peak appears at 2702 cm^{-1}. **b.** TEM diffraction pattern of resulting films indicating crystallinity.

We next attempted to transfer 2'"x 2" (or 101 mm^2 nominal surface area) samples of FLG onto commercially available polycarbonate membranes. Our initial attempts involved a process outlined in Figure 5.13.

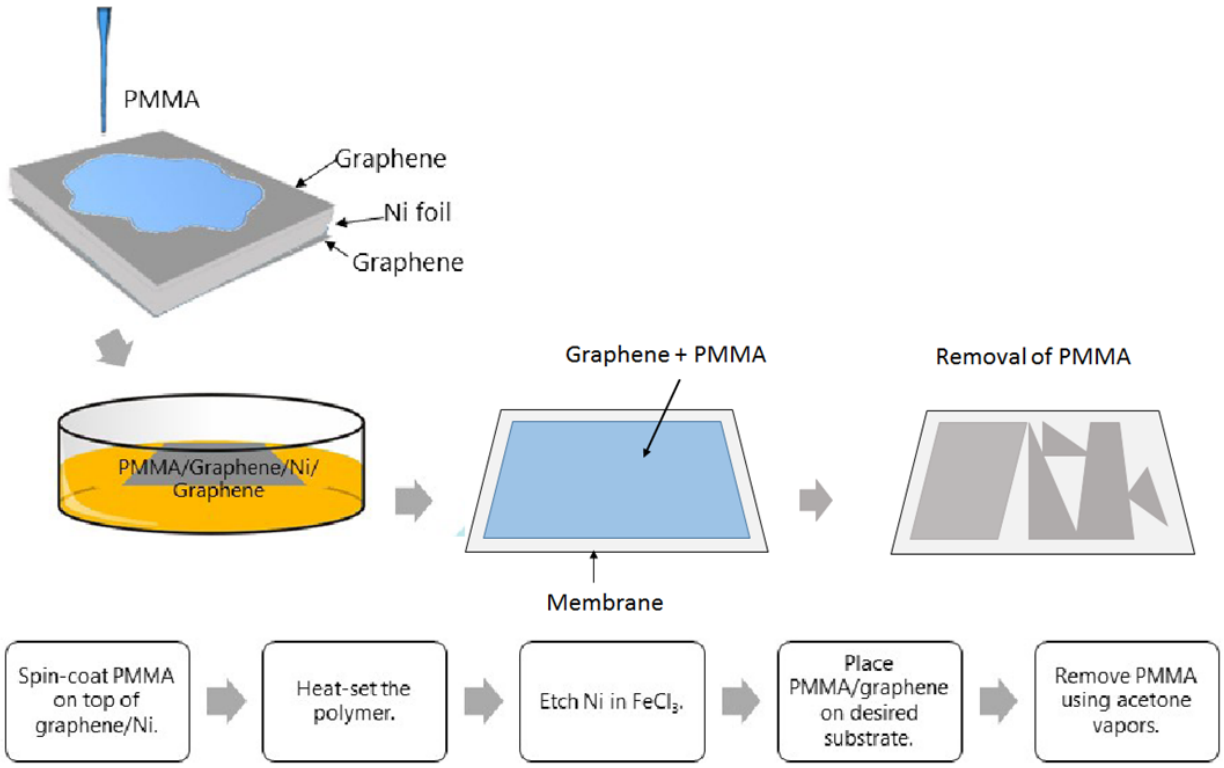

Figure 5.13 | The PMMA assisted transfer of FLG onto polymer membranes.

We used 1000 nm thick films of PMMA to aid in the transfer of the FLG on 25 µm Ni foil. Once PMMA is baked at 160 °C for a few minutes, it becomes cross-linked and difficult to remove. This is desirable when etching the underlying metal foil and manipulating the graphene/PMMA film, but unwanted when trying to isolate the graphene onto the membrane polymer. We initially used polycarbonate membranes (PC) that contained a PVP top layer as the supporting membrane. We transferred the graphene onto the support layer and allowed it to dry either overnight or on a hot plate. We next used acetone vapor to strip away the PMMA gently over the course of a few minutes. The result was warped membrane polymer and discontinuous graphene films. We suspect the reason is the choice of using 0.1 µm polyvinyl alcohol coated polycarbonate (PVA-PC) membranes. These membranes are slightly hydrophilic, whereas the graphene is naturally hydrophobic. Once we wet the membranes with acetone, the vapors that condense will naturally

repel from the hydrophobic graphene and cause tearing. The chemical compatibility of PVA-PC with acetone is also very poor and causes additional warping, but unfortunately, when dealing with PMMA, we have very little options to remove it. We next decided to use a more hydrophobic surface and settled on both Teflon micro-filters available to us in lab and PVP-less PC membranes. These filters are PTFE with 0.45 μm pore sizes and are chemically compatible with acetone. Once again we followed the previous transfer method and this time managed to get good transfers as seen in Figure 5.14

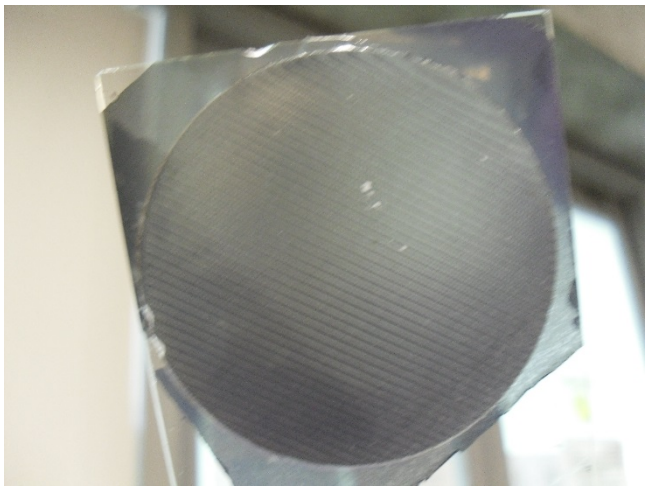

Figure 5.14 | The transfer of FLG onto a commercially available PTFE membrane.

Since we are interested in both ultrafiltration and RO applications for these membranes, we decided to utilize commercially available hydrophobic PC and PTFE with the smallest pore sizes possible. Sterlitech provides both PC and PTFE membranes with track etched pores down to 0.01 and 0.1 μm, respectively. We initially began with the PC membranes, but as we continued to transfer large samples, we had great difficulty in isolating complete sheets. We attributed this to using PMMA as a support layer which we had to subsequently remove with acetone thereby causing unwanted damage to the graphene as well as warping the underlying membrane support.

We decided to not use any supporting polymer layer and directly etch the FLG/Ni substrated in concentrated iron (III) chloride $FeCl_3$.

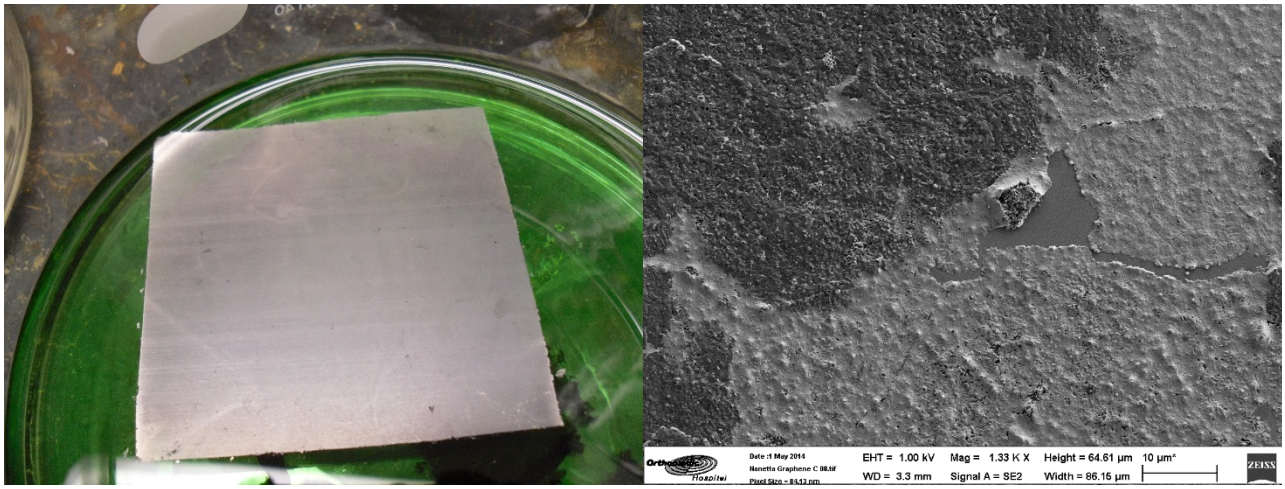

Figure 5.15 | The PMMA-less transfer of FLG: a. Etching of FLG-Ni in $FeCl_3$ and water. **b.** SEM image of as transferred film on Si/SiO_2. The presence of multilayer regions is clearly visible as are transfer induced micro-tears in the sheet.

Unfortunately, there are micro-tears that develop during the transfer process as seen in Figure 5.15 b. As mentioned previously, the transfer of graphene takes place in water and the surface tension of water may pull the graphene sheet apart causing tears. Of course, the concentration of the etchant may also be too high which will lead to aggressive etching of the underlying Ni and create bubbling. The bubbling has been observed in the past and may lead to tears during the transfer. Additionally, it is known that $FeCl_3$ can form crystals that precipitate near grain boundaries[26] of graphene during etching, which may result in tearing. To alleviate this, we attempted transferring graphene in a variety of solvents and with varying concentration of $FeCl_3$ (Figure 5.16).

Figure 5.16 | The solvent effect on the transfer of support layer-less FLG: a. Etching of FLG-Ni in $FeCl_3$ and water. **b.** Etching of FLG-Ni in $FeCl_3$ and ethanol. **c.** Etching of FLG-Ni in $FeCl_3$ and isopropanol.

We used diluted $FeCl_3$ in a 1:6 proportion to water respectively, 1:6 to ethanol, and 1:6 isopropanol. As expected, the surface tension of the solution was altered which led to less pulling on the graphene sheet, but subsequent wrinkling. As the surface tension decreases, the sheet no longer floats and sinks to the bottom. The $FeCl_3$ has various solubility in the organic solutions and as the length of the hydrocarbon chain increases, the solubility of the etchant decreases. As expected, the use of surface tension modification led to less torn graphene, but at the expense of increased etching time and introduced new found wrinkling, which also complicates transfer. The ideal etchant would involve just enough water to dissolve the etchant, just enough alcohol to alter the surface tension, and just enough iron chloride to etch at a reasonable rate. One possible alternative would be to use ammonium persulfate (APS) as the etchant which has been previously described as more gentle on graphene during transfers. Unfortunately, APS has little solubility in alcohol and tends to etch Ni inordinately slow.

Recall that the flux of a membrane is inversely proportional to the thickness of the surface of the membrane. Based on our Ni growths, Raman, TEM, and UV-Vis characterization, we believe we have made FLG that is 11.4 nm thick. Because of the difficulty in etching the Ni in APS, we

decided to try using Cu-Ni alloys to grow FLG. Previous attempts at alloy growth[34] have resulted in few layer graphite because the amount of Ni used was exceedingly thick. Work from Ajayan et al.[36] has demonstrated that use of <500 nm thick films of Ni on top of <1300 nm thick Cu can yield <5 layers of graphene films. We then deposited 400 nm of Ni on top of 25 μm thick (25,000 nm) Cu and attempted to grow FLG. We were motivated to produce less layers of graphene thereby increasing flux, but enough to allow for rigid support during transfer and to possibly prevent intrinsic holes from forming. Furthermore, the Cu would allow for the APS to etch away the alloy in ways the Ni standing alone would not permit.

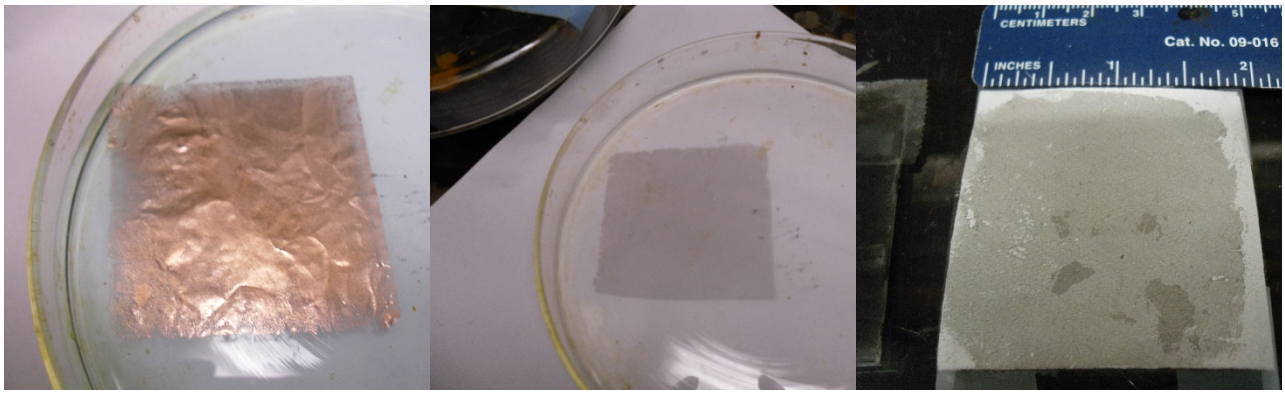

Figure 5.17 | Transfer of FLG grown Cu-Ni alloy: a. Etching of Cu-Ni alloy in APS. As the Cu etches, the solution becomes blue **b.** The resulting etched film is self-supported in water. **c.** Transferred film onto PTFE. There are noticeable tears caused by the transfer process. The extra dark regions on the transferred sample correspond to flakes that were floating in solution, but got trapped beneath the transferred sheet and the membrane support.

As confirmed by Raman, TEM, and UV-Vis, the alloying has produced FLG <9 layer or 3.1 nm thick films.

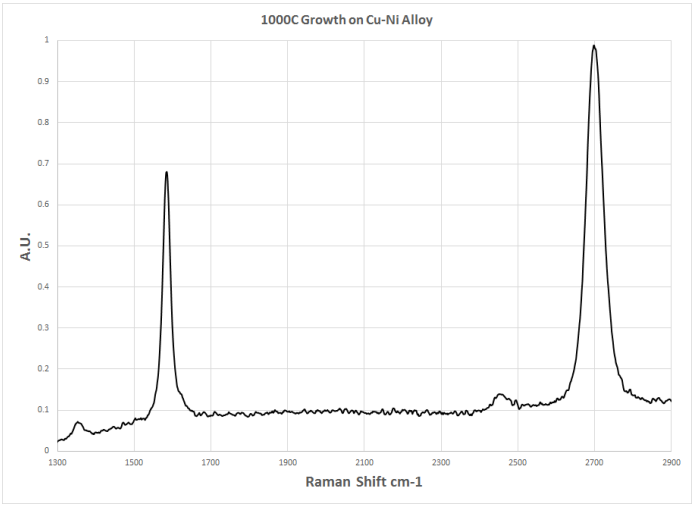

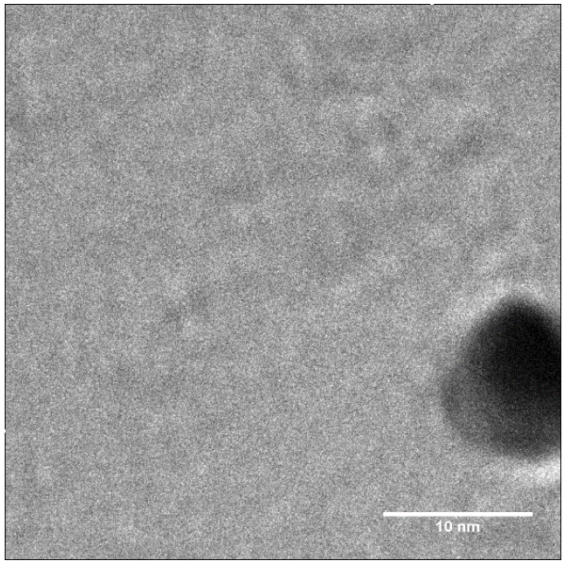

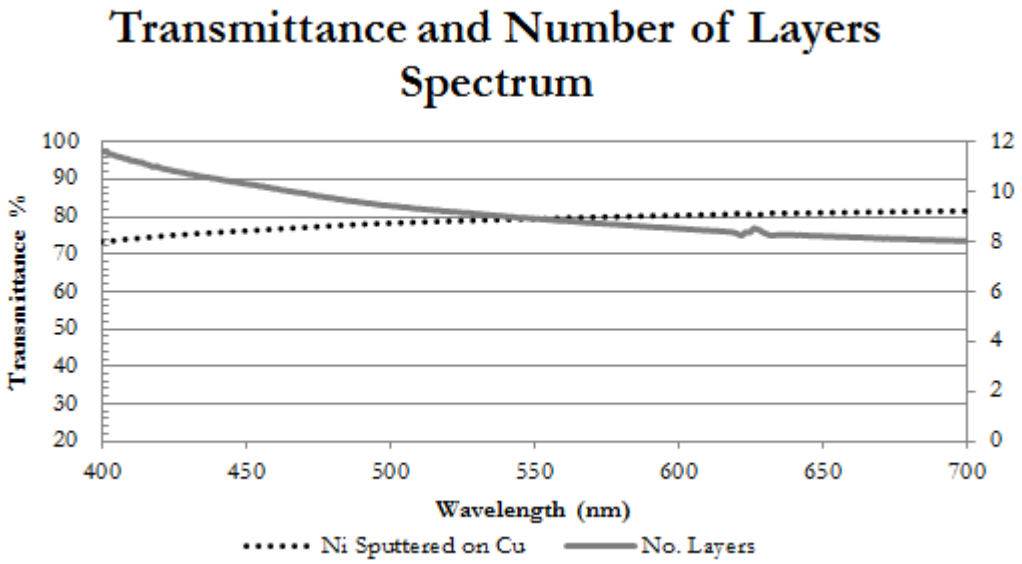

Figure 5.18 | Characterization of FLG derived from Cu-Ni alloy: a. Raman of transferred film grown on Cu-Ni alloy. **b** TEM of as prepared film. Scale is 10 nm. No intrinsic holes larger than 10 nm are observed. Object in picture is Ni debris left over from etching used for contrast. **c.** UV-Vis plot of transmittance vs. wavelength vs. number of graphene layers. The number of layers can be extrapolated and inferred as <10 on the right hand y-axis.

We prepared a handful of samples of Ni and Cu-Ni alloy and decided to run high pressure stirred cell tests to determine salt rejection. Our initial testes focused on the use of FLG prepared using Ni. The experimental set up is schematically drawn in Figure 5.19.

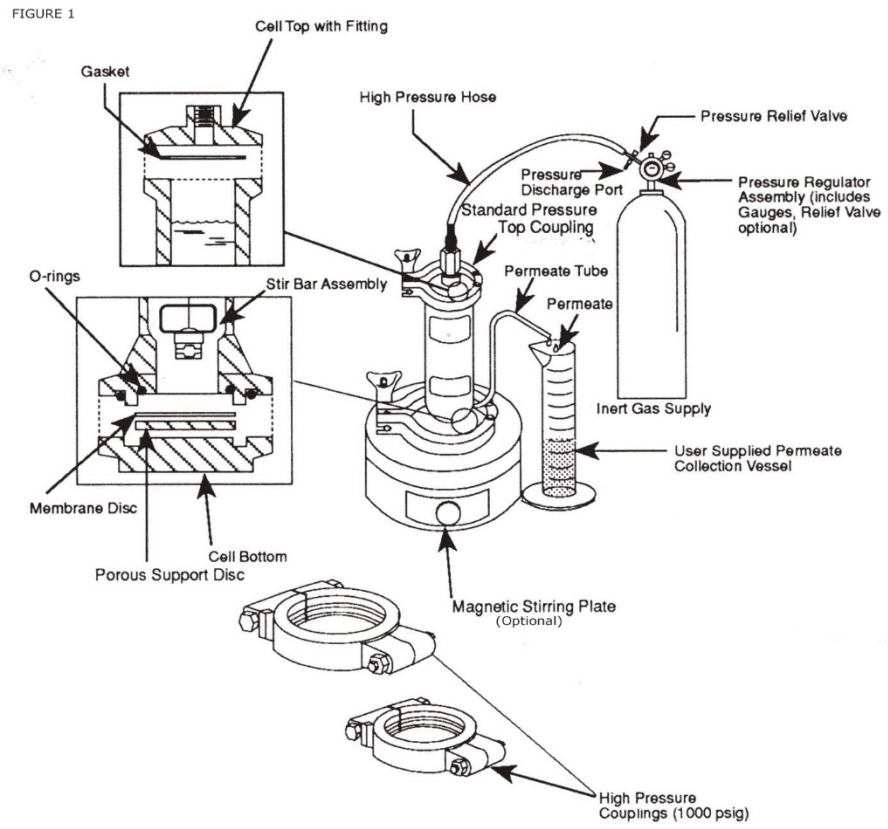

Figure 5.19 | Schematic of the testing cell for ion and molecular rejection.

We prepared 3.5% (35 g/L, or 599 mM) solutions of NaCl in deionized water and applied a pressure of 100 psi onto 0.1 μm pore PTFE track etched membranes coated with FLG. We found that initially, the permeate did not drip through even at pressures approaching 100 psi. Eventually the permeate began to collect and we took note of the flow rate and the ionic conductivity. The results indicated that the modified membranes had little salt rejection. We took the flow cell apart and examined the membrane and found pin sized holes had been created during the testing (Figure 5.20)

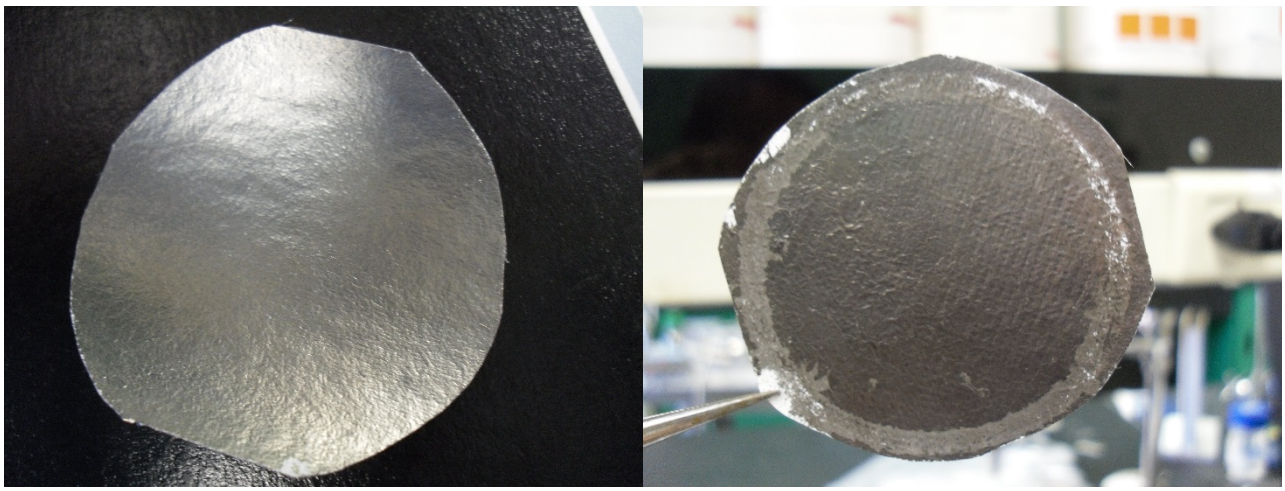

Figure 5.20 | FLG coated PTFE: a. Pre-test **b**. post-test.

During the testing, the membrane must be clamped down by an o-ring (the impression of which is clearly visible in Figure 5.20b) and this action may tear the graphene apart and provide an avenue for water and ions to flow through. The testing area itself is about 1" in diameter and has small micro tears caused by the filling of the flow cell with water. This is not a trivial act. Several prepared membranes experienced the same fate when we filled the chamber with water although the problem was alleviated by the use of hydrophobic surfaces as shown in Figure 5.21.

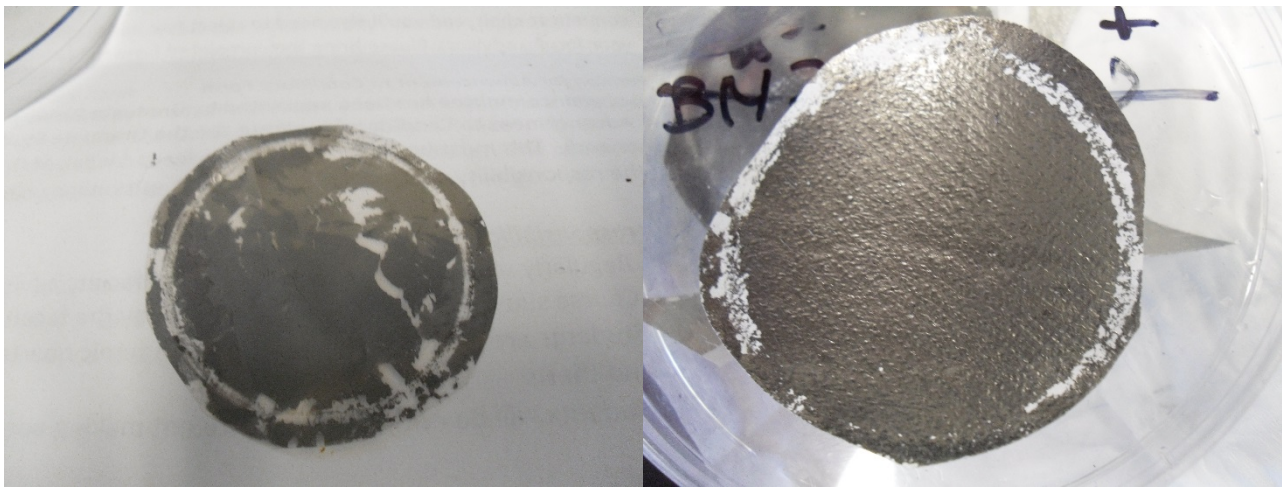

Figure 5.21 | Effect of membrane hydrophobicity on the delamination of FLG: a. FLG on hydrophobic polycarbonate membranes. During the loading of the test water, the sample began to delaminate. **b.** FLG on hydrophobic PTFE. The sample survived the initial water loading and high pressure testing. Notice the clamping of the o-ring causes mechanical delamination of the FLG.

The more hydrophobic the material, the better the graphene sticks to its surface and the less likely it is to delaminate. PTFE membranes fared better than hydrophobic PC membranes for the water loading, but if careful enough, both can be tested. However, if enough agitation takes place (for example scratching, or aiming a high pressure stream of concentrated water from a squirt bottle) then some FLG will delaminate. We next decided to use a sealant on the o-ring portion to prevent the possible leakage of ions around the graphene membrane. We turned to PMMA and coated the o-ring with a generous amount prior to sealing. We cured the PMMA using a heat gun for a few minutes then tested for NaCl rejection. Unfortunately, we detected no salt rejection at this time.

Ongoing work:

We are currently switching our focus from RO membranes to ultra- and nano-filtration applications. We have begun to optimize the etching of the Ni grown FLG as well as the Cu-Ni alloy grown version. We are using dilute 1:20 parts water to $FeCl_3$ and adding ethanol to ensure the best quality transfers. Similarly, we are using 1:20 parts water to APS etchant for the alloyed growth synthesis. The PFTE support membrane we use from Sterlitech has pores that are 100 nm in diameter—far too large to reject molecular species such bovine serum albumin, BSA (66 KDa, <10 nm in diameter). We need a sufficiently hydrophobic membrane surface for successful graphene transfer with small enough pores to possibly prevent any leakage of permeate around graphene. For this we turn to polyvinylidene fluoride (PVDF) membranes with pore sizes suitable for nanofiltration. We will next test for rejection of various molecular and salt species such BSA, lead (II) chloride, cesium chloride, potassium chloride and sodium chloride.

Ultimately, we would like to create defects into the graphene sheet itself. Several methods[27-31] have been shown to etch pores that increase with exposure time including the use of deep UV wavelengths, ozone bombardment, and ion bombardment using focused ion beam. We propose to achieve highly ordered, nanoporous films by etching the graphene with deep UV covered by a metal nanomesh mask. The mask can be prepared by the use of alumina oxide templates[37-41] as outlined in Figure 5.22.

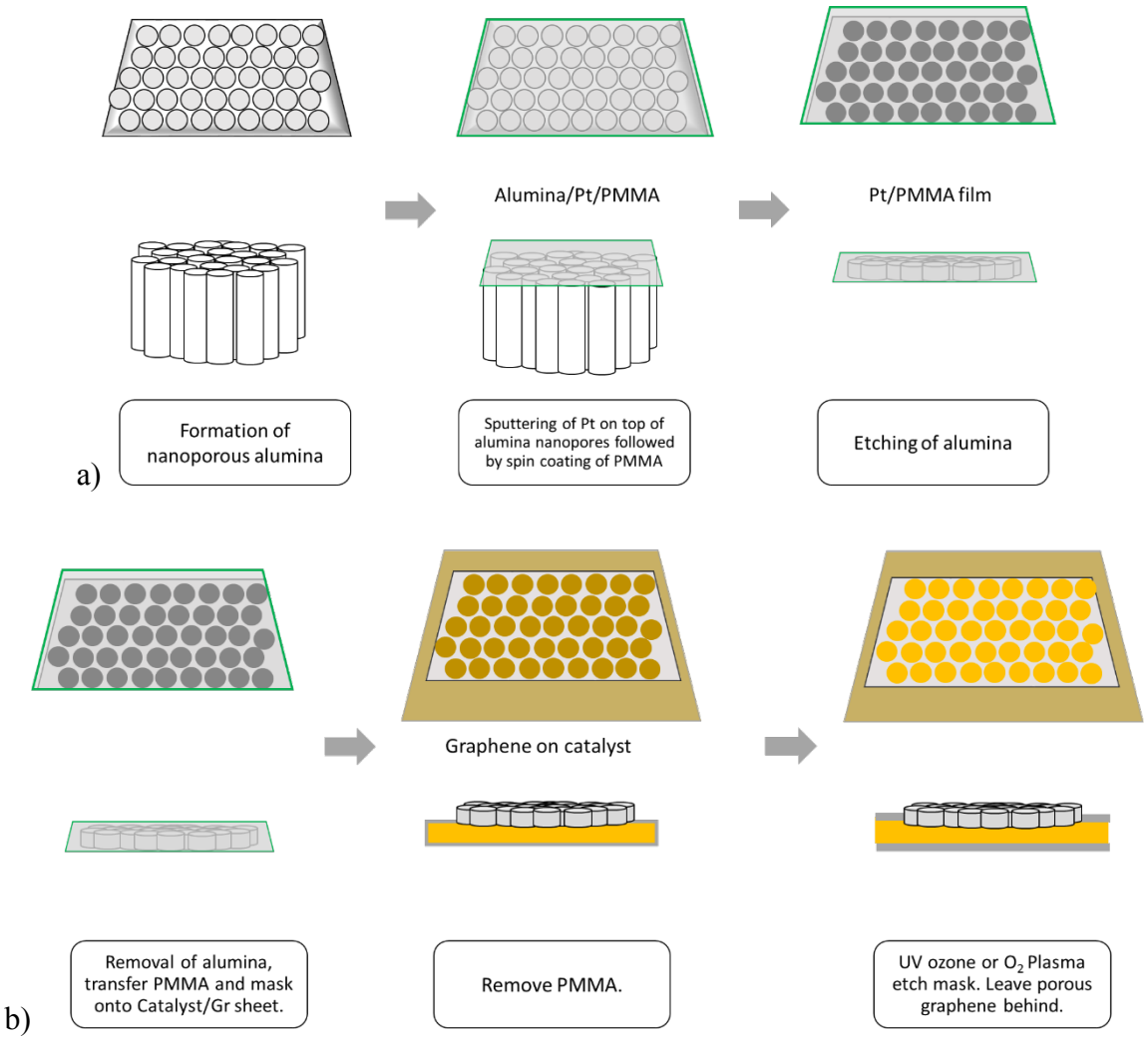

Figure 5.22 | Schematic for the controlled drilling of pores into FLG: a.Nanoporous alumina is synthesized then used as a template to fabricate a mask. **b.** The mask is used to etch graphene on catalyst using reactive oxygen species. The nanopore size can be controlled by the etch time.

References

1 Humplik, T., et al. "Nanostructured materials for water desalination." *Nanotechnology* **22**.29, 292001, doi:10.1088/0957-4484/22/29/292001 (2011)

2 Pendergast, MaryTheresa M., and Eric MV Hoek. "A review of water treatment membrane nanotechnologies." *Energy & Environmental Science* **4**.6, 1946-1971, doi: 10.1039/C0EE00541J (2011)

3 Rijsberman, Frank R. "Water scarcity: fact or fiction?." *Agricultural water management* **80**.1, 5-22, doi: 10.1016/j.agwat.2005.07.001 (2006)

4. Deen, W. M. Analysis of Transport Phenomena; Oxford University Press: New York, pg 597, (1998)

5 Suk, Myung E., and N. R. Aluru. "Water transport through ultrathin graphene." *The Journal of Physical Chemistry Letters* **1**.10, 1590-1594, doi: 10.1021/jz100240r, (2010)

6 Cohen-Tanugi, D.; Grossman, J. "Water Desalination across Nanoporous Graphene. "*Nano Lett.* **12**, 3602–3608, doi: 10.1021/nl301285 (2012)

7 Bunch, J.; Verbridge, S.; Alden, J.; van der Zande, A.; Parpia, J.; Craighead, H.; McEuen, P. "Impermeable Atomic Membranes from Graphene Sheets." *Nano Lett*. **8**, 2458–2462, doi: 10.1021/nl801457b (2008)

8 Jiang, D.; Cooper, V.; Dai, S. "Porous Graphene as the Ultimate Membrane for Gas Separation." *Nano Lett*. **9**, 4019–4024, doi: 10.1021/nl9021946 (2009)

9 Du, H.; Li, J.; Zhang, J.; Su, G.; Li, X.; Zhao, Y. "Separation of Hydrogen and Nitrogen Gases with Porous Graphene Membrane." *J. Phys. Chem. C* **115**, 23261-23266, doi: 10.1021/jp206258u (2011)

10 Nair, R.; Wu, H.; Jayaram, P.; Grigorieva, I.; Geim, A. "Unimpeded Permeation of Water Through Helium-Leak-Tight Graphene-Based Membranes." *Science* **335**, 442–444, doi: 10.1126/science.1211694 (2012)

11 Lee, Changgu, et al. "Measurement of the elastic properties and intrinsic strength of monolayer graphene." science 321.5887, 385-388, doi: 10.1126/science.1157996 (2008)

12 Meyer, Jannik C., et al. "The structure of suspended graphene sheets." *Nature* **446**.7131, 60-63 doi:10.1038/nature05545 (2007)

13 Garaj, Slaven, et al. "Graphene as a subnanometre trans-electrode membrane." *Nature* **467**.7312, 190-193, doi:10.1038/nature09379 (2010)

14 Meyer, Jannik C., et al. "Direct imaging of lattice atoms and topological defects in graphene membranes." *Nano letters* **8**.11, 3582-3586, doi: 10.1021/nl801386m (2008)

15 Booth, Tim J., et al. "Macroscopic graphene membranes and their extraordinary stiffness." *Nano letters* **8**.8, 2442-2446, doi: 10.1021/nl801412y (2008)

16 Meyer, J. C., et al. "On the roughness of single-and bi-layer graphene membranes." *Solid State Communications* **143**.1,101-109, doi: 10.1016/j.ssc.2007.02.047 (2007)

17 Koenig, Steven P., et al. "Ultrastrong adhesion of graphene membranes." *Nature nanotechnology* **6**.9, 543-546, doi:10.1038/nnano.2011.123 (2011)

18 Huang, Pinshane Y., et al. "Grains and grain boundaries in single-layer graphene atomic patchwork quilts." *Nature* **469**.7330, 389-392, doi:10.1038/nature09718 (2011)

19 Schrier, Joshua. "Helium separation using porous graphene membranes." *The Journal of Physical Chemistry Letters* **1**.15, 2284-2287, doi: 10.1021/jz100748x (2010)

20 Hauser, Andreas W., and Peter Schwerdtfeger. "Nanoporous graphene membranes for efficient 3He/4He separation." *The Journal of Physical Chemistry Letters* **3**.2, 209-213, doi: 10.1021/jz201504k (2012)

21 O'Hern, Sean C., et al. "Selective Ionic Transport through Tunable Subnanometer Pores in Single-Layer Graphene Membranes." *Nano letters* **14**.3, 1234-1241, doi: 10.1021/nl404118f (2014)

22 O'Hern, Sean C., et al. "Selective molecular transport through intrinsic defects in a single layer of CVD graphene." *ACS nano* **6**.11, 10130-10138, doi: 10.1021/nn303869m (2012)

23 Celebi, Kemal, et al. "Ultimate Permeation Across Atomically Thin Porous Graphene." *Science* **344**.6181, 289-292, doi: 10.1126/science.1249097 (2014)

24 Boutilier, Michael SH, et al. "Implications of Permeation through Intrinsic Defects in Graphene on the Design of Defect-Tolerant Membranes for Gas Separation." *ACS nano* **8.**1, 841-849, doi: 10.1021/nn405537u (2014)

25 Schneider, Grégory F., et al. "DNA translocation through graphene nanopores." *Nano letters* **10**.8, 3163-3167, doi: 10.1021/nl101046t (2010)

26 Pereira, Vitor M., et al. "Geometry, mechanics, and electronics of singular structures and wrinkles in graphene. *Phys. Rev. Lett.* **105**, 156603, doi: http://dx.doi.org/10.1103/PhysRevLett.105.156603 (2010)

27 Morin, A., et al. "FIB carving of nanopores into suspended graphene films." *Microelectronic Engineering* **97**, 311-316, doi: 10.1016/j.mee.2012.02.02 (2012)

28 Kim, Myungwoong, et al. "Fabrication and characterization of large-area, semiconducting nanoperforated graphene materials." *Nano letters* **10**.4, 1125-1131, doi: 10.1021/nl9032318 (2010)

29 Ozeki, Shun-ei, et al. "Scanning tunneling microscopy of UV-induced gasification reaction on highly oriented pyrolytic graphite." *Japanese journal of applied physics* **35**.6S, 3772, doi: (1996)

30 Yamada, Yasuhiro, et al. "Subnanometer Vacancy Defects Introduced on Graphene by Oxygen Gas." *Journal of the American Chemical Society* **136**.6, 2232-2235, doi: dx.doi.org/10.1021/ja4117268 (2014)

31 Liu, Li, et al. "Graphene oxidation: thickness-dependent etching and strong chemical doping." *Nano letters* **8**.7, 1965-1970, doi: 10.1021/nl0808684 (2008)

32 Li, Xuesong, et al. "Large-area synthesis of high-quality and uniform graphene films on copper foils." *Science* **324**.5932, 1312-1314, doi: 10.1126/science.1171245 (2009)

33 Reina, Alfonso, et al. "Large area, few-layer graphene films on arbitrary substrates by chemical vapor deposition." *Nano letters* **9**.1, 30-35, doi: 10.1021/nl801827 (2008)

34 Chen, Shanshan, et al. "Synthesis and characterization of large-area graphene and graphite films on commercial Cu–Ni alloy foils." *Nano letters* **11**.9, 3519-3525, doi:.10.1021/nl201699j (2011)

35 Childres, Isaac, et al. "Raman spectroscopy of graphene and related materials." Developments in photon and materials research: 978-1.

36 Liu, Wei, et al. "Controllable and Rapid Synthesis of High-Quality and Large-Area Bernal Stacked Bilayer Graphene using Chemical Vapor Deposition." *Chemistry of Materials* **26**.2, 907-915, dx.doi.org/10.1021/cm4021854 (2013)

37 Li, Yanbo, et al. "Fabrication of highly ordered nanoporous alumina films by stable high-field anodization." *Nanotechnology* **17**.20, 5101, doi:10.1088/0957-4484/17/20/010 (2006).

38 Sousa, C. T., et al. "Nanoporous alumina as templates for multifunctional applications." *Applied Physics Reviews* **1**.3, 031102, doi: 10.1063/1.4893546 (2014)

39 Wang, Min, et al. "CVD growth of large area smooth-edged graphene nanomesh by nanosphere lithography." *Scientific reports* **3** doi:10.1038/srep01238 (2013)

40 Akhavan, Omid. "Graphene nanomesh by ZnO nanorod photocatalysts." *Acs Nano* **4**.7, 4174-4180, doi:10.1021/nn1007429 (2010)

41 Ning, Guoqing, et al. "Gram-scale synthesis of nanomesh graphene with high surface area and its application in supercapacitor electrodes." *Chem. Commun*. **47**.21, 5976-5978, doi:10.1039/C1CC11159K (2011)

Chapter 6: Future Directions

Chemical vapor deposition (CVD) is a powerful tool for the synthesis of high quality graphene thin films, but the scalability of CVD to mass produce graphene is limited and cost prohibitive. Solution processing of high quality graphene or graphene derivatives would open the door to a variety of plant scale technologies for brackish water treatment and composite material mass production. Chemical processing of large batches of graphite into graphene will lead to form single and few layer graphene dispersed solutions suitable for use in capacitive deionization water filtration and graphene containing composites.

Improved synthesis of graphene oxide by the selective oxidation of edges

The mass production of single or few layer graphene sheets for use in electronics or composites is a widely studied field. Many promising exfoliation methods of graphite[1-6] have been devised including sonication assisted intercalation in various organic solvents and oxidation of graphite into graphene oxide (GO) by harsh oxidation. The latter can be reduced back into graphitic like compounds albeit with reduced electronic properties.[7] Selective modification of the edges of graphite may confer limited polar solubility to graphite and allow for exfoliation into single and few layer sheets. Further modification may take place to tailor the solubility in a variety of solvents.

Selective edge modification to make edge oxidized graphite (EOG) may take place using a mildly alkaline solution of periodate containing permanganate. This reaction was first described by Lemieux and Bauer[9] where it was discovered that olefinic double bonds are readily oxidized in an aqueous solution of periodate which contains only catalytic amounts of permanganate.

The olefin edges of graphene are far more reactive than the double bonds found in the basal plane[10]. This is due to the presence of both sp^2 and sp^3 bonds at the edges, where under the right conditions, the sp^3 carbons can be activated for chemical reactions (Figure 6.1).

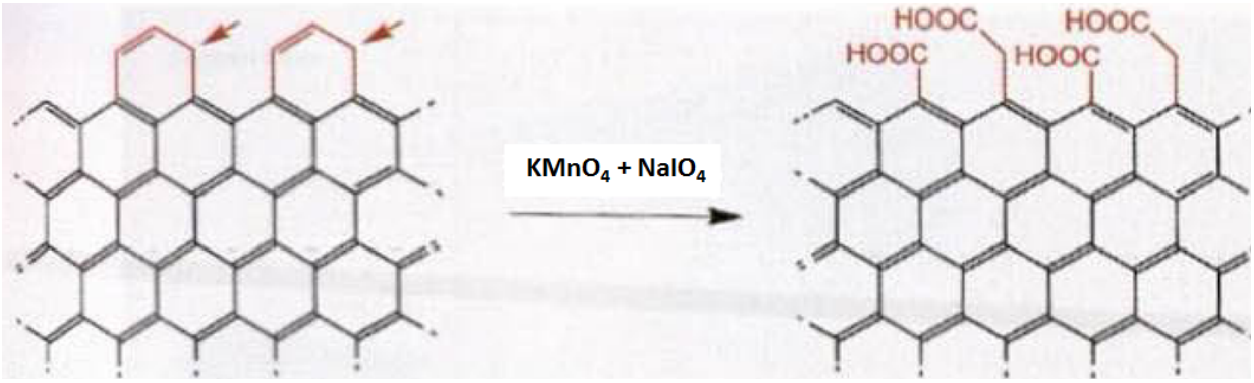

Figure 6.1 | Schematic of edge sp^2 and sp^3 carbons on graphene: A catalytic amount of $KMnO_4$ in mildly basic conditions will selectively oxidize the edges of graphene. (reprinted with permission[11] © 2000- American Scientific Publishers.)

Yang et al. recently demonstrated that indeed graphite and graphene edges can be selectively modified using periodate and permanganate[11]. TGA was utilized to characterize the amount of oxidation that had occurred with prolonged reactivity (Figure 6.2).

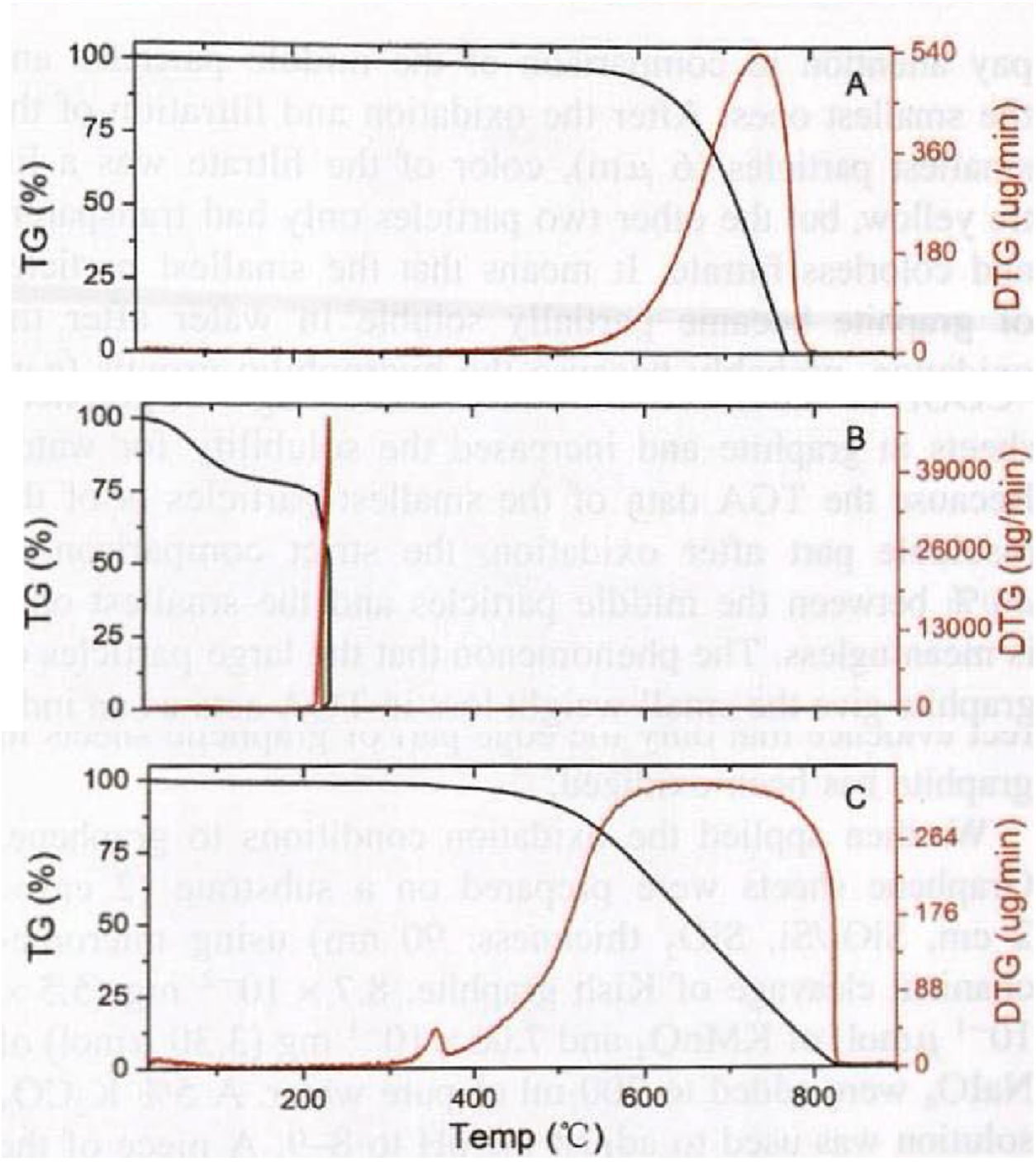

Figure 6.2 | Thermogravimetric (TGA) analysis (10 °C/min heating rate) of oxidation loss of: a. as received graphite, **b.** graphite oxide prepared by Hummer's method, **c.** edge oxidize (EOG) graphite. (reprinted with permission[11] © 2000- American Scientific Publishers.).

Weight loss due to thermal decomposition in the graphite (Figure 6.2a) does not occur until 600 °C and continues past 800 °C. The GO prepared by Hummer's method shows rapid weight loss beginning at 250 °C (Figure 6.2b), most likely due to its highly oxidized nature. The EOG experiences weight loss at 500 °C until it ceases at 820 °C. The high thermal stability is indicative of the intact π-conjugated network of the graphite as seen in the unmodified graphite.

Wei et al.[12] used a modified Hummer's approach that utilized considerably less $KMnO_4$ at relatively high temperature (60 °C) in order to edge oxidize graphite flakes. The functionalized edges permitted long-chain tetradecyl-ammonium salt ($C_{14}N^+$) to be spontaneously intercalated into EOG to form intercalated EOG-$C_{14}N^+$ compounds. Gentle and short-time sonication of EOG-$C_{14}N^+$ in toluene was shown to fully exfoliate EOG into edge-oxidized graphene nanosheets (EOGNs) with concentration of 0.67 mg/ml, monolayer populations up to 90% and lateral sizes ranging from 1 μm to >100 μm (Figure 6.3).

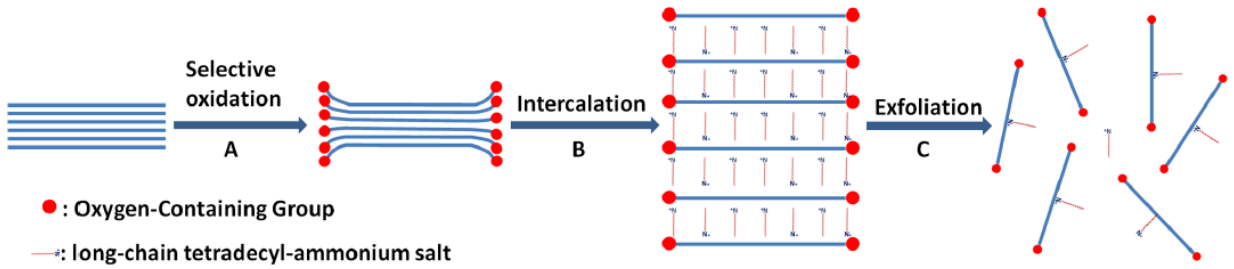

Figure 6.3 | Selective oxidation, intercalation, and exfoliation of graphite into EOG sheets. (reprinted with permission[12] © Nature Publishing Group).

Spectral analysis using FTIR (Figure 6.4) compares GO to the EOG and reveals considerably less intense oxygen group peaks. For comparison graphite is included to demonstrate slight oxidation to the EOG. The XRD powder diffraction patterns for graphite, GO, EOG, and EOG-$C^{14}N^+$ are compared. For pristine graphite, a sharp [002] peak at 26.5° corresponds to an ideal

layered-structure with d-spacing of 0.335 nm. This [002] peak was significantly shifted from 26.5° to 10.8°, corresponding to an interlayer distance increase from 0.335 to 0.818 nm for GO perhaps due to uptake of water in the hydrophilic molecule. The EOG sample slightly shifted to 25.4° indicating a d-spacing close to that of pristine graphite. This indicates that the basal plane itself is not modified as it is in GO. Further characterization took place with Raman, which reveals the presence of a pronounced D-peak at 1338 cm^{-1} in heavily oxidized GO. This peak represents edge distortion and structural defects and is not present in pristine graphite. The more intense this peak, the more defects exists in the sample. The emergence of a slight D-peak for EOG provides evidence of slight oxidation.

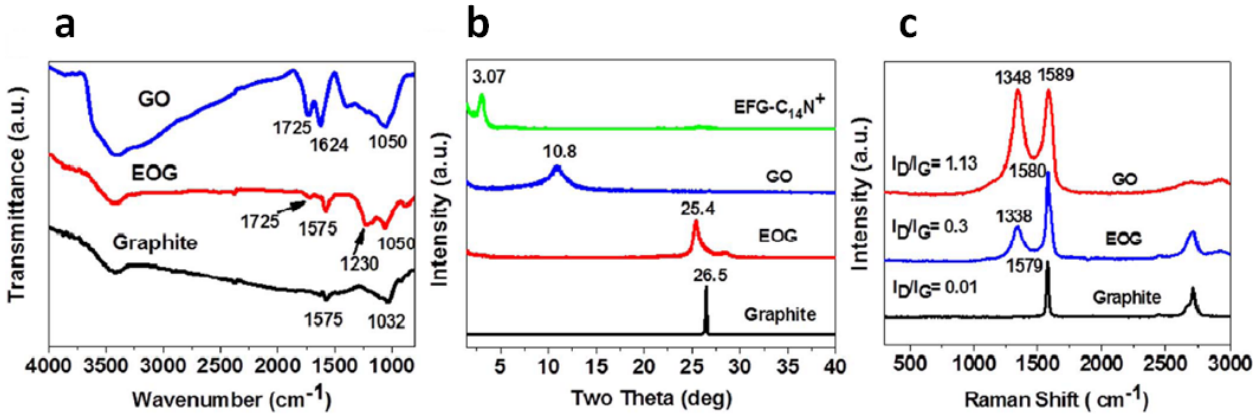

Figure 6.4 | Characterization of as prepared EOG: GO = graphite oxide, EOG = edge oxidized graphite. a. FTIR of pristine graphite, EOG and GO. **b.** XRD of pristine graphite, EOG, GO and EOG-$C_{14}N^+$ intercalated compound. **c.** Raman spectra of pristine graphite, EOG and GO. (reprinted with permission[12] © Nature Publishing Group)

Further Raman studies were conducted to search for differences in oxidation on the basal plane vs the edges (Figure 6.5). As expected, the Raman for pristine graphite did not change from basal plane to edge. Similarly for GO, the edge and basal Raman spectra appeared roughly the same, testament to the highly oxidized nature of the GO. The EOG showed basal plane Raman similar

to the parent pristine graphite and but clearly oxidized edges. Heat treatment reduces the EOG back to graphite.

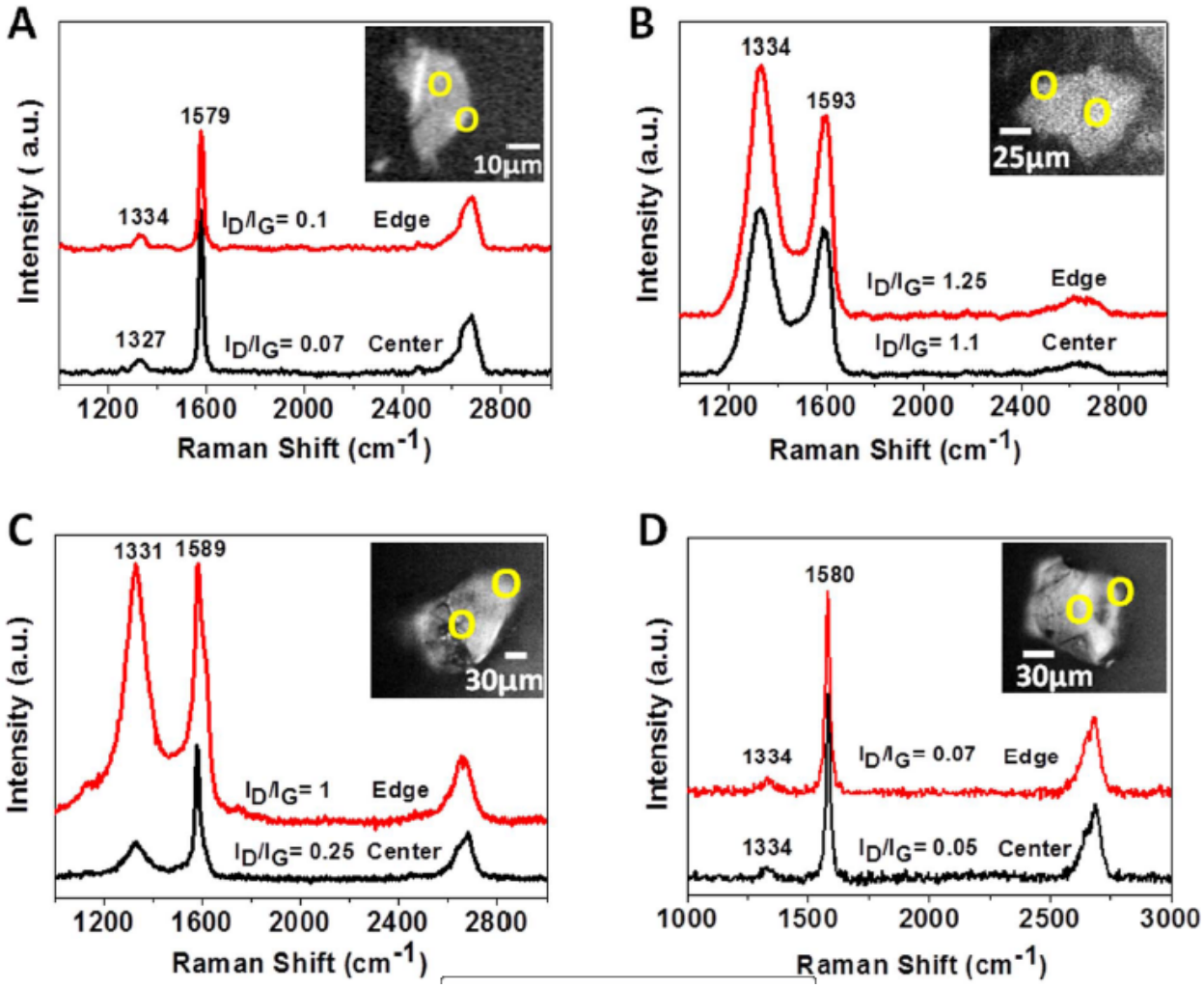

Figure 6.5 | Micro Raman spectra of basal and edges of pristine graphite, GO, and EOG samples: GO = graphite oxide, EOG = edge oxidized graphite. Red indicates the edges, black the basal plane. a. Raman of pristine graphite, **b.** Raman of GO, **c.** Raman of EOG before annealing, **d**. After annealing. (reprinted with permission[12] © Nature Publishing Group)

Intercalation only occurred in the oxidized samples. Pristine graphite had no reaction with the long chain ammonium salts. Figure 6.6 demonstrates the dispersibility of the EOG-$C_{14}N^+$ in various solvents of increasing polarity from left to right.

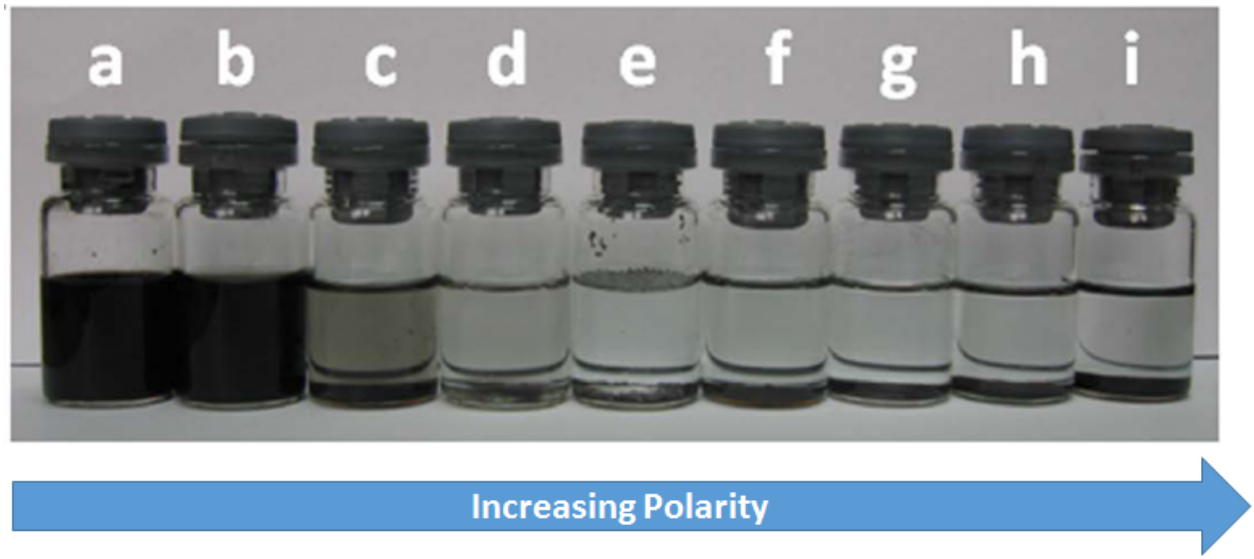

Figure 6.6 | Photographs of EOG dispersion after sonication of EOG-$C_{14}N^{+}$: a. Toluene, **b.** Benzene, **c.** NMP, **d.** DMF, **e.** DMSO, **f.** ethanol, **g.** methanol, **h.** water, **i.** acetone. (reprinted with permission[12] © Nature Publishing Group).

The authors noted that stable dispersions of EOG intercalated with long chain ammonium salts could only be made in non-polar solvents due to the hydrophobic nature of the basal plane. Any attempt to disperse the EOG-ammonium salt compound into polar solvents caused the material to instantly crash out. There are a variety of ways to modify oxidized graphene and graphite compounds[13]. Grafting of water soluble complexes can be achieved by utilizing condensation reactions[14]. Recall a condensation reaction is a chemical reaction in which two molecules (functional groups) combine to form one single molecule with a loss of entropy. In the case of graphene, condensation occurs with isocyanate, diisocyanate, and amine compounds through the formation of amides and carbamate ester linkages. It is conceivable to use amine terminated poly(ethylene glycol) (PEG-NH_2) to increase the solubility of the EOG (Figure 6.7).

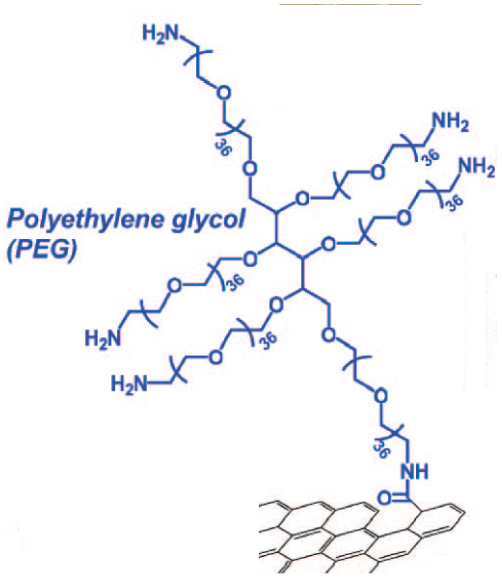

Figure 6.7 | EOG can be conceivably modified using water soluble groups such as amine terminated poly(ethylene glycol). (reprinted with permission[14] © Journal of American Chemical Society).

Carboxyl-reactive chemical groups found in EOG can be cross-linked to primary amines including the carbodiimide compounds EDC and DCC (Figure 6.8). The choice of crosslinking agent depends on whether one uses a polar or non-polar solvents which is advantageous. The crosslinking agents can then be replaced upon further reaction with groups that confer more solubility including –sulfo (SO_3^-) groups. High temperature annealing may be used to remove the water soluble groups.

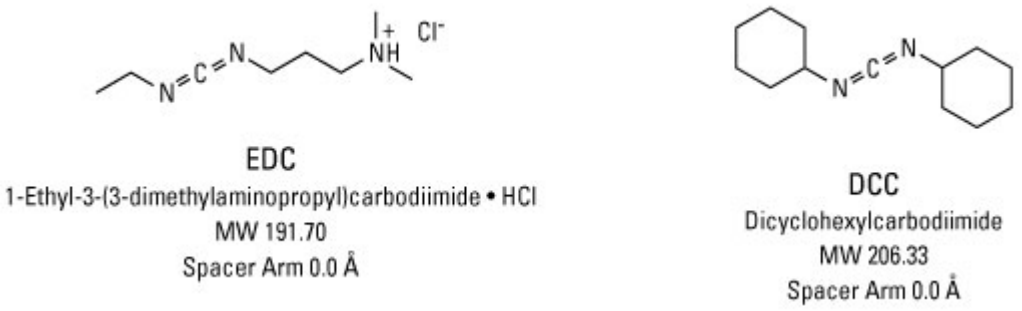

Figure 6.8 | Coupling agents used for modification of carbonyl terminated molecules.

The ability to tailor the solubility could be important for applications such, transparent conductors, conducting inks, or in making composites to increase the mechanical and thermal properties of engineered materials.

Capacitive deionization of brackish and salt water:

Previously, we explored the use of graphene as a membrane barrier for water filtration due to its predicted increase in flux. Beyond the traditional size exclusion technologies to purify water, there also exists an electrochemical method to separate ions from water (Figure 6.9). Capacitive deionization (CDI) functions by removing ions from brackish or salt water by flowing water between two electrodes under an applied field. Typically the electrodes are porous carbon and the applied field is 1.2 V. Compared to reverse osmosis and distillation, CDI is considered to be an energy-efficient technology for brackish water desalination. This is mainly because CDI removes the salt ions from the water, while the other technologies extract the water from the salt solution.

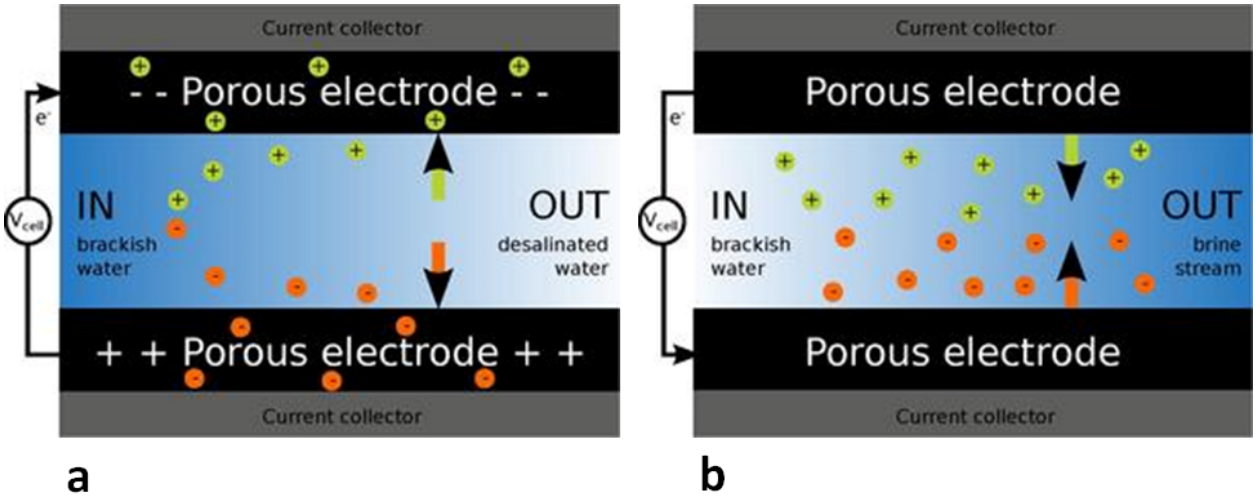

Figure 6.9 | Schematic of the capacitive deionization (CDI) process: a. Adsorption phase. Brackish water is fed into a channel containing two electrodes under a potential difference to absorb the ions in solution. **b.** Desorption phase. Adsorbed ions are released into a brine stream of water to regenerate the electrodes.

During CDI, brackish or salt water is fed into a channel between two carbon electrodes under a 1.2 V applied field, this is the adsorption phase (Figure 6.9a). The ions are attracted to the electrodes based on their respective charge and saturate the electrode. Operation continues until a point is reached when the electrodes can no longer take in any more charged species. Here, at the desorption phase, they must be discharged for continued operation (Figure 6.9b). The original stream of brackish/saltwater is turned off and a new stream of water is allowed to flow in. The potential difference between electrodes is reversed or reduced to zero and the electrodes discharge the collected salts into this stream. This brine stream is then turned off, the electrodes flushed with water, and then the brackish/saltwater stream is flowed once again. Part of the energy input required during the adsorption phase can be recovered during this desorption step.

The choice of electrode materials increases the performance of CDI:

High performance of a CDI cell hinges on the selection of high quality electrode materials. For a very long time, activated carbon has been the choice for the porous electrode material, although a great deal of research has been done on a variety of other carbon materials, including templated carbons, carbon aerogels, and carbon nanotubes for CDI[20]. Ideal electrode materials should meet the following criteria: Have high salt electrosorption capacity, large specific surface area and pore size distribution of the electrode material to accommodate ion accessibility, stability and not undergo chemical degradation in the voltage window applied for CDI. Additionally, the ions should be able to move quickly through the pore network of the electrode and the conductivity of the electrode material should be high. Lastly, the costs of the electrode materials are important to take into consideration and they would ideally be inexpensive. In light of these conditions, it makes perfect sense to utilize reduced graphene oxide as a low-cost, large specific area, highly

conductive material for CDI electrodes. Already GO and r-GO have proven capable for use as state-of-the-art capacitive storage media[16-18].

Flow electrode design CDI has superior performance:

Flow cells for CDI have traditionally utilized a single batch mode (i.e. a finite amount of brackish or saltwater is treated before the CDI cell must be regenerated), but the constant interruption in fresh water production is not at all desired. This is a consequence of utilizing static carbon electrodes that become saturated and must be regenerated for continued performance. An alternative to the traditional CDI is the emergence of continuous flow electrode capacitive deionization (FCDI), a process where desalination of water, brine production and regeneration of electrodes are all performed continuously. Comparison of the two reveals that for activated carbon electrode material, the maximum salt adsorption capacity (SAC — weight of adsorbed ions per dry weight of adsorbent) is 14.3 mg/g for batch vs. 40 mg/g for continuous flow.[20, 21] Recently, Gendel et al. proposed the use of an FCDI[19] comprised of a system of two FCDI modules: one module for water desalination and another for the regeneration of slurry electrodes (Figure 6.10). The latter also functions as a concentrator next to slurry regeneration. The feed water is split between two modules into dilute and concentrate streams. Flowing carbon electrodes are circulated continuously between two modules, while a reverse potential is applied to the second module to desorb ions from charged slurries into the concentrate water channel. The design allows for truly continuous operation.

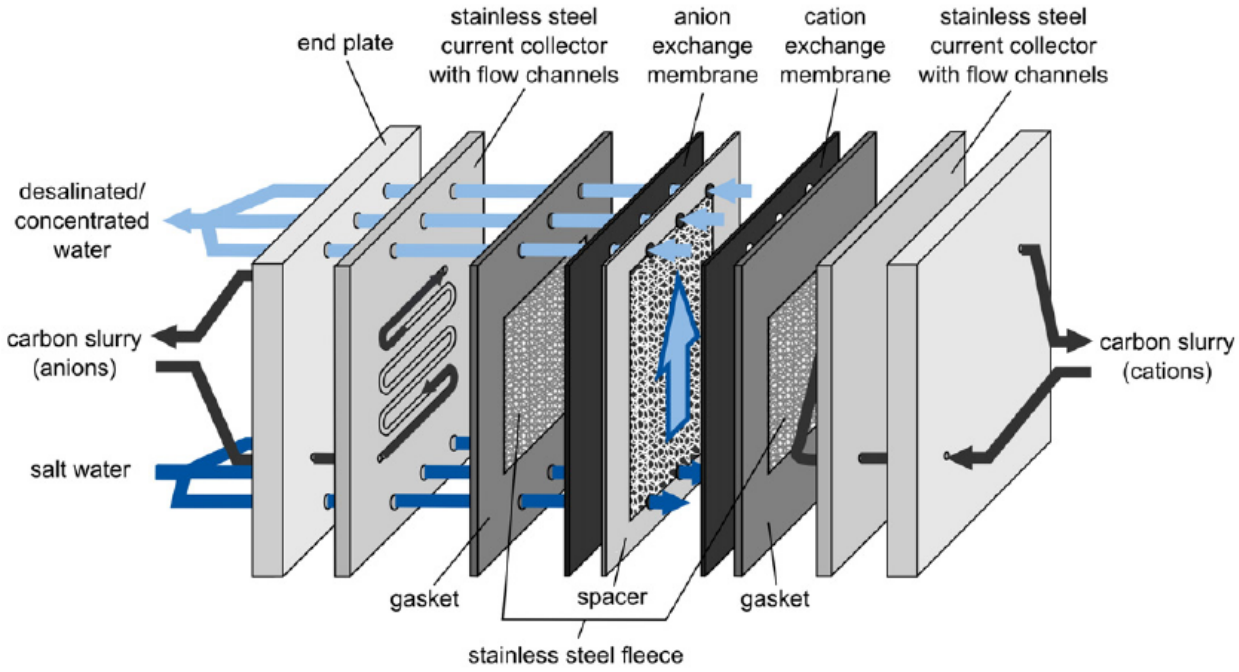

Figure 6.10 | Schematic of the flowing electrode capacitive deionization (FCDI) cell: A 5% w/w dispersion of activated carbon powder in distilled water is used as the electrode material. NaCl solutions pass through the 0.5 mm thick spacer located between the ion exchange membranes. A constant voltage of 1.2 V is supplied during operation. (reprinted with permission[19] © Elsevier).

Batch mode testing was done using slurry electrodes (50 ml each) that were recirculated between the FCDI module and two stirred vessels using peristaltic pumps at the flow rate of 60 ml/min (Figure 6.11a). NaCl solution was recirculated between the FCDI cell and the third stirred vessel at a constant flow rate of 9 ml/min. Electrical conductivity (EC) of the NaCl solution was monitored during each experiment using a pH/conductivity meter.

Continuous flow experiments were performed (Figure 6.11b) where the flowing electrodes (100 ml each) were recirculated (250 ml/min) between two stirred vessels and the FCDI modules. Feed water (1 g NaCl/l) was split between two FCDI modules at 50/50, 70/30 and 90/10 diluate/concentrate flow rate ratios. For each split ratio several tests were performed

for different flow rates of the diluate stream: 0.7, 1, 2.5, 5, 7.5, 10 and 15 ml/min which correspond to 48.6, 69.4, 173.6, 347.2, 520.8, 694.4 and 1041.7 ml/min/m^2 water flow rates per the water channel surface area ratios, respectively.

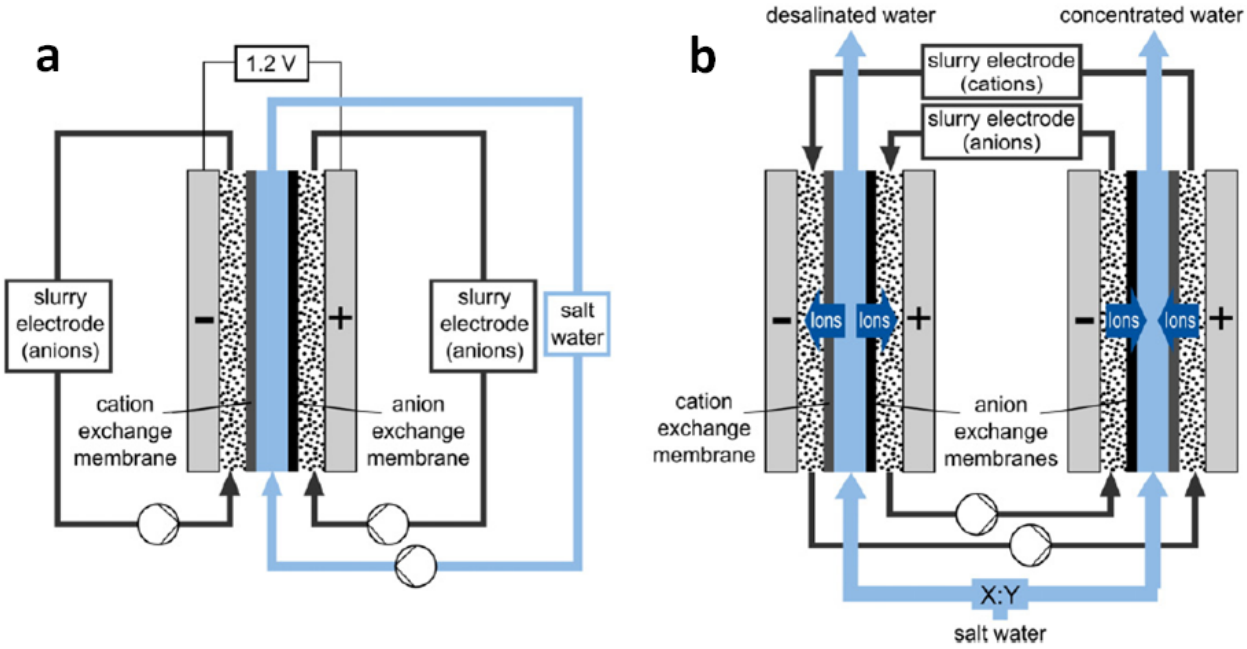

Figure 6.11 | Schematic of the flowing electrode capacitive deionization (FCDI) process: a. Batch mode. **b.** Continuous flow mode. (reprinted with permission[19] © Elsevier).

The authors claim an SAC of 260 mg/g can be estimated for the activated carbon slurry electrodes within the batch-mode FCDI experiments and the continuous water desalination experiments had desalination rates of more than 99% for the recoveries as high as

90% (1 g NaCl/l in the feed water). These results are promising and can be made better by the use of graphene. Reduced GO can be made porous with specific surface area (SSA) from 200 to higher than 1200 m^2 g^{-1}. [22] Previous work[23] has demonstrated that graphene oxide-based materials can have well-defined nanometer pores and can exhibit low frictional water flow inside them, making their properties of interest for filtration and separation. Additionally, RGO has

been shown to make excellent composite materials with CNTs[24], conducting polymers[27], and inorganic salts and metals[25,26]. Any of these composite materials will improve the conductivity of the flowing electrode and gives us the flexibility to try a variety of systems for marked increases in desalination.

High packing density sheaths of graphite oxide composites with a low density core for improved specific elastic modulus.

Graphene and graphene-derivatives have attracted vasts amount of curiosity because of graphene's excellent mechanical and thermal properties. However, making functional composites of graphene requires a way to translate its unique nano-properties to the macro-scale. Within the past few years, liquid crystalline (LC) behavior of graphene oxide (GO) dispersions in various organic and aqueous media has been widely studied. The LC behavior brings added control to the assembly of larger structures using the chemical process approach to the industrial scale production of graphene[30]. The LC state can be used to direct the ordered assembly of nanocomponents in macroscopic structures via simple methods like wet-spinning. The Wallace group has successfully synthesized liquid crystalline dispersions of graphite oxide (LCGO)[28]. The fine-tuning of the LCGO dispersion properties offers rational control over the formation and processability of the final properties of the graphene. Consequently, scalable one-step wet-spinning of the graphene fibers and yarns was achieved (Figure 6.12) at practical concentrations as low as 0.75 wt% (the lowest ever reported value for spinning of any type of colloidal solutions). Furthermore, the Wallace group has demonstrated that hybrid materials can be synthesized by utilizing GO's amphiphillic ability to disperse in both water and a wide range of organic solvents to aid in the dispersion and organization of hydrophobic materials such as single walled carbon nanotubes (SWCNTs)[29]. Additionally, not only are the SWNTs dispersed in water,

but the π-π interactions between the GO sheets and SWNTs aid in their alignment resulting in excellent mechanical properties. Self-assembled layer-by-layer multifunctional architectures of LC GO-SWNTs have been formed by cast drying as shown in Figure 6.13.

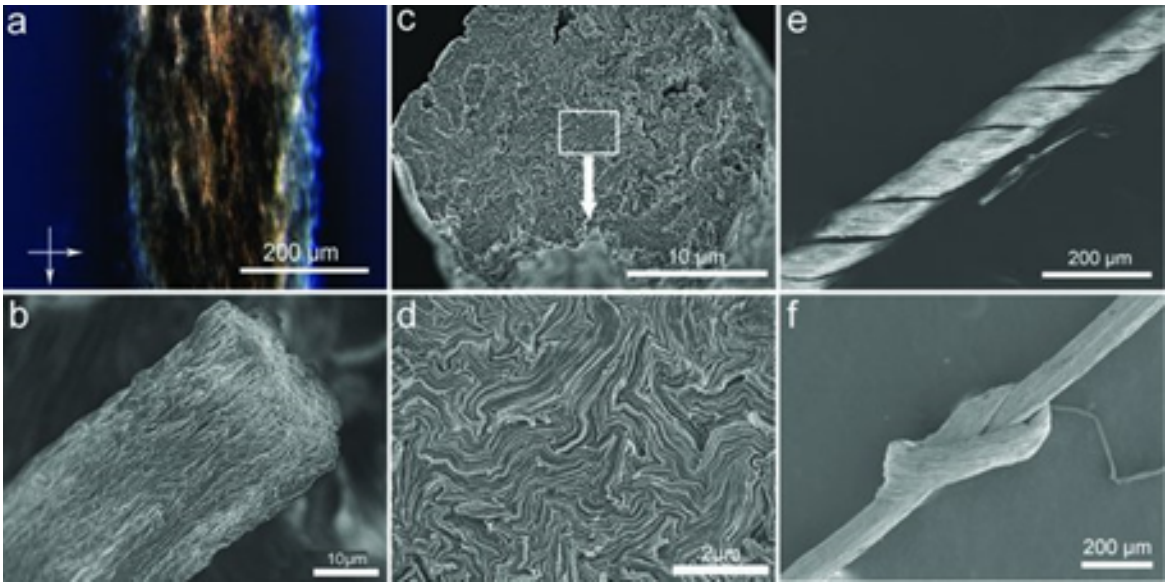

Figure 6.12 | Images of as-spun GO Fibers: a. Polarized optical microscopy image of as-spun gel state GO fiber. **b.** SEM images of an as-spun GO fiber and its corrugated surface. **c.** Near-circular cross-section. **d.** Close-up SEM image of the cross-section of GO fiber shown in b revealing GO sheet planes that are oriented along the fiber axis. **e.** SEM images of crumpled and **f.** knotted rGO yarns (reduced by annealing) showing their flexibility. (reprinted with permission[28] ©2014 WILEY-VCH Verlag GmbH & Co. KGaA, Weinheim).

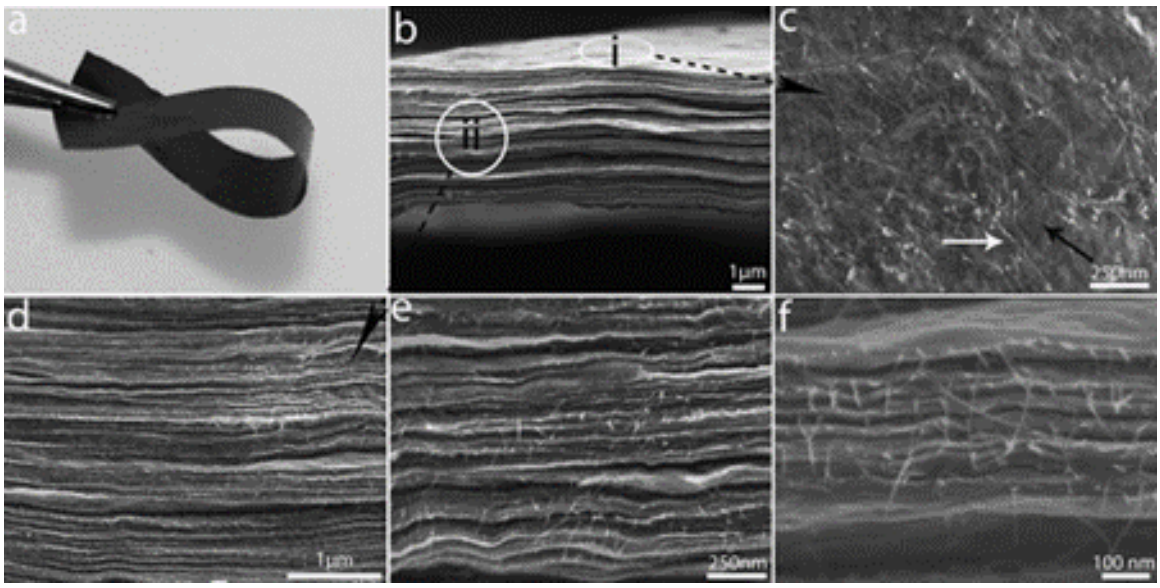

Figure 6.13 | Schematic of the flowing electrode capacitive deionization (FCDI) process a. a flexible free-standing paper of LC GO-SWNT made by cast drying method. **b.** SEM image of the cross section of as-cast dried LC GO-SWNT paper. **c.** SEM image of the surface of the layer-by-layer composite, which is marked as region (i) in **b**. Some of the SWNTs are laid on the surface of the paper (white arrow), while others are placed between layers of GO sheets (black arrow). Transparency of the monolayer/few layers of GO sheets allows observing tube sites in different layers. **d–f**. Cross section of composite paper at different magnifications (marked as (ii) in **b.** confirmed the self-oriented nature of the composite as well as maintaining SWNTs debundled after the fabrication of composite. (reprinted with permission[28] ©2014 WILEY-VCH Verlag GmbH & Co. KGaA, Weinheim).

Carbon nanotube yarns are an excellent analog to LCGO fibers. Both are low dimensional carbons with excellent mechanical and thermal properties and both can be aligned with shear forces to make directional fibers[31-36]. The load transfer between carbon nanotubes in a yarn mainly relies on the van der Waals force between the constituent nanotubes. To maximize carbon nanotube interconnections, all the constituent carbon nanotubes in the yarn need to lie parallel and close with each other so that line contacts between them can be formed. This may be achieved using LCGO shear flow wet spinning. Recently, a new mechanical method[37] to produce a highly densified, twistless CNT yarn has been developed, in which the CNTs are substantially straight and parallel with each other and are aligned in the direction of the yarn axis. Most

interesting is this new CNT yarn has a unique structure consisting of a high packing density sheath and a low density core and has shown similar tensile strength but significantly improved elastic modulus in comparison with twist-densified carbon nanotube yarns (Figure 6.14).

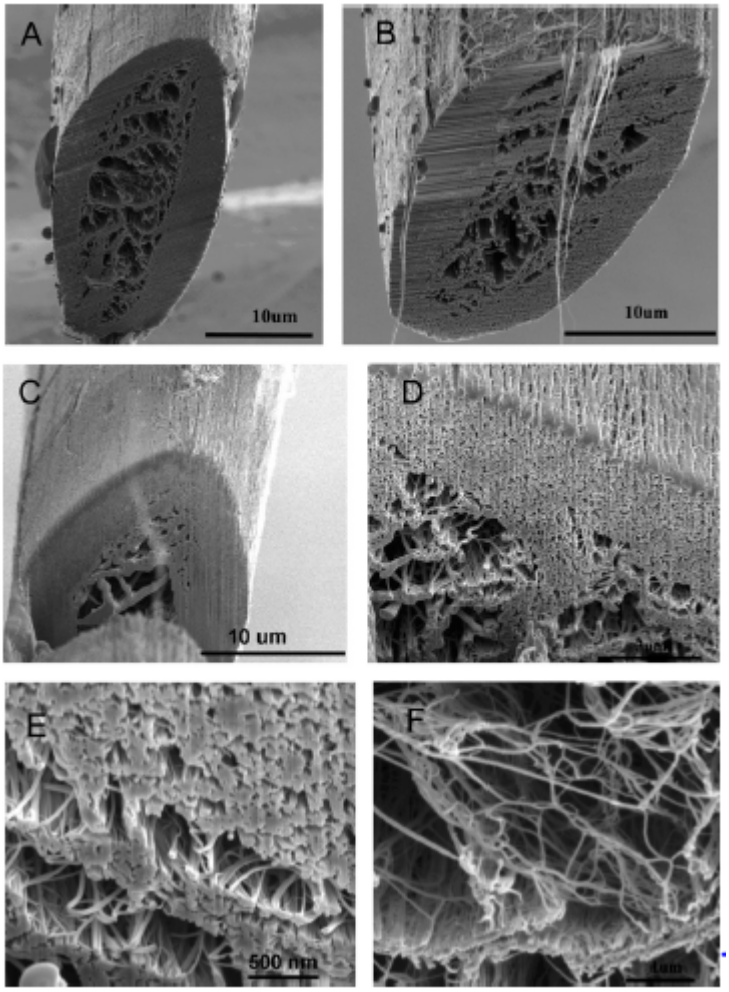

Figure 6.14 | Cross-sections of rub-densified carbon nanotube yarns: a-c. SEM images of yarn cross sections. **d,e.** SEM images of high CNT density areas. **f.** SEM images of large voids in the yarn core. (reprinted with permission[37] © Elselvier).

This method relies on rubbing densification in which a fiber is twisted and pulled in between two rubber rolling nips.

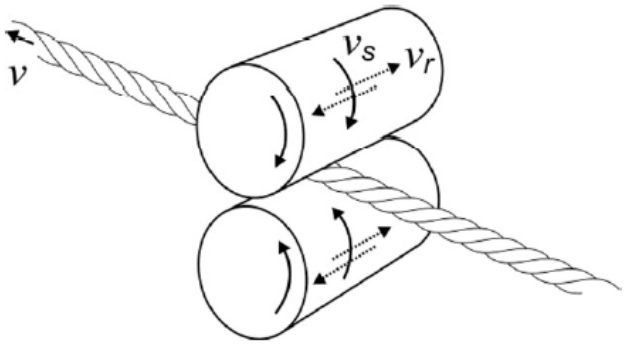

Figure 6.15 | Schematic of the alternating twist introduced by reciprocating rubbing rollers.

When the CNT yarn starts to travel cross the rubbing roller nip from the incoming side to the outgoing side, the twist brought with the yarn from the incoming side will cancel the opposite twist generated in the outgoing side. There is only a temporary twist on the incoming side that disappears on the outgoing side. The process is also known as false twisting and the result of a continuous false twisting process is the same as twisting a yarn in one direction first and then twisting by an equal amount in the opposite direction. The action of the moving surfaces is to rotate the yarn about its axis, causing the fibers to move around in a ‘‘race-track” fashion.

It may be possible to increase the elastic modulus of graphene composite fibers by rubbing densification, where the fibers are rolled over to make a ribbon like structure. It would be interesting to observe whether or not the rub-densified GO fibers form twistless structures with a highly packed sheath comprising of essentially straight and parallel graphene sheets/CNTs and hollow core similar to their CNTs counter parts.

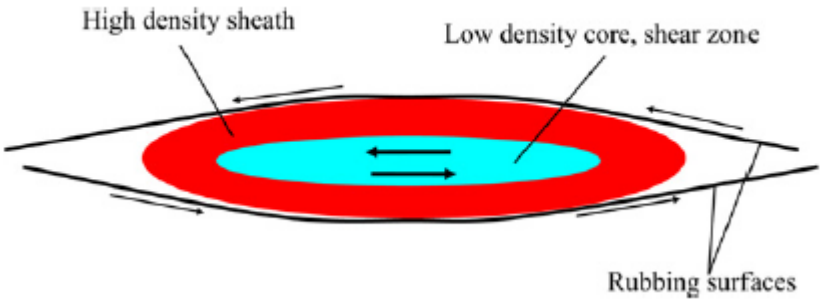

Figure 6.16 | A schematic of the core-sheath yarn structure forming process.

References:

1 Li, D., Muller, M. B., Gilje, S., Kaner, R. B. &Wallace, G. G. "Processable aqueous dispersions of graphene nanosheets." *Nat. Nanotechnol*. **3**, 101–105, doi:10.1038/nnano.2007.451 (2008)

2 Viculis, L. M., Mack, J. J., Mayer, O. M., Hahn, H. T. & Kaner, R. B. Intercalation and exfoliation routes to graphite nanoplatelets. *J. Mater. Chem*. **15**, 974–978, doi:10.1039/B413029D (2005)

3 Park, S. J. & Ruoff, R. S. Chemical methods for the production of graphenes. *Nat. Nanotechnol*. **4**, 217–224, doi: 10.1038/nnano.2009.58 (2009)

4 Chen, D., Feng, H. B. & Li, J. H. Graphene oxide: preparation, functionalization, and electrochemical applications. *Chem. Rev*. **112**, 6156–6214, doi: 10.1021/cr300115g (2012)

5 Dreyer, D. R., Park, S. J., Bielawski, C. W.& Ruoff, R. S. The chemistry of graphene oxide. *Chem. Soc. Rev*. **39**, 228–240, doi: 10.1039/B917103G (2010)

6 Coleman, Jonathan N., et al. "Two-dimensional nanosheets produced by liquid exfoliation of layered materials." *Science* **331**.6017, 568-571, doi: 10.1126/science.1194975 (2011)

7 Shin, H. J. et al. "Efficient reduction of graphite oxide by sodium borohydride and its effect on electrical conductance."*Adv. Funct. Mater*. **19**, 1987–1992, doi: 10.1002/adfm.200900167 (2009)

8 Kim, H. Y. et al. Scalable functionalized graphene nano-platelets as tunable cathodes for high-performance lithium rechargeable batteries. *Sci. Rep*. **3**, 1506, doi: 10.1038/srep01506 (2013)

9 Lemieurx., U. and Bauerh, . F. *Anal. Chem*. **26**: 920. 1954

10 Hiura, H., et al. "Role of sp3 defect structures in graphite and carbon nanotubes." *Nature* **367**, 148 – 151, doi:10.1038/367148a0 (1994)

11 Yang, Min, Satoshi Moriyama, and Masayoshi Higuchi. "Selective Edge Modification in Graphene and Graphite by Chemical Oxidation." *Journal of nanoscience and nanotechnology* **14**.4, 2974-2978, doi: 10.1166/jnn.2014.8578 (2014)

12 Wei, Liangming, et al. "Spontaneous intercalation of long-chain alkyl ammonium into edge- selectively oxidized graphite to efficiently produce high-quality graphene." *Scientific reports* **3**, doi:10.1038/srep02636 (2013)

13 Kuila, Tapas, et al. "Chemical functionalization of graphene and its applications." *Progress in Materials Science* **57**.7 (2012): 1061-1105, doi: 10.1016/j.pmatsci.2012.03.002 (2012)

14 Liu, Zhuang, et al. "PEGylated nanographene oxide for delivery of water-insoluble cancer drugs." *Journal of the American Chemical Society* **130**.33, 10876-10877, doi: 10.1021/ja803688x (2008)

15 Oren, Y. . "Capacitive deionization (CDI) for desalination and water treatment — past, present and future (a review)". *Desalination* **228** .1: 10–29, doi:10.1016/j.desal.2007.08.005 (2008)

16 El-Kady, Maher F., et al. "Laser scribing of high-performance and flexible graphene-based electrochemical capacitors." *Science* **335**.6074, 1326-1330, doi: 10.1126/science.1216744 (2012)

17 El-Kady, Maher F., and Richard B. Kaner. "Scalable fabrication of high-power graphene micro- supercapacitors for flexible and on-chip energy storage." *Nature communications* **4**, 1475, doi: 10.1038/ncomms2446 (2013)

18 Lin, Jian, et al. "3-dimensional graphene carbon nanotube carpet-based microsupercapacitors with high electrochemical performance." *Nano letters* **13**.1, 72-78, doi: 10.1021/nl3034976 (2012)

19 Gendel, Youri, et al. "Batch mode and continuous desalination of water using flowing carbon deionization (FCDI) technology." *Electrochemistry Communications* **46**, 152-156, doi:10.1016/j.elecom.2014.06.004 (2014)

20 Porada, S., et al. "Direct prediction of the desalination performance of porous carbon electrodes for capacitive deionization." *Energy & Environmental Science* **6**.12, 3700 3712, doi:10.1039/C3EE42209G (2013)

21 Jeon, Sung-il, et al. "Ion storage and energy recovery of a flow-electrode capacitive deionization process." *Journal of Materials Chemistry* A 2.18 , 6378-6383, doi: 10.1039/C4TA00377B (2014)

22 Peng, Wenchao, et al. "Synthesis of porous reduced graphene oxide as metal-free carbon for adsorption and catalytic oxidation of organics in water." *Journal of Materials Chemistry* A **1**.19, 5854-5859. doi: 10.1039/C3TA10592J (2013)

23 Joshi, R. K., et al. "Precise and ultrafast molecular sieving through graphene oxide membranes." *Science* 343.6172 ,752-754.doi: 10.1126/science.1245711 (2014)

24 Sridhar, Vadahanambi, et al. "Defect-engineered three-dimensional graphene–nanotube–palladium nanostructures with ultrahigh capacitance." *ACS nano* **6**.12, 10562-10570, doi:10.1021/nn3046133 (2012)

25 Wang, Lina, et al. "Synthesis and microwave absorption property of flexible magnetic film based on graphene oxide/carbon nanotubes and Fe_3O_4 nanoparticles." *Journal of Materials Chemistry A* **2**.36, 14940-14946, doi: 10.1039/C4TA02815E (2014)

26 Zhao, Hongbin, et al. "Reduced graphene oxide with ultrahigh conductivity as carbon coating layer for high performance sulfur@ reduced graphene oxide cathode." *Journal of Power Sources* 245, 529-536, doi: 10.1016/j.jpowsour.2013.07.002 (2014)

27 Potts, Jeffrey R., et al. "Graphene-based polymer nanocomposites." *Polymer* **52**.1, 5-25, doi: 10.1016/j.polymer.2010.11.042 (2011)

28 Jalili, Rouhollah, et al. "Scalable One-Step Wet-Spinning of Graphene Fibers and Yarns from Liquid Crystalline Dispersions of Graphene Oxide: Towards Multifunctional Textiles." *Advanced Functional Materials* **23**.43, 5345-5354. doi: 10.1002/adfm.201300765 (2013)

29 Jalili, Rouhollah, et al. "Organic solvent-based graphene oxide liquid crystals: a facile route toward the next generation of self-assembled layer-by-layer multifunctional 3D architectures." *Acs Nano* **7**.5, 3981-3990, doi: 10.1021/nn305906z (2013)

30 Xu, Zhen, and Chao Gao. "Graphene chiral liquid crystals and macroscopic assembled fibres." *Nature communications* **2**, 571. doi: 0.1038/ncomms1583 (2011)

31 Jiang, Kaili, Qunqing Li, and Shoushan Fan. "Nanotechnology: Spinning continuous carbon nanotube yarns." *Nature* **419**.6909, 801-801, doi: 10.1038/419801a (2002)

32 Kuznetsov, Alexander A., et al. "Structural model for dry-drawing of sheets and yarns from carbon nanotube forests." *Acs Nano* **5**.2, 985-993, doi: 10.1021/nn102405u (2011)

32 Thess, Andreas, et al. "Crystalline ropes of metallic carbon nanotubes." *Science-AAAS-Weekly Paper Edition* **273**.5274 (1996): 483-487 (1996)

33 Lee, R. S., et al. "Transport properties of a potassium-doped single-wall carbon nanotube rope." *Physical Review B* **61**.7, 4526. doi: 10.1103/PhysRevB.61.4526 (2000)

34 Ebbesen, T. W., and P. M. Ajayan. "Large-scale synthesis of carbon nanotubes." Nature **358**.6383, 220-222, doi: 10.1038/358220a0 (1992)

35 Addou, Rafik, et al. "Monolayer graphene growth on Ni (111) by low temperature chemical vapor deposition." *Applied Physics Letters* **100**.2, 021601, doi: /10.1063/1.3675481 (2012)

36 Zhang, Xiaobo, et al. "Spinning and Processing Continuous Yarns from 4-Inch Wafer Scale Super-Aligned Carbon Nanotube Arrays." *Advanced Materials* **18**.12, 1505-1510, doi: 10.1002/adma.20050252 (2006)

37 Miao, Menghe. "Production, structure and properties of twistless carbon nanotube yarns with a high density sheath." *Carbon* **50**.13, 4973-4983. doi: 1 0.1016/j.carbon.2012.06.035 (2012)